

CZTSSe THIN FILM: GROWTH, CHARACTERIZATION AND SOLAR CELL  
APPLICATIONS

A THESIS SUBMITTED TO  
THE GRADUATE SCHOOL OF NATURAL AND APPLIED SCIENCES  
OF  
MIDDLE EAST TECHNICAL UNIVERSITY



BY

MAKBULE TERLEMEZOĞLU

IN PARTIAL FULFILLMENT OF THE REQUIREMENTS  
FOR  
THE DEGREE OF DOCTOR OF PHILOSOPHY  
IN  
PHYSICS

AUGUST 2019



Approval of the thesis:

**CZTSSe THIN FILM: GROWTH, CHARACTERIZATION AND SOLAR  
CELL APPLICATIONS**

submitted by **MAKBULE TERLEMEZOĞLU** in partial fulfillment of the requirements for the degree of **Doctor of Philosophy in Physics Department, Middle East Technical University** by,

Prof. Dr. Halil Kalıpçılar  
Dean, Graduate School of **Natural and Applied Sciences**

Prof. Dr. Altuğ Özpineci  
Head of Department, **Physics**

Prof. Dr. Mehmet Parlak  
Supervisor, **Physics, METU**

Prof. Dr. Raşit Turan  
Co-Supervisor, **Physics, METU**

**Examining Committee Members:**

Prof. Dr. Macit Özenbaş  
Metallurgical and Materials Engineering, METU

Prof. Dr. Mehmet Parlak  
Physics, METU

Prof. Dr. Bahtiyar Salamov  
Physics, Gazi University

Prof. Dr. Ayşe Çiğdem Erçelebi  
Physics, METU

Prof. Dr. Dilber Esra Yıldız  
Physics, Hitit University

Date: 19.08.2019



**I hereby declare that all information in this document has been obtained and presented in accordance with academic rules and ethical conduct. I also declare that, as required by these rules and conduct, I have fully cited and referenced all material and results that are not original to this work.**

Name, Surname: Makbule Terlemezođlu

Signature:

## ABSTRACT

### CZTSSe THIN FILM: GROWTH, CHARACTERIZATION AND SOLAR CELL APPLICATIONS

Terlemezođlu, Makbule  
Doctor of Philosophy, Physics  
Supervisor: Prof. Dr. Mehmet Parlak  
Co-Supervisor: Prof. Dr. Rađit Turan

August 2019, 146 pages

$\text{Cu}_2\text{ZnSn}(\text{S},\text{Se})_4$  (CZTSSe) compound is one of the most promising absorber materials for thin film solar cell technology due to the abundance and non-toxicity of its constituents. Besides, CZTSSe has an ideal direct band gap value in the range of 1-1.5 eV and high absorption coefficient ( $> 10^4 \text{ cm}^{-1}$ ) in the visible region, which satisfies the conversion of the maximum amount of energy of the solar spectrum. For this, CZTSSe absorber layer with only a few microns of thickness is sufficient to absorb all the photons having the energy greater than its band gap. Another advantage is that its crystal structure is very similar to chalcopyrites. For this reason, CZTSSe thin film based solar cells are fabricated in a similar manner to chalcopyrite based solar cells.

This study focused on the growth, characterization, and photovoltaic applications of CZTSSe thin films. In this context, firstly, CZTSSe thin films were grown by using thermal evaporation method on both glass and silicon (Si) substrates. During the deposition process, sintered crystalline powder of CZTSSe was used as the evaporation source to obtain CZTSSe thin films in an efficient and cost-effective way. Post annealing process was applied to increase the homogeneity of the deposited thin films. Subsequently, the characterization of annealed films was carried out. Then, the

electrical properties of the CZTSSe/Si structure were investigated using temperature-dependent current-voltage (I-V) and frequency dependent capacitance-voltage (C-V) measurements for possible future applications in various technologies.

Also, in this study, CZTSSe thin films having a surface decorated with self-assembled nanoflakes were fabricated by utilizing the RF magnetron sputtering method. It was observed that the self-assembled nanostructures on the surface of the film yield low surface reflectance. The formation of nanoflakes was investigated. It was observed that the size of nanoflakes can be adjusted by an accurate control of the sputtering process, including film thickness. Moreover, the effect of substrate temperature on the formation of nanoflakes at the film surface was discussed at a fixed deposition route.

In the last part of the thesis, CZTSSe thin film based solar cells were fabricated in superstrate configuration. For this purpose, the performance of glass/ITO/CdS/CZTSSe/metal structure was investigated. Then, the effect of titanium dioxide layer ( $\text{TiO}_2$ ) on the device performance was examined due to its being a hole blocking and wide band gap material properties. As a result, the considerable positive effect of  $\text{TiO}_2$  layer on the open circuit voltage was observed.

**Keywords:** CZTSSe, Thin Film, Solar Cell, Self-assembled Nanostructures

## ÖZ

### CZTSSe İNCE FİLM: BÜYÜTME, KARAKTERİZASYON VE GÜNEŞ HÜCRESİ UYGULAMALARI

Terlemezoğlu, Makbule

Doktora, Fizik

Tez Danışmanı: Prof. Dr. Mehmet Parlak

Ortak Tez Danışmanı: Prof. Dr. Raşit Turan

Ağustos 2019, 146 sayfa

$Cu_2ZnSn (S,Se)_4$  (CZTSSe) bileşiği, bileşenlerinin bolluğu ve toksik olmaması nedeniyle ince film güneş pili teknolojisi için en umut verici emici malzemelerden biridir. Ayrıca, CZTSSe, görünür bölgede 1-1.5 eV arasında direkt bant aralığı değerine ve yüksek soğurma katsayısına ( $> 10^4 \text{ cm}^{-1}$ ) sahiptir ve bu da güneş spektrumunun enerjije dönüşmesini maksimum düzeyde sağlar. Bunun için, sadece birkaç mikron kalınlığa sahip olan CZTSSe emici tabaka, bant aralığından daha büyük enerjije sahip tüm fotonları soğurmak için yeterlidir. Bir başka avantajı ise, kristal yapısının kalkopiritlere çok benzemesidir. CZTSSe ince film bazlı güneş pilleri kalkopirit bazlı güneş pillerine benzer şekilde üretilir.

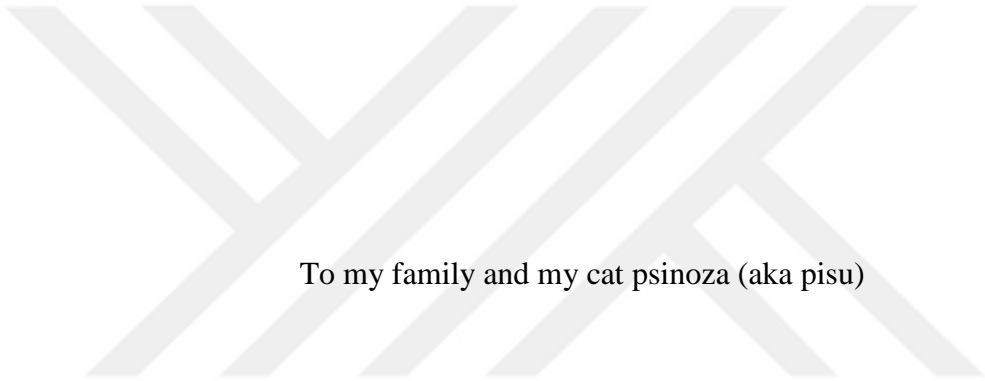
Bu çalışmada, CZTSSe ince filmlerinin büyütülmesine, karakterizasyonuna ve fotovoltajik uygulamalarına odaklanıldı. Bu bağlamda, ilk olarak, CZTSSe ince filmler termal buharlaştırma yöntemi kullanılarak hem cam hem de silisyum (Si) alttaşlar üzerine büyütüldü. Biriktirme işlemi esnasında, CZTSSe ince filmlerini etkili ve uygun maliyetli bir şekilde elde etmek için sinterlenmiş CZTSSe kristal tozu buharlaşma kaynağı olarak kullanıldı. Üretilen ince filmlerin homojenliğini arttırmak için tavlama işlemi uygulandı. Ardından, tavllanmış filmlerin karakterizasyonu yapıldı. Daha sonra, çeşitli teknolojilerde muhtemel uygulanabilirliğini görmek

amacıyla, CZTSSe/Si yapısının elektriksel özellikleri sıcaklığa bağılı akım-voltaj (I-V) ve frekansa bağılı kapasitans-voltaj (C-V) ölçümleri yapılarak incelendi.

Buna ek olarak, bu çalışmada, kendiliğinden oluşan nano-pullarla kaplı bir yüzeye sahip olan CZTSSe ince filmleri, RF manyetik saçtırma yöntemi kullanılarak üretildi. Film yüzeyinde kendiliğinden oluşan nano-yapıların oldukça düşük yüzey yansımaları sağladığı görüldü. Nano-pulların oluşumu incelendi. Film kalınlığının da dahil olduğu saçtırma işleminin hassas bir şekilde kontrol edilmesiyle, nano-pulların boyutunun ayarlanabildiği gözlemlendi. Ayrıca, alttaş sıcaklığının film yüzeyi üzerindeki nano-pulların oluşumu üzerindeki etkileri sabit bir üretim rotasında tartışıldı.

Tezin son bölümünde, CZTSSe ince film tabanlı güneş pilleri, üst tabaka konfigürasyonunda üretildi. Bu amaçla, cam/ITO/CdS/CZTSSe/metal yapısının performansı incelendi. Ardından, geniş bant aralıklı ve iyi bir deşik bloklama malzemesi olmasından dolayı titanyum dioksit katmanının ( $\text{TiO}_2$ ) aygıt performansı üzerindeki etkisi incelendi. Sonuç olarak,  $\text{TiO}_2$  katmanının açık devre voltajı üzerinde önemli ölçüdeki olumlu etkisi gözlemlendi.

Anahtar Kelimeler: CZTSSe; İnce Film, Güneş Hücresi, Kendiliğinden Oluşan Nanoyapılar



To my family and my cat psinoza (aka pisu)

## ACKNOWLEDGMENTS

I would first like to express my deepest gratitude to my supervisor Prof. Dr. Mehmet Parlak, for his advice, guidance, and allowing me to work in his group. It was a great honor and privilege for me to work under his supervision. I will forever be grateful to him for his patience and continuous support. I would also like to give special thanks to my co-supervisor Prof. Dr. Raşit Turan, for his guidance and support since the first day that I met him in Eskişehir. I am also very grateful to him for his scientific advice and suggestions.

I am also very grateful to members of the thesis monitoring committee, Prof. Dr. Macit Özenbaş and Prof. Dr. Bahtiyar Salamov, for their invaluable suggestions, comments, and kindly attitude towards me during this study. I would like to present my sincere thanks to Prof. Dr. Ayşe Çiğdem Erçelebi for her valuable comments, informative discussion, and endless support through this research. I am also thankful to Prof. Dr. Dilber Esra Yıldız for sharing her knowledge and being helpful.

I would like to thank Assoc. Dr. Hakan Karaağaç for enabling me to participate in his Tübitak 1003 project with a project number of 315M401.

I will always be grateful to Prof. Dr. Yasemin Yıldız Yarar, Prof. Dr. Serbüent Yıldırım, and Assoc. Prof. Dr. Kadir Ertürk, who provided me an opportunity to join METU, for their patience and support.

I am very grateful to Assoc. Prof. Dr. Tahir Çolakoğlu for valuable suggestions, unlimited support, and brainstorming that we did. He has been my mentor and my brother. I will never forget his help.

I want to thank Assis. Prof. Dr. Hasan Hüseyin Güllü for his friendship, useful discussion, and sharing his experience with me. I want to send special thanks to Dr. Özge Bayraklı Sürücü, who makes the laboratory a joyful place, for her sincere friendship, help, and collaboration since the first day I joined the group. Discussions

about our research for hours on the phone at midnight were invaluable for me. Special thanks also go to Assoc. Prof. Dr. Gökhan Sürücü for his useful advice and great friendship. Without the Sürücü family, that period would be more difficult. I also want to thank Çiğdem Doğru, who has always been a great friend to me. I would like to continue with Merve Demir for her friendship.

I would like to express my sincere thanks to two special people: E. Hande Çiftınar and Ergi Dönerçark. I do not know how I can explain the importance of them for me. I would like to start with Hande. Hande, who is the most talented and smartest girl I have ever met, has always been a real friend. I am also grateful to her for stimulating discussions that we did. Ergi has been my invaluable friend and my brother. He motivated me by mentioning about the biography that I will write one day, named as ‘‘from Çorum to New York’’:).

I am also grateful to Dr. Aydın Tankut, Kurtuluş Abak, Mustafa Ünal for their friendship and sharing their knowledge with me. My sincere thanks also go to Gence Bektaş for his priceless friendship. Also, I am thankful to Hava Akpınar and Wiria Sultanpoor for helping me, sparing their time and preparing TiO<sub>2</sub> layer.

I would like to extend my thanks to my friends at GÜNAM, namely, Dr. Mehmet Karaman, Olgu Demircioğlu, Zeynep Demircioğlu, Salar Habibur Sedani, Burcu Barutçu, Dr. Fırat Es, Emel Semiz, Dr. Gülşen Baytemir, Dr. İsmail Kabaçelik, , Dr. Bülent Arıkan, Dr. Engin Özkol, Dr. Hisham Nasser, Gamze Kökbudak, Dr. Serra Altınoluk, Mete Günöven, Özden B. Balbaşı, Deniz Bender, Seda Kayra Güllü, Cansu Emir, Mona Zolfaghariborra Borra, Arman Ayan, Milad Ghasemikashitaban, İbrahim Murat Öztürk and Dr. Kamil Çınar for their friendship. I am also grateful to GÜNAM technicians: Yücel Eke, Tayfun Yıldız, Nevzat Görmez for technical support and I am also thankful to Harun Tanık, Tuncay Güngör, Buket Gökbakan and Mehtap Kaynar for their support. I also thank Gülşen Özdemir Parlak and Zeynep Eke for their help and conversations when I felt stressed.

I would like to thank Prof. Dr. Vildan Bilgin, Prof. Dr. Ferhunde Atay, and Assoc. Prof. Dr. Salih Köse for their great support and guiding me on the right path. I would not be where I am today without them. I am also deeply grateful to Prof. Dr. Takhmasib Aliev and Prof. Dr. İsmail Turan for their help and support. I am also thankful to Prof. Dr. Bayram Tekin for endless support and informative discussion during my education life.

A very special thanks to Zehra Aras, my dear friend, who is always there to support me for my bad days and good day. I will never forget the amazing time that we spent together.

I would like to thank Selçuk Bilmiş for his love and being my biggest support. There are not enough words that could explain my appreciation for him. He made my life beautiful. He motivated me during difficult times when I needed it. Thanks for being a good mentor, being my best friend I have ever had, being a man that I fell in love and thank you for always believing me.

Last but not least, I am endlessly grateful to my lovely parents, Fatma and İbrahim Terlemezoğlu, for their support, encouragement, and unconditional love through my life. I would also like to give special thanks to my brother and his wife, Zeynel and Ayşe Terlemezoğlu, for everything we shared.

I am grateful for every soul who has been part of my journey.

## TABLE OF CONTENTS

ABSTRACT.....	v
ÖZ.....	vii
ACKNOWLEDGMENTS .....	x
TABLE OF CONTENTS .....	xiii
LIST OF TABLES .....	xvii
LIST OF FIGURES .....	xviii
LIST OF ABBREVIATIONS .....	xxiv
LIST OF SYMBOLS .....	xxvi
CHAPTERS.....	1
1. INTRODUCTION .....	1
1.1. Current Status of Photovoltaic Technologies .....	1
1.2. The Properties of CZTSSe Compound.....	6
1.3. Superstrate Configuration of CZTSSe Thin Film Based Solar Cells .....	8
1.4. Outline of This Thesis .....	10
2. THEORETICAL CONSIDERATIONS .....	13
2.1. Absorption of Light .....	13
2.2. Direct and Indirect Band Gap Semiconductor.....	14
2.3. Absorption Coefficient .....	15
2.4. The Solar Radiation.....	18
2.5. Metal-Semiconductor Junction.....	19

2.5.1. Schottky Junction .....	19
2.5.2. Ohmic Contact.....	22
2.6. Physics of p-n Junction .....	23
2.7. Operating Principles of Solar Cells.....	26
2.8. Solar Cell Parameters.....	29
2.9. Simulation of CZTSSe Solar Cells in Superstrate Configuration Using SCAPS-1D Software .....	31
3. METHODOLOGY .....	35
3.1. Introduction.....	35
3.2. Thin Film Growth Techniques.....	35
3.2.1. Thermal Evaporation Technique .....	35
3.2.2. RF/DC Magnetron Sputtering Technique .....	37
3.3. Post-Annealing Process.....	39
3.4. Thin Film Characterization Techniques.....	39
3.4.1. X-Ray Diffraction (XRD) .....	40
3.4.2. Raman Scattering Spectroscopy .....	42
3.4.3. Scanning Electron Microscopy (SEM).....	43
3.4.4. Energy Dispersive X-ray Spectroscopy (EDS) .....	45
3.4.5. Atomic Force Microscopy (AFM) .....	45
3.4.6. Transmission and Reflection Measurements.....	46
3.4.7. Resistivity Measurement .....	47
3.4.8. Photoconductivity Measurement .....	49
3.4.9. Hall Effect Measurement.....	51
3.5. Device Characterization Techniques .....	53

3.5.1. Current-Voltage Measurements .....	53
3.5.2. Capacitance-Voltage Measurements.....	53
3.5.3. Solar Cell Measurements .....	54
4. DEPOSITION AND CHARACTERIZATION OF THERMALLY EVAPORATED CZTSSe THIN FILMS AND ANALYSIS OF CURRENT CONDUCTION MECHANISM OF CZTSSe/Si STRUCTURE .....	55
4.1. Introduction .....	55
4.2. Experimental Procedure .....	56
4.3. Results and Discussions .....	59
4.3.1. Structural Properties of CZTSSe Thin Film .....	59
4.3.2. Optical Properties of CZTSSe Thin Film .....	64
4.3.3. Electrical Properties of CZTSSe Thin Film.....	66
4.3.4. Device Behavior of In/CZTSSe/Si/Ag Structure.....	67
5. CONSTRUCTION OF SELF ASSEMBLED NANOFILAKES ON CZTSSe THIN FILMS .....	83
5.1. Introduction .....	83
5.2. Experimental Procedure .....	84
5.3. Results and Discussion .....	87
5.3.1. Effect of Precursor Thickness on the Nanoflakes.....	87
5.3.2. Effect of Substrate Temperature on the Formation of Nanoflakes.....	100
6. CZTSSe THIN FILMS FABRICATED BY SINGLE STEP DEPOSITION FOR SUPERSTRATE SOLAR CELL APPLICATIONS.....	105
6.1. Introduction .....	105
6.2. Experimental Procedure .....	106
6.3. Results and Discussion .....	108

6.3.1. Structural, Optical and Electrical Properties of the Absorber Layer.....	108
6.3.2. Photovoltaic Properties of SLG/ITO/CZTSSe/CdS/Au Superstrate Structure .....	114
6.3.3. The Effect of TiO <sub>2</sub> Layer on the Device Performance of CZTSSe Superstrate Structure .....	117
6.3.3.1. Physical Properties of TiO <sub>2</sub> Layer .....	117
6.3.3.2. The Effect of TiO <sub>2</sub> Thickness on Device Performance .....	119
6.3.3.3. The Effect of Different Contact Materials on CZTSSe Superstrate Solar Cells .....	121
7. CONCLUSION .....	125
REFERENCES .....	129
CURRICULUM VITAE.....	141

## LIST OF TABLES

Table 2.1. SCAPS input parameters [78], [79] .....	32
Table 4.1. Device parameters extracted from the analysis of temperature dependent I-V measurements .....	70
Table 5.1. Experimental conditions and process parameters of D1, D2, D3 and D4	86
Table 5.2. Structural parameters of CZTSSe films acquired from XRD patterns of annealed D1 and D2 samples .....	88
Table 5.3. Elemental compositional analysis of CZTSSe thin films acquired from EDS measurements .....	91
Table 6.1. Solar cell parameters of SLG/FTO/CdS/CZTSSe/Ag-Au structure extracted from I-V curves under illumination .....	121
Table 6.2. Device performance results of SLG/FTO/TiO <sub>2</sub> /CdS/CZTSSe/metal structure with different contact materials.....	123

## LIST OF FIGURES

Figure 1.1. Implementations of CIGS modules [13]. .....	2
Figure 1.2. NREL' cell efficiency graph [24].....	4
Figure 1.3. Abundance (atom fraction) of chemical elements in Earth's upper continental crust as a function of atomic number. Many of elements are classified into (partially overlapping) categories: (1) rock-forming elements (major elements in green field and minor elements in light green field); (2) rare earth elements (lanthanides, La-Lu, and Y; labeled in blue); (3) major industrial metals (global production > $\sim 3 \times 10^7$ kg/year; labeled in bold); (4) precious metals (italic); and (5) the nine rarest "metals"-the six platinum group elements plus Au, Re, and Te (a metalloid) (adopted from, [25]). .....	5
Figure 1.4. The relationship of binary, ternary and quaternary structures [38] .....	6
Figure 1.5. Kesterite (left) and stannite (right) crystal structures; large yellow sphere: S and Se; small sphere: blue Cu, yellow Zn, red Sn [41]. .....	7
Figure 1.6. Substrate and superstrate configurations of CZTSSe based solar cells. ...	9
Figure 2.1. Simplified illustration of different optical absorption processes in semiconductors: (1) band to band, (2) interconduction band, (3) intervalance band, (4) donor to conduction band, (5) valance band to acceptor, (6) valance band to donor, (7) acceptor to conduction band and (8) acceptor to donor transitions. ....	14
Figure 2.2. Energy-crystal momentum diagram of direct and indirect band gap semiconductor [65]. .....	15
Figure 2.3. Solar irradiance spectrum [69]. .....	19
Figure 2.4. Schottky barrier formation by contacting n-type semiconductor with a metal .....	20
Figure 2.5. Schottky junction under the forward and reverse bias for n-type semiconductor. ....	21
Figure 2.6. Ohmic contact between metal and n-type semiconductor. ....	22

Figure 2.7. Schematic diagram of (a) p-n junction, (b) band alignment in equilibrium. Donor atoms (blue particles), acceptor atoms (red particles), electrons (black particles) and holes (white particles). .....	24
Figure 2.8. The operating principle of typical solar cell [71]. .....	26
Figure 2.9. The variation of photogenerated EHPs concentration with distance due to absorption of light (taken from [71] ). .....	28
Figure 2.10. Typical current density-voltage characteristics of a solar cell [74]......	30
Figure 2.11. Equivalent circuit of solar cell (a) ideal p-n junction, (b) with series and shunt resistances (adopted by Ref. [71] ). .....	31
Figure 2.12. (a) Energy band diagram of CZTSSe solar cell, (b) J-V characteristics, (c) quantum efficiency vs wavelength plot of simulated CZTSSe superstrate solar cell under illumination .....	34
Figure 3.1. The multi-source thermal evaporation system and schematic view of the chamber of the system 1: fusion cells, 2: shutters of fusion cells, 3: substrate, 4: heater, 5: shutter of the substrate, 6: thickness monitor probe.....	36
Figure 3.2. An image showing Vaksis three magnetron sputtering system. ....	37
Figure 3.3. Schematic presentation of three magnetron system. 1: targets, 2: shutters, 3: substrate holder, 4: halogen lamp heater, 5: thickness monitor probe, 6: Ar flow controller, 7: vacuum valve, 8: turbo molecular pump, 9: rough pump, 10: control unit. ....	38
Figure 3.4. Horizontal tube furnace. ....	39
Figure 3.5. (a) X-rays diffraction from crystal planes, (b) observed diffraction peak. ....	40
Figure 3.6. X-ray diffraction system. ....	41
Figure 3.7. Schematic representation of Rayleigh and Raman Scattering [86]. .....	42
Figure 3.8. Raman Spectroscopy System.....	43
Figure 3.9. An image showing the main parts of the SEM system.....	44
Figure 3.10. The schematic diagram of AFM. 1: piezo-electric scanner, 2: sample, 3: chip with cantilever, 4: laser diode, 5: mirror, 6: position-sensitive photodetector, 7: electronics (computer system).....	45

Figure 3.11. AFM setup used in this study.....	46
Figure 3.12. Bentham PVE 300 system.....	47
Figure 3.13. Schematic representation of van der Pauw geometry that was prepared for electrical characterization. ....	48
Figure 3.14. The illustration of the cryostat system. ....	49
Figure 3.15. Experimental setup of photoconductivity and Hall effect system.....	51
Figure 3.16. The experimental setup of temperature dependent current-voltage and frequency dependent capacitance-voltage measurement system.....	53
Figure 3.17. Schematic presentation of solar simulator. ....	54
Figure 4.1. (a) Vertical furnace, (b) Bridgman-Stockbarger system. ....	57
Figure 4.2. The XRD pattern of deposited film.....	59
Figure 4.3. Raman spectrum of the deposited film.....	60
Figure 4.4. (a) Cross-sectional, (b) top-view SEM images of CZTSSe/Si structure. ....	62
Figure 4.5. (a) 3D, (b) 2D 10 $\mu$ m x 10 $\mu$ m AFM images of deposited film. ....	63
Figure 4.6. Transmission and absorption spectrum of CZTSSe thin film. ....	64
Figure 4.7. Absorption coefficient of deposited film and the inset shows Tauc plot used for band gap calculation of CZTSSe thin film. ....	65
Figure 4.8. Temperature dependent electrical conductivity of deposited film. Inset shows the linearity of different temperature regions in dark. ....	66
Figure 4.9. The schematic diagram of fabricated diode structure. ....	67
Figure 4.10. Temperature dependent current-voltage graph of Ag/Si/CZTSSe/In structure. ....	69
Figure 4.11. The variations of (a) zero bias barrier height and (b) ideality factor with temperature. ....	71
Figure 4.12. Zero bias barrier height vs ideality factor graph of CZTSSe/Si structure. ....	72
Figure 4.13. The plot of $\phi_{BO}$ vs $q/2kT$ for CZTSSe/Si structure. ....	74
Figure 4.14. The plot of $(n^{-1} - 1)$ vs $q/2kT$ .....	75
Figure 4.15. The modified Richardson plof of $\ln(I_0/T^2) - (q^2\sigma_0^2)/(2k^2T^2)$ vs $q/kT$ .....	76

Figure 4.16. Under dark and illumination at room temperature, the plots of (a) semi logarithmic I-V and (b) J-V in the voltage range of 0 and 0.15 V.....	77
Figure 4.17. Frequency-dependent capacitance voltage characteristics of CZTSSe/Si structure.....	78
Figure 4.18. Frequency-dependent conductance voltage characteristics of CZTSSe/Si structure.....	79
Figure 4.19. The profile of density of interface states achieved from $C_{HF}-C_{LF}$ capacitance method. ....	79
Figure 4.20. The density profile of states obtained by from the Hill-Coleman method. ....	81
Figure 5.1. Schematic presentation of stacking order of precursors .....	84
Figure 5.2. XRD spectra of as-deposited and annealed samples of D1 and D2 .....	87
Figure 5.3. Raman spectra of as-deposited and annealed films of D1 and D2 .....	89
Figure 5.4. (a) Top view, (b) and (c) tilted SEM images of as deposited D1 film, (d) top view, (e) and (f) tilted SEM images of annealed D1 film.....	92
Figure 5.5. (a) SEM images of annealed sample surface of D1 and elemental EDS mapping of sample surface for (b) Cu, (c) Zn, (d) S, (e) Se and (f) Sn .....	94
Figure 5.6. (a) High angle annular dark field STEM image of annealed film (D1); EDS mapping of (b) Cu, (c) Zn, (d) S, (e) Se and (f) Sn.....	95
Figure 5.7. The evolution of the nanoflakes on the film surface; SEM micrographs after (a) ZnSe layer, (b) ZnSe/CuSe stacked layers, (c) ZnSe/CuSe/SnS stacked layers and (d) sixth layers depositions of D1 .....	96
Figure 5.8. The top view SEM images of (a) as-deposited, (b) annealed sample of D2 .....	97
Figure 5.9. Reflectance and transmittance spectra of as-deposited and annealed samples of D1 and D2 .....	98
Figure 5.10. PL spectrum of annealed CZTSSe film of D1 at room temperature .....	99
Figure 5.11. Temperature dependent electrical conductivity of annealed CZTSSe film of D1 under dark and illumination.....	100
Figure 5.12. XRD patterns of D1, D2, D3 and D4 samples.....	101

Figure 5.13. Raman spectra of D1, D2, D3 and D4 samples.....	102
Figure 5.14. The top view SEM micrographs of (a) as-deposited, (b) annealed films of D3, (c) as-deposited, (d) annealed films of D4 .....	103
Figure 5.15. Reflectance versus wavelength plot of D1, D3 and D4 samples .....	104
Figure 6.1. The schematic presentation of precursor sequence. ....	106
Figure 6.2. Flow diagram of solar cell fabrication in superstrate configuration .....	107
Figure 6.3. The XRD pattern of CZTSSe layer. The inset shows the XRD pattern of CdS layer. ....	109
Figure 6.4. Raman spectrum of CZTSSe layer.....	110
Figure 6.5. The SEM surface image of CZTSSe thin film. ....	111
Figure 6.6. The plot of reflectance and transmittance of CZTSSe layer as a function of wavelength.....	112
Figure 6.7. $(\alpha h\nu)^2$ vs $h\nu$ graph for CZTSSe thin film. Inset shows the $(\alpha h\nu)^2$ vs $h\nu$ graph for CdS layer.....	113
Figure 6.8. Temperature dependent dark and illuminated conductivity behavior of CZTSSe thin film. Inset shows the variation of dark conductivity. ....	114
Figure 6.9. J-V graph for ITO/CdS/CZTSSe/Au solar cell under dark and illumination. Inset shows the J-V graph of the solar cell at the voltage range of 0 and 0.5 V.....	115
Figure 6.10. External quantum efficiency (EQE) spectrum of ITO/CdS/CZTSSe/Au structure. The inset shows the $[h\nu \ln(1-EQE)]^2$ vs $h\nu$ plot of CZTSSe layer. ....	116
Figure 6.11. XRD results of anatase TiO <sub>2</sub> layer (90 nm) on FTO substrate.....	118
Figure 6.12. Top view SEM image of the TiO <sub>2</sub> thin film with a thickness of 90 nm. ....	118
Figure 6.13. Transmission spectra of TiO <sub>2</sub> films with different thickness on FTO substrate. ....	119
Figure 6.14. TiO <sub>2</sub> thickness dependence of J-V and I-V plots as linear and semi-logarithmic scales of SLG/FTO/TiO <sub>2</sub> /CdS/CZTSSe/Ag-Au structure in dark and under illumination. Thickness of TiO <sub>2</sub> layer is (a), (b) 20 nm; (c), (d) 50 nm; (e), (f) 90 nm. ....	120

Figure 6.15. J-V and I-V plots in linear and semi-logarithmic scales in dark and under illumination for (a), (b) of SLG/FTO/TiO<sub>2</sub>/CdS/ CZTSSe/Au; (c), (d) of SLG/FTO/TiO<sub>2</sub>/CdS/CZTSSe/Cr-Au structures.....122

Figure 6.16. Simulated J-V curve of solar cell with high series and low shunt resistance value by using SCAPS 1D. ....123



## LIST OF ABBREVIATIONS

PV	Photovoltaic technology
CIGS	Copper-indium-gallium-selenide
CdTe	Cadmium telluride
CZTS	Copper-zinc-tin-sulfide
CZTSe	Copper-zinc-tin-selenide
CZTSSe	Copper-zinc-tin-sulfo-selenide
MBE	Molecular beam epitaxy
XRD	X-ray diffraction
CdS	Cadmium sulfide
Mo	Molybdenum
Si	Silicon
FWHM	Full width at half maxima
TE	Thermionic emission
RF	Rectification factor
AFM	Atomic force microscopy
EDS	Energy dispersive X-ray spectroscopy
SEM	Scanning electron microscope
I-V	Current-voltage
C-V	Capacitance-voltage
G/w-V	Conductance-voltage

FF	Fill factor
GD	Gaussian distribution
$C_{HF-C_{LF}}$	High-low frequency capacitance
$D_{it}$	Interface state density
PVD	Physical vapor deposition
DC	Direct current
RF	Radio frequency



## LIST OF SYMBOLS

$\alpha$	Absorption coefficient
$q\phi_m$	Work function of metal
$q\phi_s$	Work function of semiconductor
$\chi$	Electron affinity
$\eta$	Efficiency
$n$	Ideality factor
$E_{Fm}$	Fermi level of metal
$D_e$	Diffusion coefficient of electron
$\Phi_{B0}$	Zero-bias barrier height
$I_0$	Saturation current

## CHAPTER 1

### INTRODUCTION

#### 1.1. Current Status of Photovoltaic Technologies

“ More energy from sunlight strikes Earth in 1 hour than all of the energy consumed by humans in an entire year”

-Nathan S. Lewis, 2007

The increasing energy demand is one of the most important problems all over the world since energy consumption has increased exponentially due to the industrial evolution [1], [2]. The main energy source of the world, regarding electricity, is based on fossil fuels such as coal and natural gas. However, conventional fossil fuels, which are the limited resources lead to both insufficiencies in demand and increase in price [3], [4]. Besides, the usage of fossil fuels on energy production gives rise to global severe problems such as climate change caused by greenhouse gas emission and acid rains [5].

For this reason, in recent decades, there has been a push towards the usage of the renewable sources such as solar energy, wind energy, geothermal energy, etc. to cope with the increasing energy demand in an environmental friendly way. Among the other alternative energy sources, solar energy is one of the most abundant, clean, and accessible energy sources. Photovoltaic technology (PV), which is based on generating electricity directly from sunlight, has been become a significant player for

the future economy concerning clean energy since the costs of PV systems has been dropped continuously.

Although more than %80 of current PV technology is based on conventional silicon (Si) wafer based technology, this technology has some fundamental limitations such as having an indirect band gap, high material consumption, and limited flexibility[4], [6], [7]. For this reason, thin film PV technologies have been an alternative to Si wafer based technology.

The semiconductor materials used in thin film solar cells have a direct band gap and higher absorption coefficient than silicon such as copper indium (gallium) selenide (CIGS) and cadmium telluride (CdTe) [8], [9]. Especially as an emerging application, CIGS modules become prevalent due to lightweight and flexibility [10]–[12]. Some of the possible implementations of CIGS modules are shown in Figure 1.1.

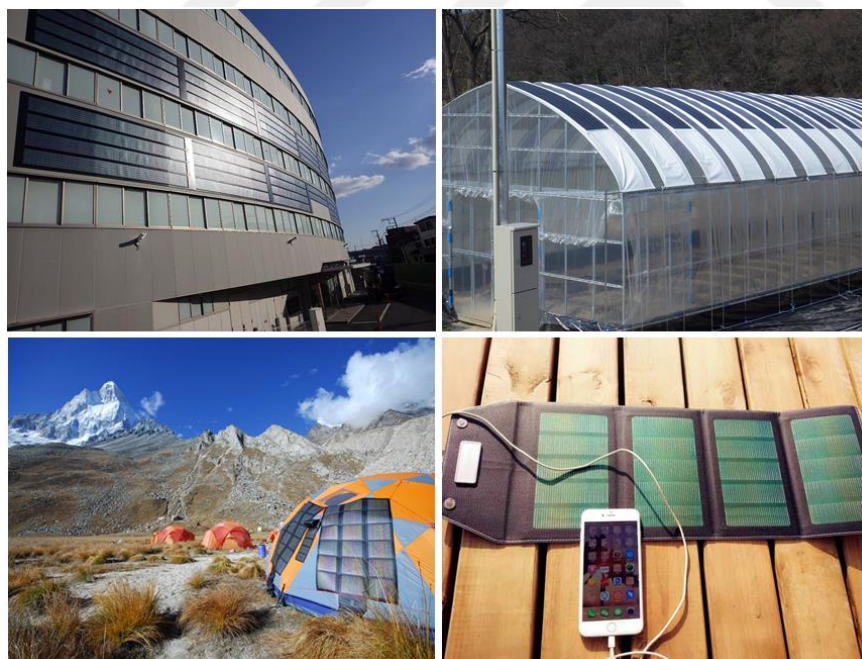


Figure 1.1. Implementations of CIGS modules [13].

In fact, efficiencies of fabricated solar cells in lab-scale from those materials have been comparable with the Si-based solar cells, as indicated from Figure 1.2. Although CIGS and CdTe based PV technologies demonstrated remarkable efficiencies, the scarcity of In and Te elements has emerged as the most controversial issue, limiting the mass production in TW scale [14]–[16]. The abundance of chemical elements in Earth's upper continental crust as a function of atomic numbers is given in Figure 1.3.

Recently, the kesterite structures belonging to the family of  $I_2-II-IV-VI_4$  quaternary compounds, specifically copper-zinc-tin-sulfide ( $Cu_2ZnSnS_4$ -CZTS), copper-zinc-tin-selenide ( $Cu_2ZnSnSe_4$ -CZTSe), and their alloys copper-zinc-tin-sulfo-selenide ( $(Cu_2ZnSn(S,Se)_4$ -CZTSSe) have attracted a prominent attention due to their appropriately tunable physical properties by changing chemical composition of the constituent elements for an optimized photovoltaic conversion of sunlight into electricity [17], [18].

With the earth abundant and non-toxic constituent elements as Zn and Sn, kesterite structures can be utilized as a potentially low-cost material for large-scale photovoltaic production. These kesterite structures are derived from the well-known compounds; CIGSe by substituting the rare metals, In and Ga by Zn and Sn or CIGSe by changing In with partially Zn and Sn. Figure 1.4 shows the relationship of binary, ternary, and quaternary semiconductors from II-VI compound to CZTS compound. The main reason for the attraction of the investigations of these quaternary compounds is analogous to characteristics of CIGSe material.

Similarities in the crystal structure and electronic characteristics of CIGSe and CZTSSe compounds makes kesterite compounds the most promising alternative absorber layer. In particular, the crystal and lattice structure properties such as the direct band gap around 1.0-1.5 eV, high absorption in visible region (absorption coefficient over  $10^4 \text{ cm}^{-1}$ ), p-type conductivity and also prominent optoelectronic characteristics attract the attention to the research of CZTSSe based solar cells [19]–[23].

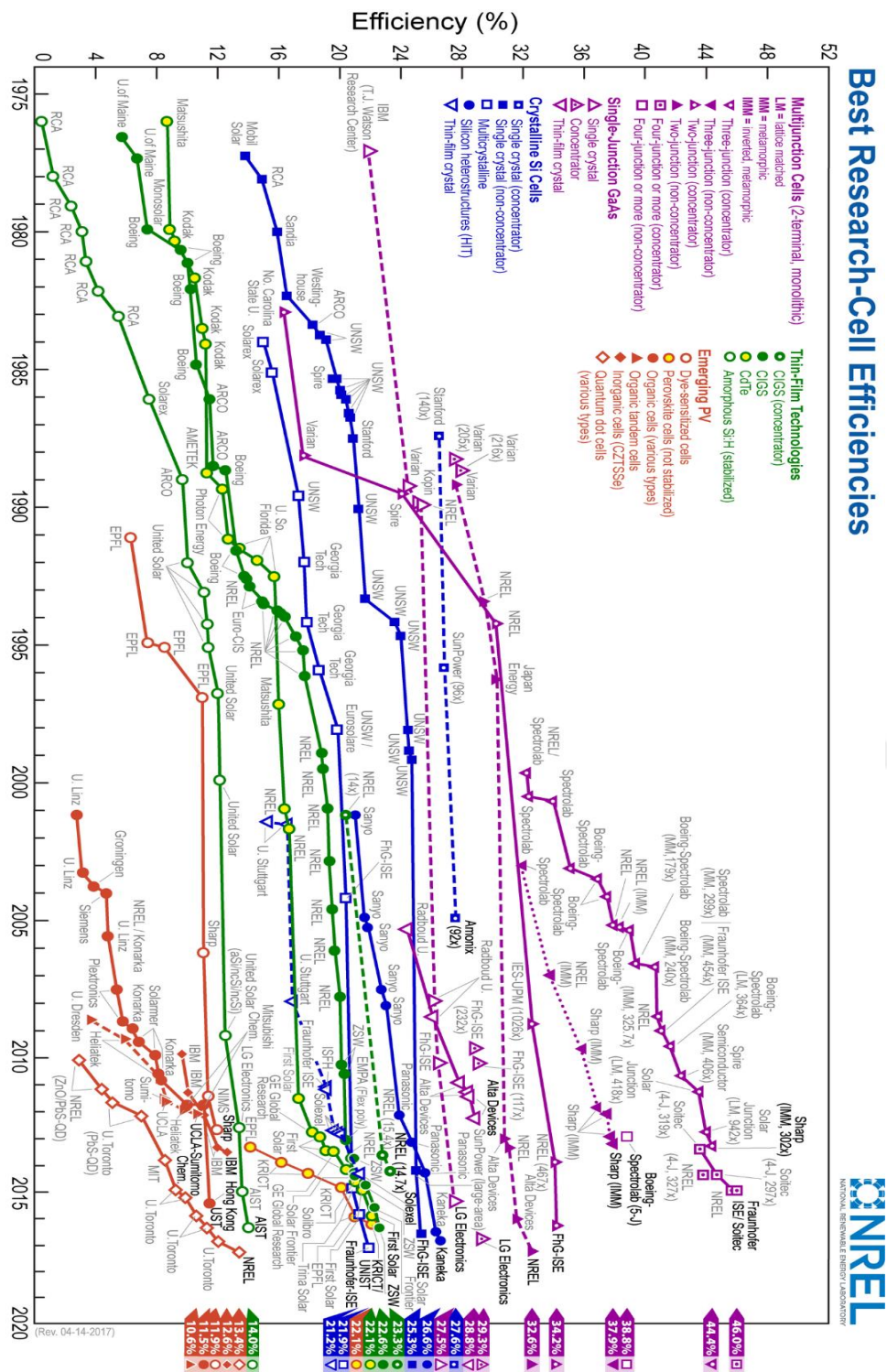


Figure 1.2. NREL' cell efficiency graph [24].

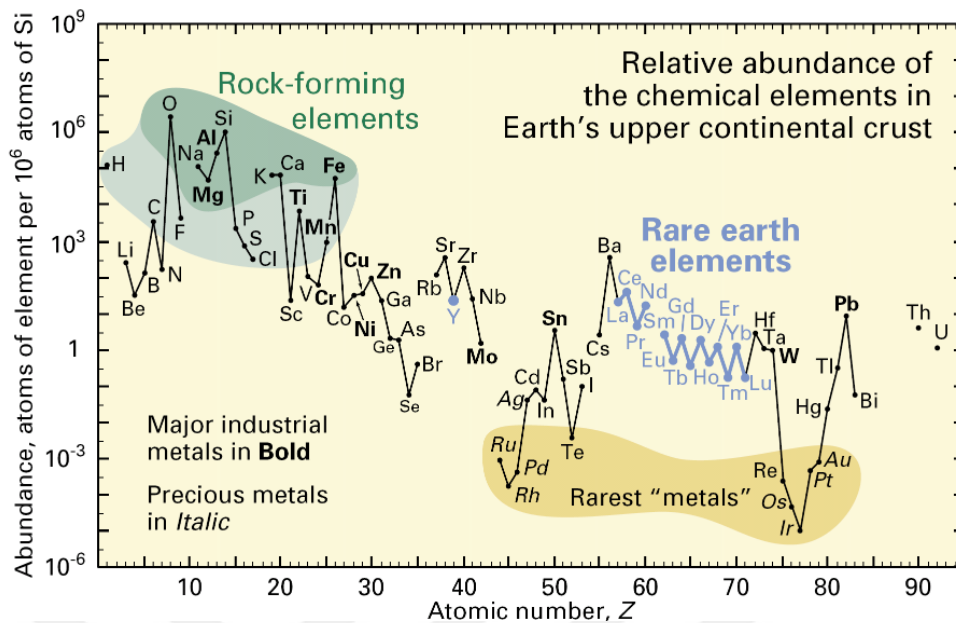


Figure 1.3. Abundance (atom fraction) of chemical elements in Earth's upper continental crust as a function of atomic number. Many of elements are classified into (partially overlapping) categories: (1) rock-forming elements (major elements in green field and minor elements in light green field); (2) rare earth elements (lanthanides, La-Lu, and Y; labeled in blue); (3) major industrial metals (global production  $> \sim 3 \times 10^7$  kg/year; labeled in bold); (4) precious metals (italic); and (5) the nine rarest "metals"-the six platinum group elements plus Au, Re, and Te (a metalloid) [25].

In literature, various deposition methods including pulsed laser deposition [15], thermal evaporation [26], [27], sputtering [28], [29], e-beam evaporation [21], molecular beam epitaxy (MBE) [30], spray pyrolysis [31], [32], sol-gel [33], electro-deposition [34]–[36] were applied for the fabrication of CZTSSe absorber layers. Among them, in 2014, the highest photovoltaic conversion efficiency was reached to 12.6 % by utilizing the hydrazine-based precursor technique, as given in Figure 1.2 [37].

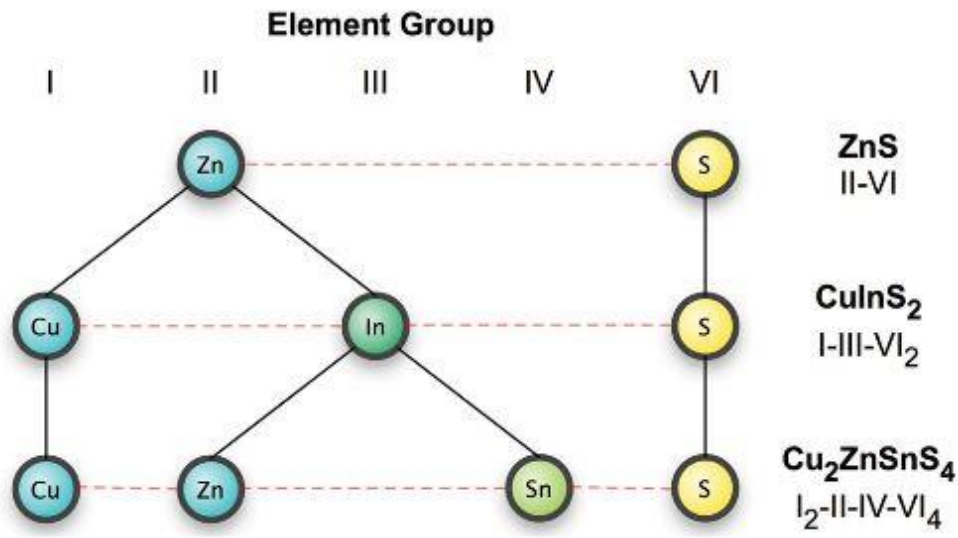


Figure 1.4. The relationship of binary, ternary and quaternary structures [38] .

## 1.2. The Properties of CZTSSe Compound

Crystal structure of CIGS(Se) demonstrates the chalcopyrite structure, while that of CZTS(Se) structure shows either kesterite (space group  $I\bar{4}$ ) or stannite (space group  $I\bar{4}2m$ ) [39], [40]. These structures are similar except the order of Cu and Zn, as shown in Figure 1.5. Kesterite and stannite crystal structures cannot be determined by using X-ray diffraction (XRD) since XRD patterns are the similar due to being isoelectronic of  $\text{Cu}^+$  and  $\text{Zn}^{2+}$ . However, neutron diffraction is an efficient technique to identify the crystal structure because neutrons interact with the nuclei [41]. According to research related to neutron diffraction of CZTSSe compounds, copper zinc tin sulfo selenide structures occur in kesterite structure rather than stannite structure [41].

Calculations based on density functional theory of hybrid functionals indicate that the kesterite is the most stable phase for CZTSSe structures. According to the published phase diagrams of CZTS(Se), secondary phases would exist due to complexity of CZTS(Se) compound [42].

The band gap is the crucial parameter for PV technology and the band gap of 1.5 eV is the optimum band gap for the absorption of the photon. In the majority of research, the band gap of pure sulfide CZTS structure have been found as 1.5 eV nearly while that of pure selenide structure CZTSe have been determined as 1.0 eV using transmission or quantum efficiency measurement in the solar cell [19], [34], [43]–[47].

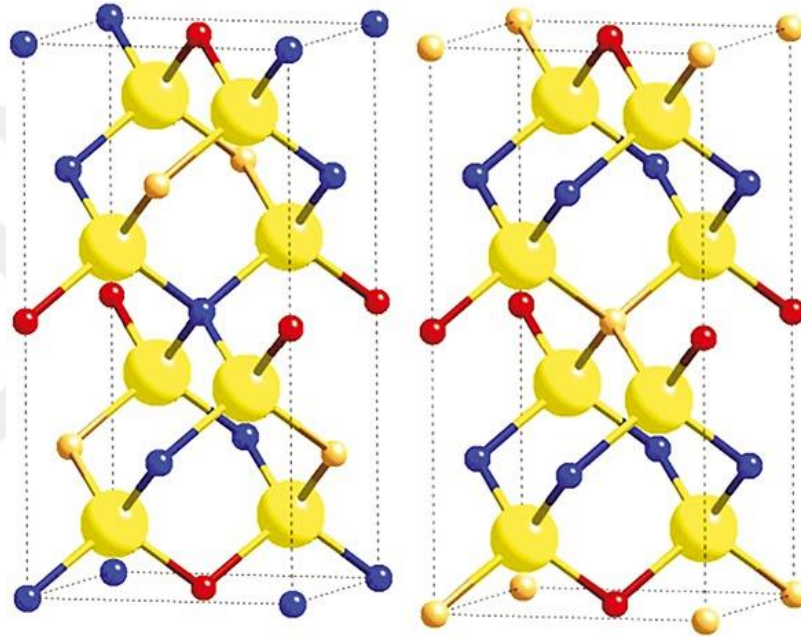


Figure 1.5. Kesterite (left) and stannite (right) crystal structures; large yellow sphere: S and Se; small sphere: blue Cu, yellow Zn, red Sn [41].

To clarify the change of CZTSSe band gap, mathematical expression is defined as follows [48],

$$E_g(\text{CZTSSe}) = (1 - x)E_g(\text{CZTS}) + xE_g(\text{CZTSe}) - bx(1 - x) \quad (1.1)$$

where  $x$  is the ratio of Se/(Se+S) and  $b$  is bowing parameter to be 0.1 eV. In addition, CZTSSe is self-doped material like the CIGS via the formation intrinsic defects such as vacancies ( $V_{\text{Cu}}$ ,  $V_{\text{Zn}}$ ,  $V_{\text{Sn}}$ ,  $V_{\text{S}}$ , etc.), antisite defects ( $\text{Cu}_{\text{Zn}}$ ,  $\text{Zn}_{\text{Cu}}$ ,  $\text{Cu}_{\text{Sn}}$ ,  $\text{Sn}_{\text{Cu}}$ , etc.) and

interstitial defects ( $\text{Cu}_i$ ,  $\text{Zn}_i$ , and  $\text{Sn}_i$ ). Also, CZTSSe structures show p-type conductivity behavior.

### **1.3. Superstrate Configuration of CZTSSe Thin Film Based Solar Cells**

In general, CZTSSe thin film based solar cells have been fabricated in substrate configuration with a hole collecting molybdenum (Mo) back contact, which is the well-known configuration of CIGS technology [49]. However, the reported conversion efficiencies of CZTSSe based solar cells are much lower than those of CIGSe based ones, so far (Figure 1.2) [50]. The gap between the performance of CIGS and CZTSSe based solar cells could be related to some interface problems such as the aggressive reaction between the CZTSSe absorber layer and Mo back contact layer during thermal processing [49]. This leads to an undesirable Schottky barrier at the CZTSSe/Mo interface [51], [52]. High interface recombination and high series resistance have been reported as other problems limiting the device performance [53], [54]. Considering the high efficient CdTe solar cells in superstrate configuration, it is believed that superstrate configuration can be used to tackle some of the above-mentioned problems of CZTSSe solar cells [51]. When compared with substrate configuration, superstrate configuration has several potential advantages such as a reduction in material consumption and process time since it requires a thinner window and absorber layers [55], [56]. It offers a more suitable way of construction of tandem cell applications. Moreover, the aim of research related to kesterite solar cells has recently shifted to superstrate-type configuration to further unlock the potential of kesterite [49], [51], [53], [57].

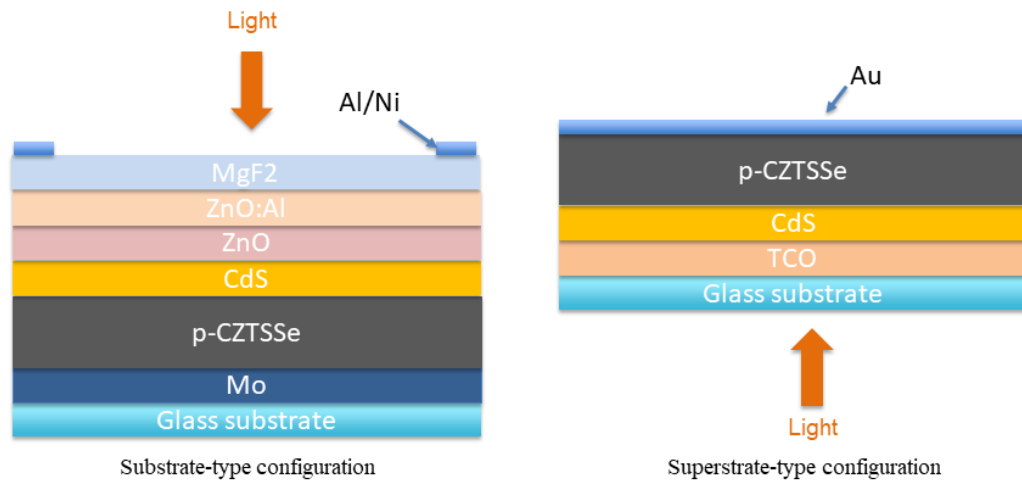


Figure 1.6. Substrate and superstrate configurations of CZTSSe based solar cells.

The evolution of CZTSSe in superstrate configuration; the early attempts started with Kurowaka et al. in 2012. Using the device structure of SLG/FTO/dense TiO<sub>2</sub>/nc-TiO<sub>2</sub>/CZTS/graphite, the power conversion efficiency was achieved as 0.51 %, and CZTS was deposited by spray pyrolysis deposition technique [58]. Moreover, in 2012, Chen et al. reported research in which device structure of SLG/TiO<sub>2</sub>/In<sub>2</sub>S<sub>3</sub>/CZTS/carbon was prepared entirely non-vacuum based processes, and they achieved 0.6 % conversion efficiency [59]. In 2013, Tanaka et al. performed the research utilizing the structure of SLG/FTO/dense TiO<sub>2</sub>/nc-TiO<sub>2</sub>/CZTS/graphite in which CZTS layer was coated by spray pyrolysis deposition and conversion efficiency was obtained as 1.13 % [60]. In 2014, Lee et al. reported the study preparing CZTSSe thin films by using spin coating and achieved 1.2 % efficiency utilizing the structure of SLG/ITO/ZnO/CdS/CZTS/Au [57]. Also, in 2014, Wang et al. reported research using SLG/ITO/CdS/CZTSSe/Au and power conversion efficiency was about 1.1 % in which CZTSSe nanocrystals were produced by hot injection method [61]. In 2016, Zhang et al. reported study CZTSe thin film deposited by spin coating and efficiency of SLG/ITO/CdS/CZTSe/carbon structure was achieved as 2.44 % [49]. Then, in 2017, the efficiency of SLG/FTO/TiO<sub>2</sub>/In<sub>2</sub>S<sub>3</sub>/CZTS/graphite was reported to be 3.5 %

by Berrut et al. CZTS was coated by electrodeposition in this study [53]. In 2018, lastly, Wang et al. announced the highest efficiency record as 5 % for superstrate configuration of SLG/FTO/TiO<sub>2</sub>NR/Al<sub>2</sub>O<sub>3</sub>/CdS/CZTS/Spiro-OMeTad/Au [62].

#### **1.4. Outline of This Thesis**

This thesis study is intended to produce low-cost CZTSSe thin film utilizing physical vapor deposition techniques and investigate the physical properties of deposited films. One of the aims is to study the current conduction mechanism of CZTSSe/Si structure in details. The other one is to fabricate and characterize CZTSSe thin film based solar cells in superstrate configurations. The study given in this thesis includes seven chapters.

The first chapter is an introduction to current photovoltaic technologies. The advantages and challenges of different PV technologies are discussed. The main focus is on thin film photovoltaics which based on chalcogenide compounds such as kesterites. Fundamental properties of CZTSSe thin film and CZTSSe based solar cell structures in substrate and superstrate configuration are explained. The advantages of superstrate configurations are discussed in details and states of the art superstrate CZTSSe solar cells are given. Following this, the objectives of this thesis are presented.

The second chapter is based on theoretical fundamentals required to explain the physics and operation principle of basic solar cell structure.

The third chapter is the experimental procedures of the CZTSSe thin film deposition. In addition, measurement techniques and setups are explained in detailed.

The fourth chapter presents the single-step deposition of CZTSSe thin films by thermal evaporation and investigation of diode properties of CZTSSe/Si structure. The first part of the chapter is focused on the determining structural, optical, and electrical properties of deposited thin films, and the following section is about the current

conduction mechanism of CZTSSe/Si structure. The results of temperature-dependent current-voltage (I-V) and frequency dependent capacitance-voltage (C-V) measurements are discussed.

The fifth chapter is about the novel fabrication technique to deposit CZTSSe thin film having self-assembled vertical nanoflakes utilizing RF magnetron sputtering. The main body of this chapter is based on the mechanism behind the formation of self-assembled nanoflakes and the effect of precursor thickness on the size of nanoflakes on the film surface. In addition, the impact of substrate temperature on the formation nanoflakes on CZTSSe thin film is discussed.

The sixth chapter is about the CZTSSe thin film based solar cell in superstrate configuration. The first part of this chapter presents the results of the ITO/CdS/CZTSSe/Au structure. In the following part, the effect of TiO<sub>2</sub> layer on the device performance is investigated in detailed.

The final chapter includes a general conclusion and interpretations of this study.



## CHAPTER 2

### THEORETICAL CONSIDERATIONS

#### 2.1. Absorption of Light

When semiconductors interact with light, the optical phenomena such as absorption, transmission and reflection occurs. Using these optical effects, valuable information about the energy band structure of semiconductors can be obtained.

The absorption can happen through several transition paths. These are band to band, donor to conduction band, interconduction band, intervalance band, acceptor to conduction band, valance band to donor, acceptor to conduction band and donor to acceptor transitions as indicated in Figure 2.1. The energy of incident photon determines the type of transition. That is, if the semiconductor absorbs photon which has energy larger than forbidden band gap of semiconductor, transition of electron from filled valance band to empty conduction band states occurs. This phenomena is called as ‘‘fundamental absorption’’[63], [64]. On the other hand, when absorbing photon which has the energy below the band gap of semiconductor, this results in absorption by excitons or transition of electrons between impurity (donor or acceptor) and energy band states (conduction or valance bands).

These electron transitions play an important role in technological applications. For example, operation principle of intrinsic photodetectors is based on band to band absorption, while semiconductor lasers rely on the transitions between impurity and band states[64].

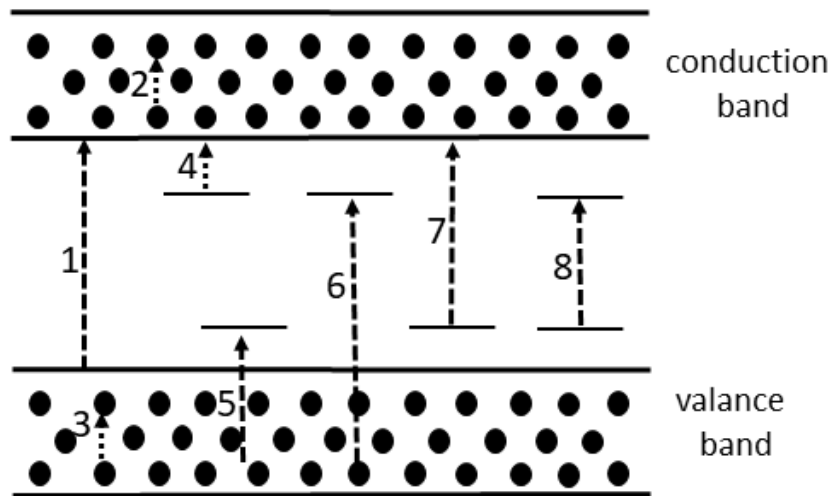


Figure 2.1. Simplified illustration of different optical absorption processes in semiconductors: (1) band to band, (2) interconduction band, (3) intervalance band, (4) donor to conduction band, (5) valance band to acceptor, (6) valance band to donor, (7) acceptor to conduction band and (8) acceptor to donor transitions.

## 2.2. Direct and Indirect Band Gap Semiconductor

Fundamental absorption can be divided into two groups in semiconductors: direct and indirect band to band transitions. In such physical processes, both momentum and energy must be conserved. In a direct band gap semiconductor, after the absorption of photon by semiconductor, electrons is excited from the valance band to conduction band directly without a change in crystal momentum since the momentum of photon is negligible. On the other hand, in indirect band gap semiconductor, transition occurs from the valance band maximum ( $\Gamma$  valley) to conduction band minimum ( $X$  valley) by accompanying a phonon. That is, there is a change in crystal momentum of semiconductor. In indirect transition, photon interaction with valance electron require a lattice vibration. For this reason, the probability of photon absorption is weaker than direct transitions. Energy versus crystal momentum behaviors of direct and indirect semiconductors are given in Figure 2.2.

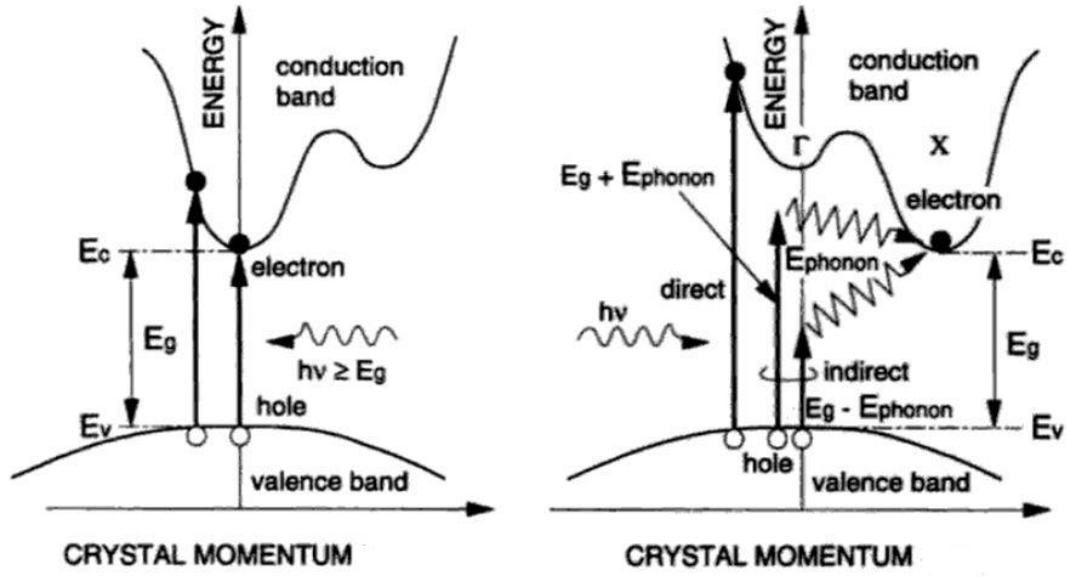


Figure 2.2. Energy-crystal momentum diagram of direct and indirect band gap semiconductor [65].

### 2.3. Absorption Coefficient

Using the transmittance ( $T$ ) and reflectance ( $R$ ) spectrum of a sample, the absorption coefficient ( $\alpha$ ) can be found experimentally as a function of wavelength with the help of the following expression [66],

$$T = \frac{(1 - R)^2 \exp(-\alpha t)}{1 - R^2 \exp(-2\alpha t)} \quad (2.1)$$

where  $t$  is the thickness of sample. For the large ( $\alpha t$ ) values, this equation becomes,

$$T = (1 - R)^2 \exp(-\alpha t) \quad (2.2)$$

In addition, absorption coefficient is defined as the following equation [67],

$$\alpha(h\nu) = A \sum p_{if} n_i n_f \quad (2.3)$$

where  $p_{if}$  is the probability of transition from the initial state to final state,  $n_i$  is the electron density in the initial state,  $n_f$  is the empty states density in the final states. Transition probability does not depend on the photon energy. With respect to parabolic bands (Figure 2.2.),

$$E_f - E_c = \frac{p^2}{2m_e^*} \quad (2.4)$$

and

$$E_i - E_v = \frac{p^2}{2m_h^*} \quad (2.5)$$

In a direct material, transition is defined by,

$$h\nu - E_g = \frac{\hbar^2 k^2}{2} \left( \frac{1}{m_e^*} + \frac{1}{m_h^*} \right) = \frac{\hbar^2 k^2}{2m_r^*} \quad (2.6)$$

where  $m_r^*$  is the reduced effective mass and given by,

$$\frac{1}{m_r^*} = \frac{1}{m_e^*} + \frac{1}{m_h^*} \quad (2.7)$$

The density of states (DOS) is defined by the following expression,

$$N(h\nu)d(h\nu) = \frac{8\pi k^2}{(2\pi)^3} dk \quad (2.8)$$

$$N(h\nu)d(h\nu) = \frac{(2m_r^*)^{3/2}}{2\pi^2 \hbar^3} (h\nu - E_g)^{1/2} d(h\nu) \quad (2.9)$$

So, the absorption coefficient as a function of energy for direct transition with respect to parabolic bands is found as,

$$\alpha(h\nu) = A(h\nu - E_g)^{1/2} \quad (2.10)$$

where A is a constant having the value of  $2 \times 10^4$  when  $h\nu$  and  $E_g$  are expressed in eV and  $\alpha$  is expressed in  $\text{cm}^{-1}$ .

In an indirect material, on the other hand, phonon having energy  $E_p$  is either emitted or absorbed to conserve the momentum during the transition. According to Bose Einstein statistics, the number of phonons is given as,

$$N_p = \frac{1}{\exp\left(\frac{E_p}{kT}\right) - 1} \quad (2.11)$$

where k and T are the Boltzmann constant and absolute temperature, respectively. During the transition, if the phonon absorption occurs, absorption coefficient is defined as,

$$\alpha_a(h\nu) = \frac{A(h\nu - E_g + E_p)^2}{\exp\left(\frac{E_p}{kT}\right) - 1} \quad (2.12)$$

If the phonon emission occurs, it is defined as,

$$\alpha_e(h\nu) = \frac{A(h\nu - E_g - E_p)^2}{1 - \exp\left(\frac{E_p}{kT}\right)} \quad (2.13)$$

Both phonon absorption and emission are possible in the case of  $h\nu > E_g + E_p$ , absorption coefficient can be found as follows,

$$\alpha(h\nu) = \alpha_a(h\nu) + \alpha_e(h\nu) \quad (2.14)$$

## 2.4. The Solar Radiation

The solar irradiation on the outside of the surface of the earth's atmosphere is close to black body radiation which corresponds to 5800 K nearly [68]. When sunlight passing through the atmosphere, it is attenuated by at least 30% due to some reasons. The reasons of such attenuation may be due to [63] ;

- i. scattering by molecules in the atmosphere.
- ii. scattering by dust particles.
- iii. absorption by the atmosphere and its constituent gases.

The wavelengths which is less than 300 nm is filtered out by nitrogen, ozone or oxygen. On the other hand, water and carbon dioxide absorb in the infrared considerably. Water is responsible for the dips in the spectrum at 900, 1100, 1400 and 1900 nm, while carbon dioxide is at 1800 and 2600 nm [68]. Attenuation is variable with respect to the length of sunlight path through the atmosphere and it is quantified by the Air mass defined as follows,

$$\text{Air mass} = \frac{1}{\cos \theta} \quad (2.15)$$

where  $\theta$  is angle between vertical axis and position of the sun (zenith angle). The solar spectrum outside the atmosphere of Earth's is called as AM0. When the sun is perpendicular to the surface of earth's directly, the radiation is defined as AM1.

The standard terrestrial solar spectrum is defined as AM1.5 in which sunlight comes with an angle of  $48.^\circ$ . AM1.5 spectrum is called also as AM1.5G and "G" stands for "global". AM1.5G is normalized to irradiance of  $1000 \text{ W/m}^2$ . The response of photovoltaic device depends mainly on the band gap of the semiconductor material. The spectral distributions of AM0 and AM1.5G with the band edges of several photovoltaic materials are given in Figure 2.3.

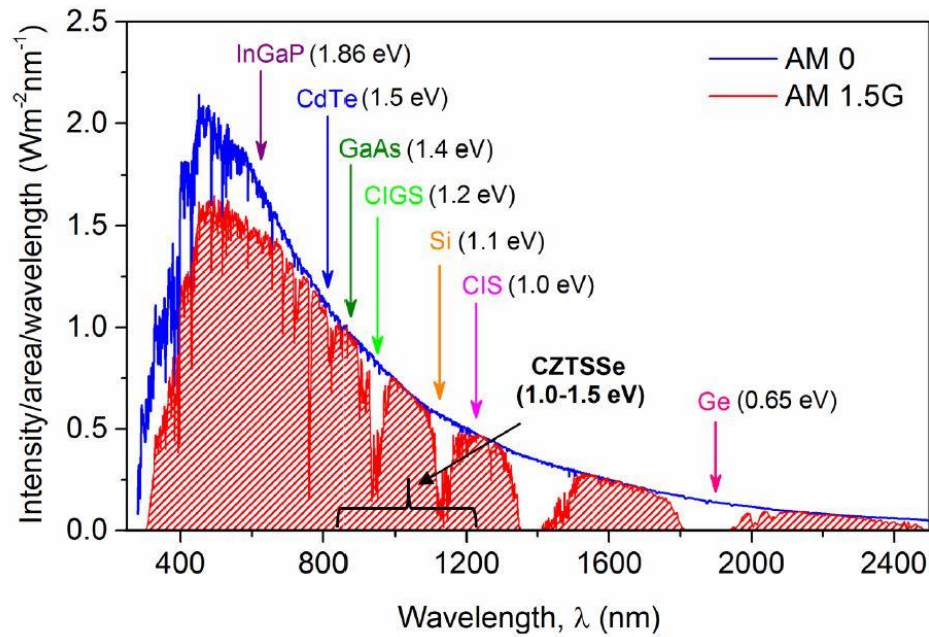


Figure 2.3. Solar irradiance spectrum [69].

## 2.5. Metal-Semiconductor Junction

When metal and semiconductor are in contact, there can be two types of contact behavior: rectifying and non-rectifying. The formed rectifying contact between metal and semiconductor is called as Schottky junction, while the non-rectifying one is called as ohmic contact. Difference in the work functions of metal and semiconductor causes such a behavior [70].

### 2.5.1. Schottky Junction

The energy band structures of the metal- semiconductor junction in the case that metal is away from the semiconductor and they are in contact as given in Figure 2.4. The work function is defined as the energy difference between vacuum level and Fermi level. Besides, work function of metal and semiconductor are labelled as  $q\phi_m$  and  $q\phi_s$ , respectively. As shown in the figure, the Fermi level of metal,  $E_{Fm}$ , lies in the band. When the position of the Fermi level of metal is lower than that of

semiconductor (in the case of  $\phi_m > \phi_s$ ), this leads to formation of Schottky barrier. This situation is illustrated in Figure 2.4. When the junction is formed between metal and semiconductor, flow of charges occurs until both Fermi levels line up at same position. This flow creates the depletion region (W) in the semiconductor side. As a result of formation of a dipole system at the junction, there is also built-in electric field ( $E_0$ ) from the positive charges to negative charges. However, the contact potential, which is called as built-in potential  $V_0$ , prevents further flow of electron from conduction band of semiconductor to metal. Built-in potential is defined as difference in work function potentials  $\phi_m - \phi_s$ . The potential barrier height called as Schottky barrier ( $\Phi_B$ ) for electron injection from the metal to conduction band of semiconductor is [71],

$$\Phi_B = \phi_m - \chi \quad (2.16)$$

Where  $q\chi$  is the electron affinity, corresponding to energy from the bottom of the conduction band to vacuum level.

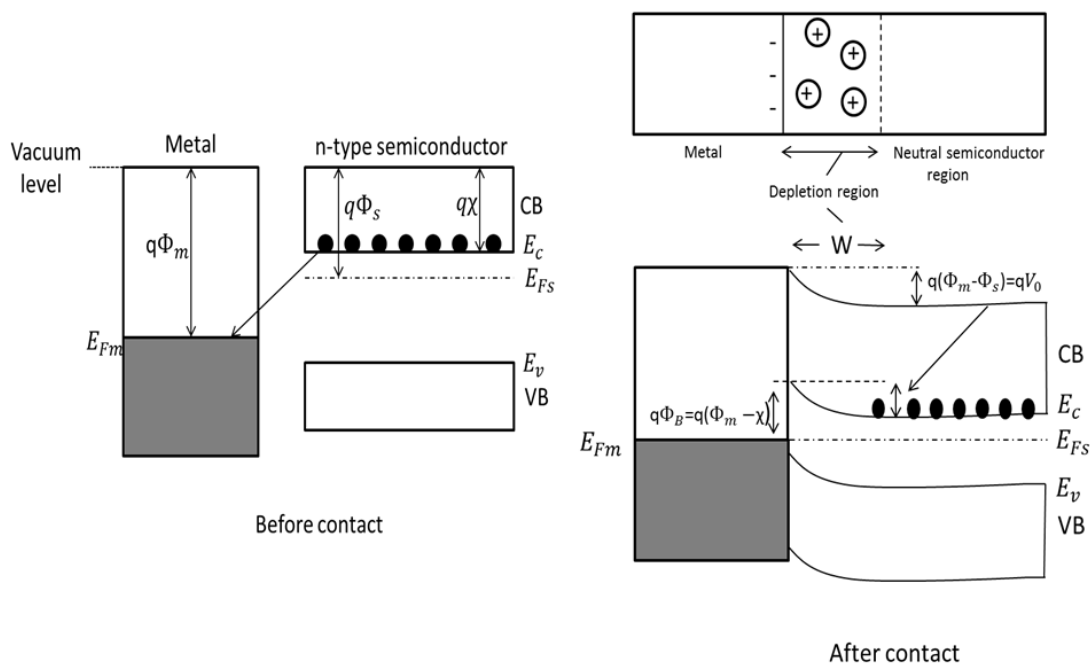


Figure 2.4. Schottky barrier formation by contacting n-type semiconductor with a metal.

Schottky junction can also be obtained in a similar way between a metal and p-type semiconductor in the case of  $\phi_m < \phi_s$ .

On the other hand, when applying a forward bias voltage to the Schottky barrier, the voltage drop is across the depletion region having higher resistance than both metal and neutral region of semiconductor. Thus, the contact potential becomes  $V_0 - V$  and  $\Phi_B$  remains unchanged as shown in Figure 2.5. In this case, electrons can overcome from the conduction band of semiconductor into metal easily, which leads to an increase in forward current through the junction. Conversely, applying a reverse bias increases the contact potential as  $V_0 + V_r$  since the depletion region is highly resistive due to having very few carriers. Electron movement from the semiconductor to metal is negligible. The current is based on the thermal emission of electrons that move over the barrier  $\Phi_B$  from the metal into the semiconductor as illustrated in Figure 2.5.

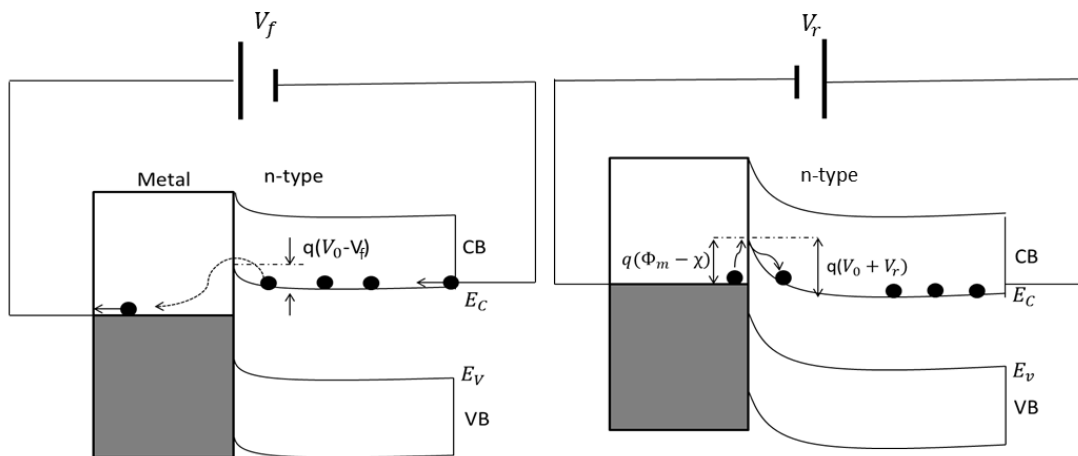


Figure 2.5. Schottky junction under the forward and reverse bias for n-type semiconductor.

The I-V profile of Schottky junction exhibits rectifying behavior as mentioned above and it is called as Schottky diode. The resulting diode equation is given by [70],

$$I = I_0 \left( e^{qV/nkT} - 1 \right) \quad (2.17)$$

where  $k$  is the Boltzmann constant,  $T$  is the temperature,  $n$  is the ideality factor and  $I_0$  is reverse the saturation current defined as the following equation,

$$I_0 \propto e^{-q\Phi_B/kT} \quad (2.18)$$

### 2.5.2. Ohmic Contact

Ohmic contact is a junction that can be formed between metal and semiconductor. It does not limit the current flow and it has a linear, non-rectifying I-V characteristic. The importance of such a contact is having minimal resistance. The ohmic contact between a metal and n-type semiconductor is given in Figure 2.6.

In the case of  $\phi_m < \phi_s$  (n-type), both Fermi levels are line up by tunneling of more energetic electron from the metal into the semiconductor at equilibrium.

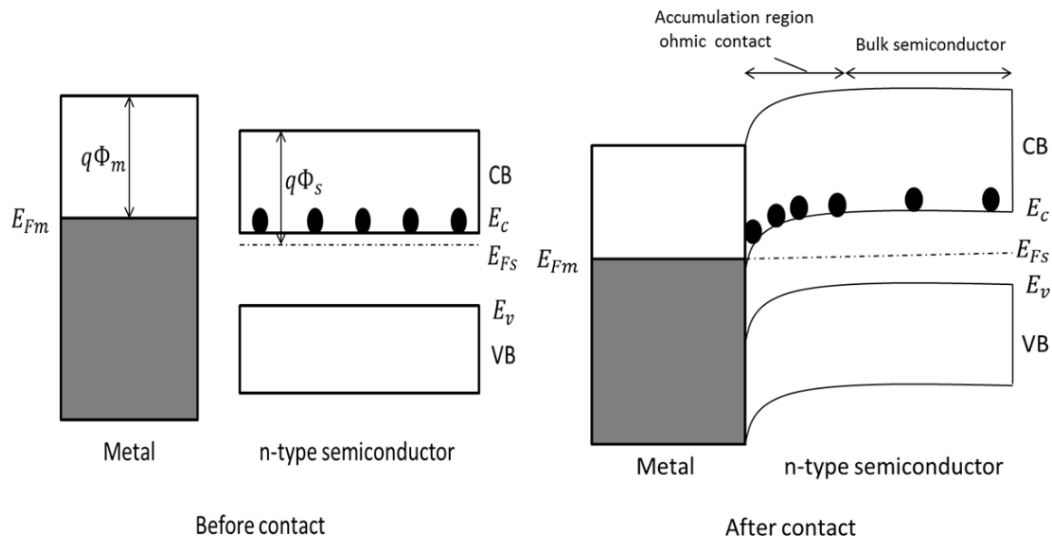


Figure 2.6. Ohmic contact between metal and n-type semiconductor.

Consequently, electrons accumulate in the conduction band of semiconductor near the junction and this region is called as accumulation region. When preventing further electron tunneling by accumulated electrons in the conduction band, equilibrium is reached.

In a similar way, in the case of  $\phi_m > \phi_s$  (p-type), ohmic contact is obtained. Hole flow across the junction can occur easily.

## 2.6. Physics of p-n Junction

It is well-known that n-type semiconductors have a high electron concentration and hole concentration. However, in p-type semiconductors, this is vice versa. In doped semiconductors, majority carrier concentration is higher in doped semiconductors. For example, electrons are the majority carriers for n-type materials, while they are minority carriers for p-type materials. When p-type and n-type semiconductor are in a contact, a p-n junction forms between the two material and this phenomena is the same as both homo-junctions and hetero-junctions. The formation of a junction results in diffusion of electrons from n-type region to p-type region and diffusion of holes from p-type region to n-type region. The concentration gradient of carriers leads to diffusion of them. Electrons diffusing to p-type region recombine with holes near the junction. Similarly, holes diffusing into the n-type region recombine with electrons. Thus, junction region is depleted of free carriers when comparing to bulk region of semiconductors. And so, space charge region (SCR) forms in the junction including opposite charged ions called as donors and acceptors as shown in Figure 2.7 (a). This region is also called as depletion region or transition region. The other part of both semiconductors is called as quasi-neutral region (QNR). Opposite charge ions results in internal electric field from the positive ions to negative ions in the SCR. This electric field fights the diffusion of carriers so that it drives the holes and electrons to the opposite direction of diffusion. Since there is no net current through the junction at equilibrium, diffusion current of electron will be balanced by the drift current of

electrons resulting from the electric field. Similarly, the diffusion current of holes cancels by the drift current of holes. These expressions are given as below [70],

$$J_p(\text{drift}) + J_p(\text{diffusion}) = 0 \quad (2.18)$$

$$J_n(\text{drift}) + J_n(\text{diffusion}) = 0 \quad (2.19)$$

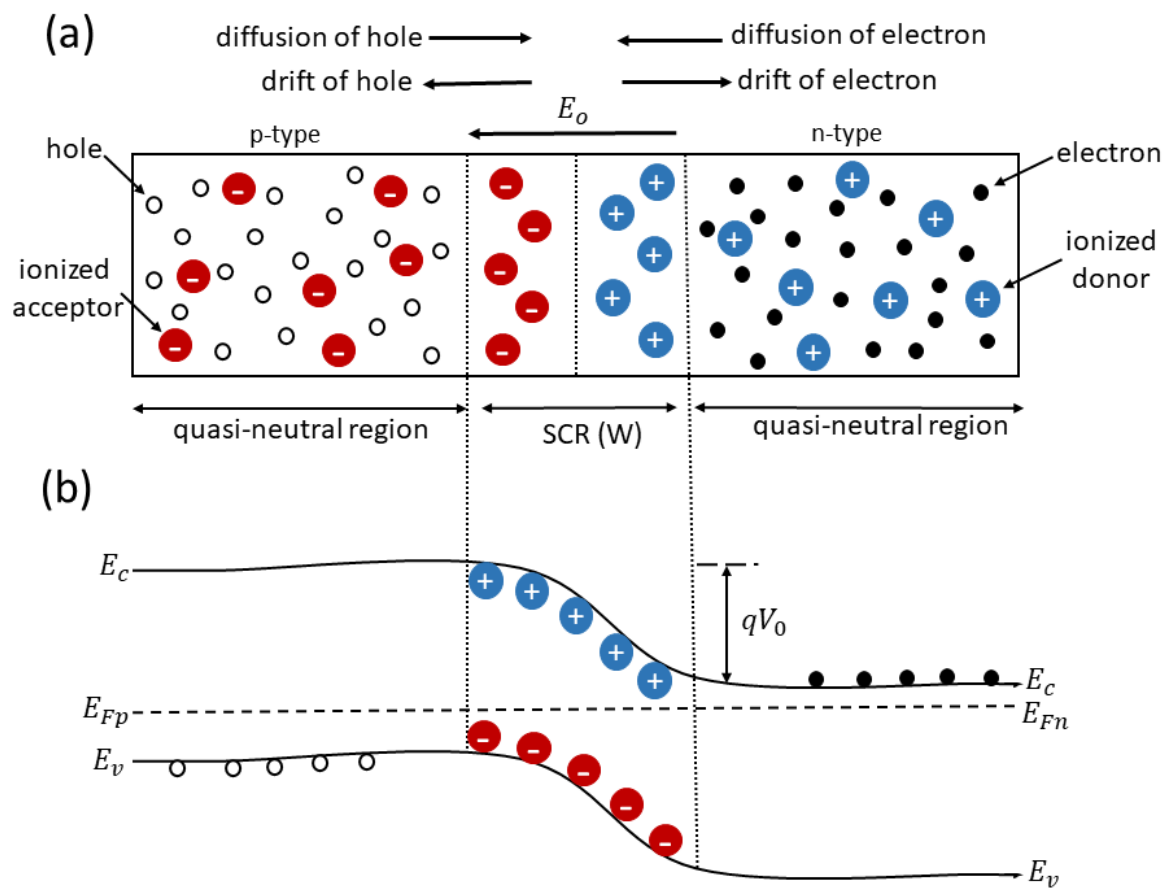


Figure 2.7. Schematic diagram of (a) p-n junction, (b) band alignment in equilibrium. Donor atoms (blue particles), acceptor atoms (red particles), electrons (black particles) and holes (white particles).

When equilibrium is reached, the potential difference occurs across the junction and it is called as built in potential (or contact potential). As indicated in Figure 2.7 (b),

the built-in potential is labelled as  $V_0$ . To find  $V_0$  in terms of donor ( $N_d$ ) and acceptor ( $N_a$ ) concentrations, drift and diffusion current equations must be used for equilibrium condition. For example, the sum of drift and diffusion current is equal to zero at equilibrium and it is expressed as follows [70],

$$J_p(x) = q \left[ \mu_p p(x) E(x) - D_p \frac{dp(x)}{dx} \right] = 0 \quad (2.20)$$

This equation becomes,

$$\frac{\mu_p}{D_p} E(x) = \frac{1}{p(x)} \frac{dp(x)}{dx} \quad (2.21)$$

And the electric field can be expressed in terms of gradient of potential, so Eqn. 2.21 becomes,

$$-\frac{q}{kT} \frac{dV(x)}{dx} = \frac{1}{p(x)} \frac{dp(x)}{dx} \quad (2.22)$$

with the help of the Einstein relation for  $\mu_p/D_p$ . Applying the appropriate limits to the Eqn 2.22,  $V_0$  is easily obtained as,

$$V_0 = \frac{kT}{q} \ln \frac{N_a N_d}{n_i^2} \quad (2.23)$$

where  $n_i$  intrinsic carrier concentration of semiconductor. In addition, width of the depletion region ( $W$ ) is calculated by using the Poisson's equations under the assumption of depletion region approximation and it is found as,

$$W = \left[ \frac{2\varepsilon(N_a + N_d)V_0}{qN_a N_d} \right]^{1/2} \quad (2.24)$$

## 2.7. Operating Principles of Solar Cells

To explain the operating principles of solar cell, a schematic diagram of typical solar cell is given in Figure 2.8. There is a p-n junction having very narrow and heavily doped n side where the depletion region extends into p side. This solar cell is illuminated by the n-type region due to being thin region. There must be electrodes on both front and back sides of p-n junction in a typical solar cell. Electrode on front side should be array of finger electrodes so that they allow the illumination. Due to having narrow the n region, majority of absorption process of photon and generation of electron-hole pairs (EHPs) occur in both the depletion region ( $W$ ) and quasi neutral p-region ( $l_p$ ). Built-in electric field in depletion region separates the photo-generated EHPs each other. The electron which is drifted by built-in electric field into the quasi neutral n-region makes the n-side negative by amount of charge  $-e$ .

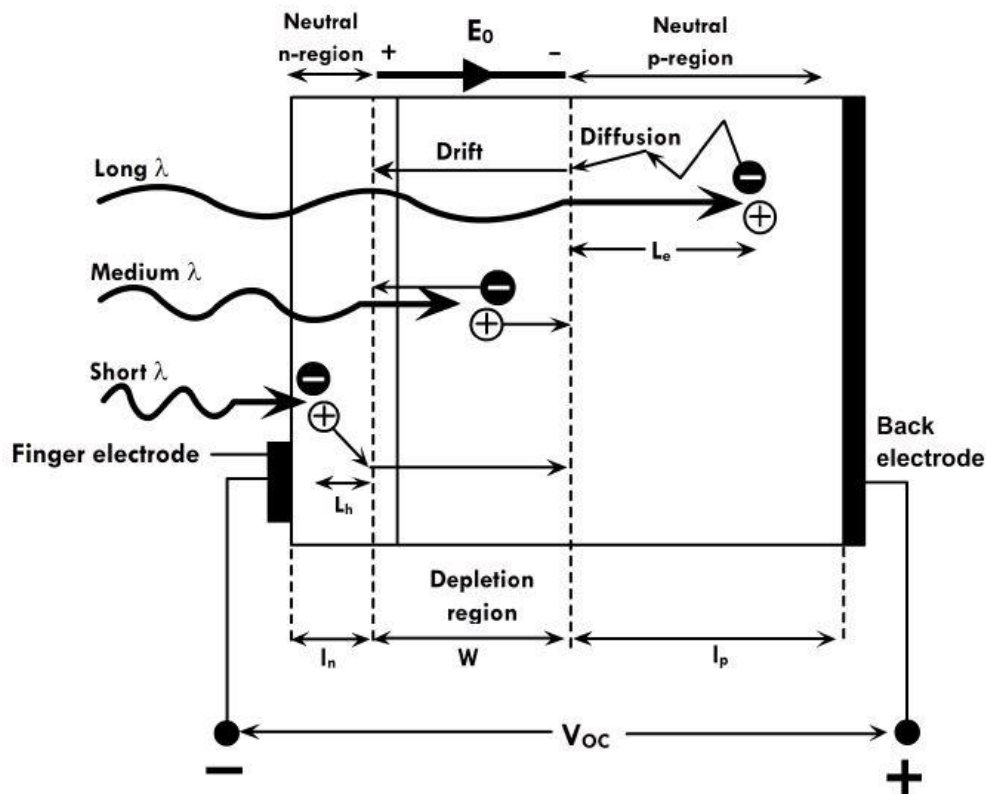


Figure 2.8. The operating principle of typical solar cell [71].

Likewise, the hole which reaches the quasi neutral p-region makes p-side positive. This results in formation of open circuit voltage between the terminals of solar cell. With connecting an external load, the excess electrons which are located in quasi neutral n-region move through the external circuit and they reach p-side and recombine with the excess hole in p-region. Long-wavelength photons are absorbed by quasi neutral p-region, which results in photogenerated EHPs (shown in Figure 2.8). The electron can diffuse in the p-side by minority carrier distance which is labelled as  $L_e$ . In addition,  $L_e$  is given as follows [71],

$$L_e = \sqrt{2D_e\tau_e} \quad (2.25)$$

where  $D_e$  and  $\tau_e$  are the diffusion coefficient and recombination lifetime of electron, respectively. So, electrons in a distance  $L_e$  can diffuse to depletion region. And then, those electrons are drifted by built-in electric field to the quasi neutral region. Similarly, photogenerated holes which are located in distance  $L_h$  can reach to the p-side. Thus, it can be deduced that only photogenerated electron or holes which are in the minority carrier diffusion length ( $L_e$  or  $L_h$ ) can contribute to the photovoltaic effect.

When solar cell is in short circuit, the only current through the circuit is due to flow of photogenerated EHPs. This current is called as photocurrent ( $I_{ph}$ ) and shown in Figure 2.9. Another name of this current is short circuit current ( $I_{sc}$ ). However, by definition, short circuit current has opposite direction with photocurrent ( $I_{sc} = -I_{ph}$ ). When considering the presence of external load R, there is a voltage appearing across the p-n junction. So, built-in potential of p-n junction decreases with the help of this voltage, which leads to minority carrier injection and increases current [71].

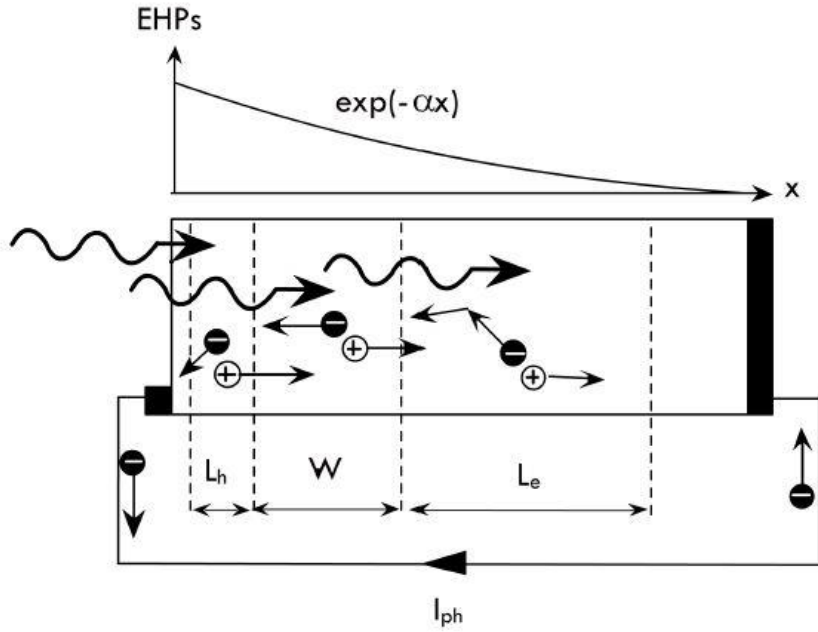


Figure 2.9. The variation of photogenerated EHPs concentration with distance due to absorption of light (taken from [71] ).

Thus, the net current through the solar cell can be written as,

$$I = -I_{ph} + I_0 \left[ \exp\left(\frac{qV}{nkT}\right) - 1 \right] \quad (2.26)$$

Where  $I_0$  is the reverse saturation current,  $n$  is the ideality factor,  $k$  is the Boltzman constant,  $V$  is the external voltage and  $T$  is the temperature.

In the case of open circuit, the total current is zero. This is expressed as follows,

$$I_{ph} = I_0 \left[ \exp\left(\frac{qV_o}{nkT}\right) - 1 \right] \quad (2.27)$$

Assuming  $V_{oc} \gg \frac{nkT}{q}$ ,  $V_{oc}$  is found by using the Eqn 2.27,

$$V_{oc} \approx \frac{nkT}{q} \ln\left(\frac{I_{ph}}{I_0}\right) \quad (2.28)$$

Eqn 2.28 indicates that the lower  $I_0$  leads to higher  $V_{oc}$ .

## 2.8. Solar Cell Parameters

Current density-voltage (J-V) curves of a solar cell under dark and illumination are given in Figure 2.10 where current density is defined as current per unit area. It can be seen that J-V profile shifts by short circuit current density ( $J_{sc}$ ) under illumination. Conventionally, J-V curve of solar cell is characterized by 4<sup>th</sup> quadrant and basic photovoltaic cell parameters are extracted by means of this curve.

$J_{sc}$  is the current density generated by illuminating of solar cell which is in short circuit. By definition,  $J_{sc}$  is equal to  $-J_{ph}$  and it depends on intensity of light. Short circuit current density of solar cell is found the point where J-V curve cuts the J axis at  $V=0$ .

Another important parameter of solar cell is open circuit voltage ( $V_{oc}$ ). It is the voltage output of illuminated solar cell when there is no external load. The point cutting the V axis ( $J=0$ ) of J-V curve gives  $V_{oc}$  as shown in Figure 2.10.

Fill factor (FF) is a parameter which determine the quality of solar cell. It is defined as [72],

$$FF = \frac{J_m V_m}{J_{sc} V_{oc}} \quad (2.29)$$

where  $J_m$  and  $V_m$  are the points which give the maximum power output indicated by shaded area in Figure 2.10. In addition, FF is introduced as a function of  $V_{oc}$  as follows [73],

$$FF = \frac{v_{oc} - \ln(v_{oc} + 0.72)}{v_{oc} + 1} \quad (2.30)$$

where  $v_{oc}$  is the dimensionless voltage and it is expressed as  $v_{oc} = qV_{oc}/kT$ . However, this equation is for ideal solar cell (with no series and shunt resistances)

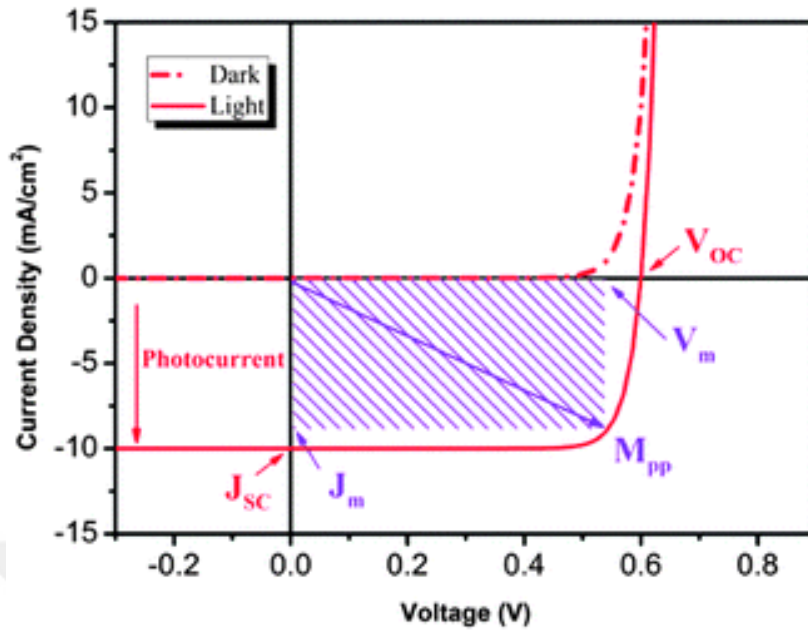


Figure 2.10. Typical current density-voltage characteristics of a solar cell [74].

Power conversion efficiency,  $\eta$ , is the most important parameters for solar cell applications. It is calculated by,

$$\eta = \frac{P_m}{P_i} = \frac{J_m V_m}{P_{in}} = \frac{J_{sc} V_{oc} FF}{P_{in}} \quad (2.31)$$

Solar cells in practice can deviate from the ideal p-n junction solar cell behavior due to some reasons. In an ideal solar cell, the effect of series or shunt resistance is negligible. In Figure 2.11 (a) shows the equivalent circuit of ideal p-n junction solar cell when connecting external load resistance ( $R_L$ ). On the other hand, Figure 2.11 (b) indicates the equivalent circuit of solar cell in practice. Series resistance ( $R_s$ ) of solar cell is introduced by the total resistance of device. It may results from the resistances of front and back contact metals, resistances at interface of layers and bulk resistance of semiconductors. Higher values of  $R_s$  affects the performance of solar cells negatively.  $R_s$  limits the short circuit current and there is no effect of open circuit voltage.

Parallel or shunt resistance ( $R_p$  or  $R_{sh}$ ) of solar cell is a measure of leakage current through the solar cell. Shunt resistance must be higher as much as possible to prevent the leakage current. Low shunt resistance causes decrease in open circuit voltage.

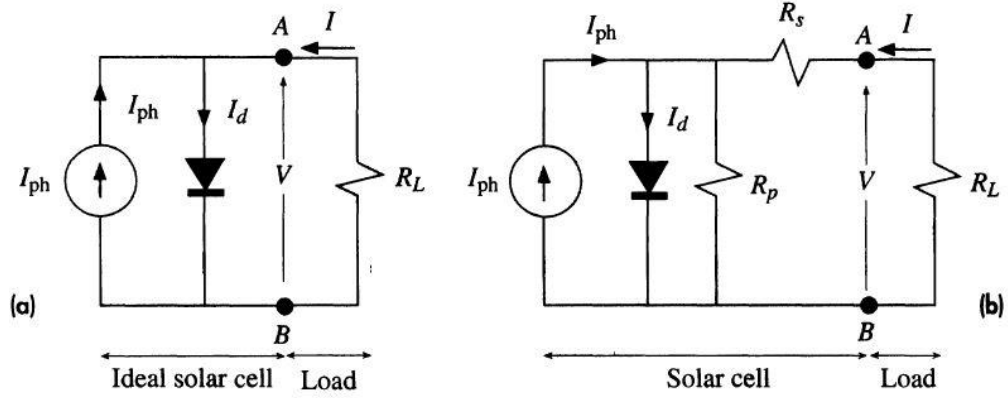


Figure 2.11. Equivalent circuit of solar cell (a) ideal p-n junction, (b) with series and shunt resistances (adopted by Ref. [71] ).

## 2.9. Simulation of CZTSSe Solar Cells in Superstrate Configuration Using SCAPS-1D Software

In this thesis, numerical modelling of CZTSSe thin film based solar cell in superstrate configuration were carried out by using SCAPS (Solar Cell Capacitance Simulator) software. SCAPS is a numerical program to simulate solar cell device structure [75], [76]. This program solves the basic semiconductor equations in one dimension under steady state conditions. These equations are the Poisson and continuity equations for electron and holes. The Poisson equation is given [77],

$$\frac{d^2}{dx^2} \Psi(x) = \frac{q}{\epsilon_0 \epsilon_r} (p(x) - n(x) + N_D^+ - N_A^- + \rho_p + \rho_n) \quad (2.32)$$

where  $\Psi$  is the electrostatic potential,  $q$  is the electrical charge,  $p$  and  $n$  are the hole and electron concentrations,  $\rho_p$  and  $\rho_n$  are the hole and electron distributions,  $N_D^+$  and  $N_A^-$  are the charged impurities of donor and acceptor,  $\epsilon_r$  and  $\epsilon_0$  are the permittivity of semiconductor and vacuum, respectively.

The continuity equations are expressed for electrons and holes as below,

$$\frac{dJ_n}{dx} = G(x) - R(x) \quad (2.33)$$

$$\frac{dJ_p}{dx} = G(x) - R(x) \quad (2.34)$$

where  $J_n$  and  $J_p$  are the current densities of electron and holes,  $R$  and  $G$  are the recombination and generation rate. And, the charge carrier transport in semiconductor is described by the following equations,

$$J_n = q\mu_n n(x)E(x) - qD_n \frac{dn(x)}{dx} \quad (2.35)$$

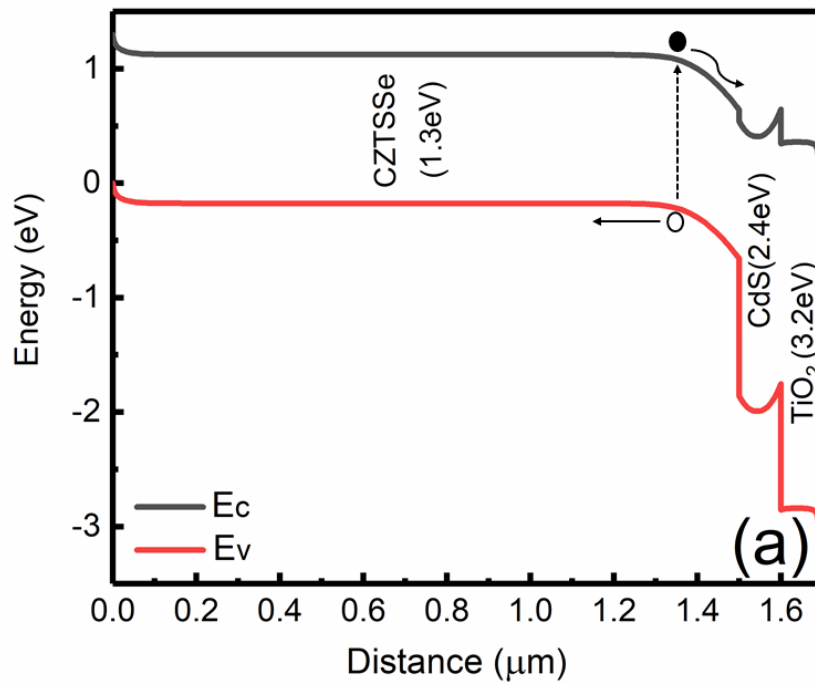
$$J_p = q\mu_p p(x)E(x) - qD_p \frac{dp(x)}{dx} \quad (2.36)$$

In this study, the photovoltaic parameters of glass/FTO/TiO<sub>2</sub>/CdS/CZTSSe/Au structure were calculated under illumination. Fluorine doped thin oxide (FTO) is used as front contact. Table 2.1 depicts the parameters of materials used in simulation.

Table 2.1. SCAPS input parameters [78], [79]

Material parameters	<i>CZTSSe</i>	<i>CdS</i>	<i>TiO<sub>2</sub></i>
Thickness ( $\mu m$ )	1.50	0.10	0.09
Band gap (eV)	1.3	2.4	3.2
Electron affinity (eV)	4.1	4.2	4.5
Relative permittivity $\epsilon_r$	13.6	10	55
CB density of states $N_c (cm^{-3})$	$2.2 \times 10^{18}$	$2.2 \times 10^{18}$	$1 \times 10^{19}$
VB density of states $N_v (cm^{-3})$	$1.8 \times 10^{19}$	$1.8 \times 10^{19}$	$1 \times 10^{16}$
Electron thermal velocity ( $cm \cdot s^{-1}$ )	$1.0 \times 10^7$	$1.0 \times 10^7$	$1.0 \times 10^7$
Hole thermal velocity ( $cm \cdot s^{-1}$ )	$1.0 \times 10^7$	$1.0 \times 10^7$	$1.0 \times 10^7$
Electron mobility $\mu_n (cm^2 \cdot V^{-1} \cdot s^{-1})$	$1.0 \times 10^2$	$1.0 \times 10^2$	$1.0 \times 10^2$
Hole mobility $\mu_p (cm^2 \cdot V^{-1} \cdot s^{-1})$	$2.5 \times 10^1$	$2.5 \times 10^1$	$5.0 \times 10^1$
Density of acceptors $N_A (cm^{-3})$	$2.0 \times 10^{16}$	-	$1.0 \times 10^1$
Density of donors $N_D (cm^{-3})$	-	$1.0 \times 10^{17}$	$1.0 \times 10^{18}$

The solar cell is at 300 K is illuminated from the FTO side. Current transport of heterojunctions strongly depends on the band alignment. The band diagram of CZTSSe solar cell in superstrate configuration was obtained by using SCAPS under the equilibrium condition. The cliff-like configuration at CZTSSe-CdS interface is observed as in Figure 2.12 (a). Photo-generated carriers at the interface are separated each other and they are accelerated by means of electric field. Holes flow to the absorber layer and collected by metal contact. On the other hand, electrons flow to the CdS. TiO<sub>2</sub> also exhibits the hole blocking behavior. In addition, simulated J-V characteristics and quantum efficiency (QE) results are given in Figure 2.12 (b). The photovoltaic parameters were obtained as  $V_{oc}=0.81V$ ,  $J_{sc}=32\text{ mA/cm}^2$ ,  $FF= 82\%$ ,  $\eta = 21\%$ . And, QE exhibited the high response between 500-900 nm (Figure 2.12 (c)).



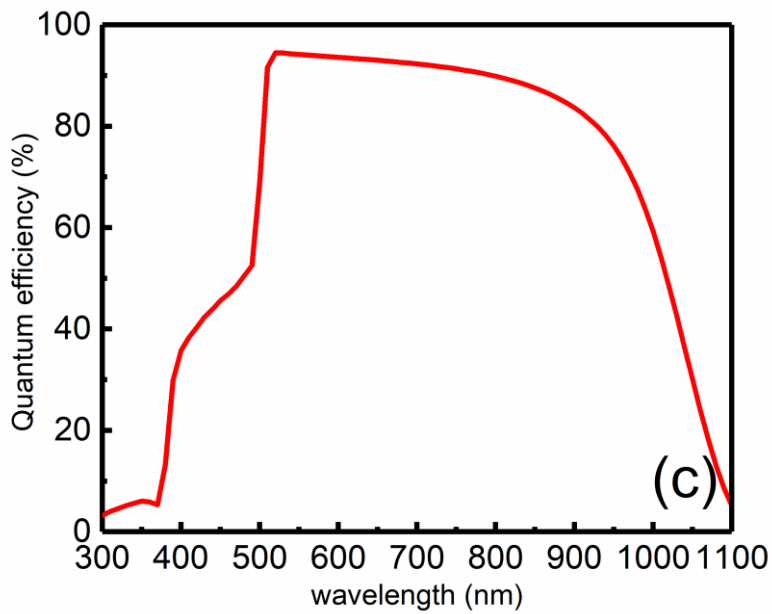
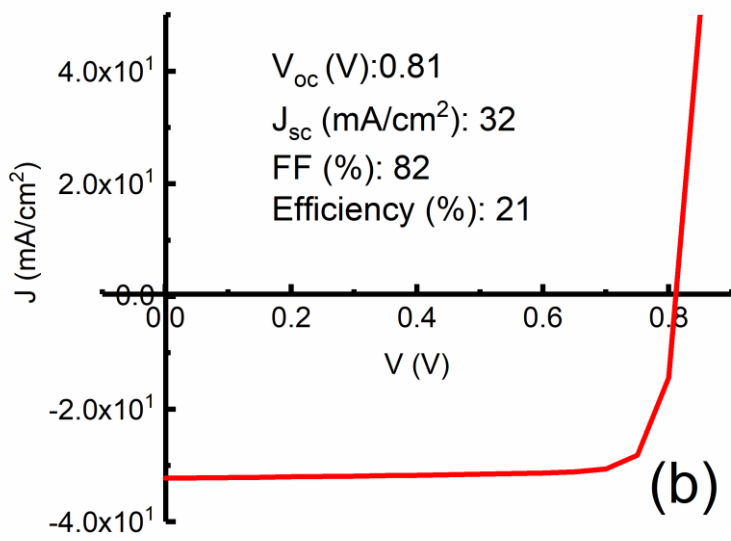


Figure 2.12. (a) Energy band diagram of CZTSSe solar cell, (b) J-V characteristics, (c) quantum efficiency vs wavelength plot of simulated CZTSSe superstrate solar cell under illumination

## CHAPTER 3

### METHODOLOGY

#### 3.1. Introduction

The aim of this chapter is to give short information about the deposition process of CZTSSe thin films and description of experimental setups which were used in this study. For this purpose, this chapter starts with the explanation of deposition systems and applied procedures for CZTSSe thin films. Then, the characterization techniques for CZTSSe thin films and CZTSSe thin film based devices are presented.

#### 3.2. Thin Film Growth Techniques

CZTSSe absorber layer is fabricated by using different techniques such as sputtering thermal evaporation, spray pyrolysis deposition and electrodeposition [4]. However, in the framework of this study, vacuum based approaches were used for deposition of thin films since physical vapor deposition (PVD) techniques are widely used in thin film deposition due to providing low contamination and uniformity control. In this study, thermal evaporation technique and magnetron sputtering technique are applied to deposit CZTSSe thin films.

##### 3.2.1. Thermal Evaporation Technique

Thermal evaporation relies on changing the phase of material from solid to vapor phase by heating source material via heating coil around the source tube in a vacuum chamber. This method is strongly depends on three parameters: material that vaporized thermally, applied voltage difference and vacuum pressure.

In this study, CZTSSe films were produced by using thermal evaporation technique in which sintered CZTSSe powder was used as the evaporation source. Deposition processes were carried out by using multi-source Vaksis Midas coating system as shown in Figure 3.1. This system consists of evaporation chamber, control unit, mechanic pump and turbo pump. In the chamber of this system, there are four fusion cells and a substrate holder which is placed at above the fusion cells at a fixed distance of about 30 cm. In addition, there is a rotation stage for substrate to obtain uniform film surface. The vacuum pressure of this system can reach to  $10^{-7}$  Torr. Thickness of the films can be controlled by Inficon XTM/2 during the deposition.

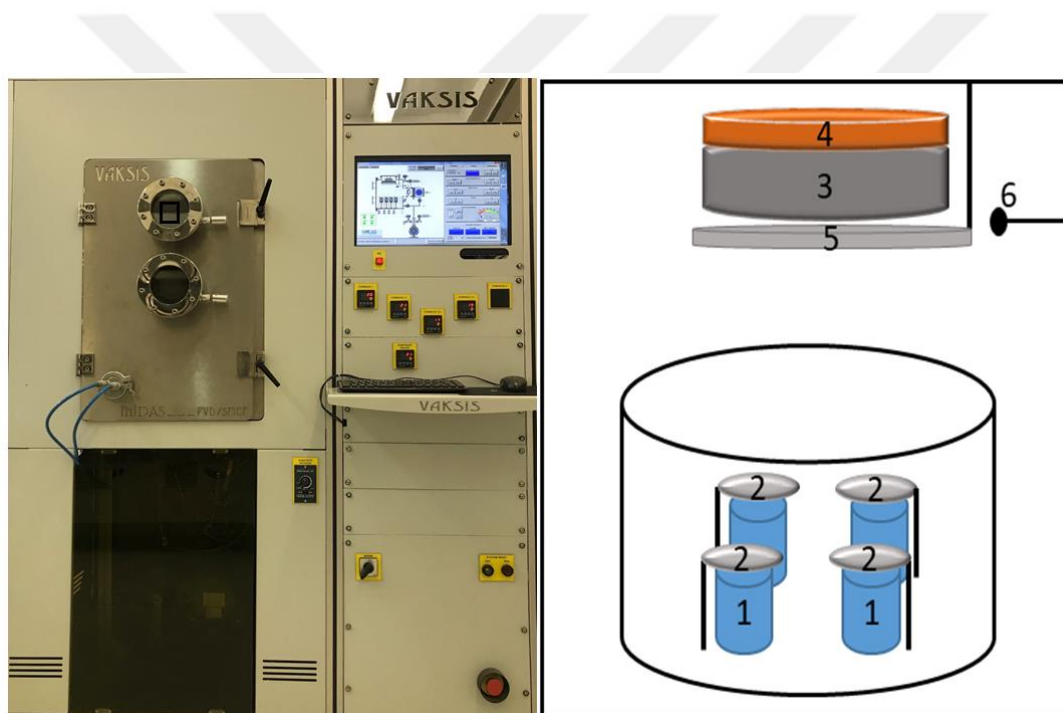


Figure 3.1. The multi-source thermal evaporation system and schematic view of the chamber of the system 1: fusion cells, 2: shutters of fusion cells, 3: substrate, 4: heater, 5: shutter of the substrate, 6: thickness monitor probe.

### 3.2.2. RF/DC Magnetron Sputtering Technique

Sputtering technique is based on the momentum transfer between the atom on the surface of source material (target) and inert gas ions. The target (or cathode) is bombarded by energetic ions generated in plasma and atoms of the target are ejected and accelerated to the substrate. In this process, secondary electrons are emitted from the surface of target, which provides the continuity of plasma. In sputtering systems, direct current (DC) or radio frequency (RF) plasmas are used for metals and insulators, respectively. However, there are major problems of this process such as low deposition rate, overheating the substrate. To overcome these limitations, magnetron sputtering have been developed. In magnetron sputtering, magnetically confined plasma is created close to the target when the gas atoms entering the vacuum chamber [80], [81].



Figure 3.2. An image showing Vaksis three magnetron sputtering system.

This constrain the motion of secondary electrons which are in the vicinity of target. Trapping the electrons enhances their probability of ionizing the gas atoms. The increase in ionization efficiency gives rise to the increase in ion bombardment of the surface of target. So, higher sputter rates are obtained in that way.

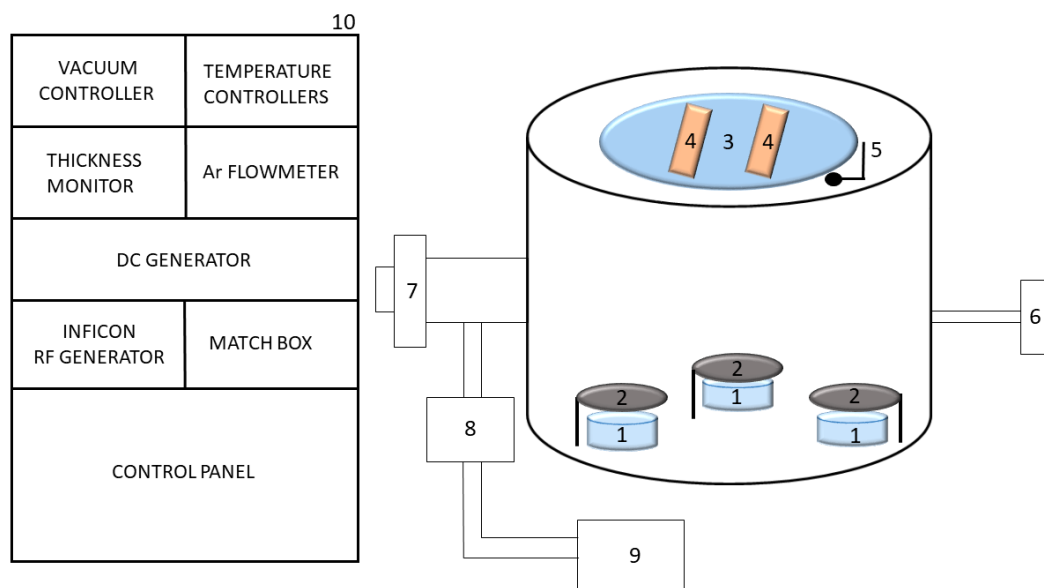


Figure 3.3. Schematic presentation of three magnetron system. 1: targets, 2: shutters, 3: substrate holder, 4: halogen lamp heater, 5: thickness monitor probe, 6: Ar flow controller, 7: vacuum valve, 8: turbo molecular pump, 9: rough pump, 10: control unit.

In this study, Vaksis three magnetron DC/RF sputtering system was utilized to deposit CZTSSe thin films (Figure 3.2). This deposition system has three magnetron heads that are cooled by water circulation. Chamber pressure is reached up to  $10^{-7}$  Torr. Ar flow is maintained to the vacuum chamber in order to create plasma. Substrate could be heated up to  $400^{\circ}\text{C}$  by means of halogen lamp heater. In addition, there is a rotation stage for substrate holder In Figure 3.3, the components of the system are given clearly.

### 3.3. Post-Annealing Process

Post-annealing process is widely utilized to improve the physical or chemical properties of deposited thin films. In this process, samples are put into the furnace and heated up to desired temperature for a certain time period under inert gas atmosphere. After that, samples are cooled down to the room temperature.

In this study, CZTSSe thin films were exposed to post-annealing process to make its materials properties better using Lindberg horizontal tube furnace, as shown in Figure 3.4. During the annealing, nitrogen ( $N_2$ ) gas flow was maintained into the furnace to eliminate contamination from ambient.



Figure 3.4. Horizontal tube furnace.

### 3.4. Thin Film Characterization Techniques

Having completed the deposition processes, CZTSSe thin films were analyzed by using various characterization techniques. In this subsections, a brief introduction of these techniques is given.

### 3.4.1. X-Ray Diffraction (XRD)

XRD is an efficient method to determine crystallographic and structural properties of the material properties. The diffraction pattern gives us to comprehensive knowledge about the material including orientation, phase composition and purity. X-ray wavelengths vary from 0.1 to 100 Å. However, the wavelengths used in XRD method are in the range of 0.5-2.5 Å since wavelengths should be the same order of magnitude with the shortest interatomic distances.

X ray diffraction is the elastic scattering of X-ray photons with atoms that are in a periodic structure. When hitting the monochromatic X-ray to atom, constructive or destructive types of interference may occur. The constructive interference of the incident beam in a specific orientation gives the x-ray diffraction patterns. Bragg's law describes the X-ray diffraction. As given in Figure 3.5 (a), the incident X-rays hit the planes with an angle  $\theta$  and the reflection angle  $\theta$ . To observe the diffraction peaks, Bragg condition is satisfied as follows [82];

$$n\lambda = 2d \sin \theta \quad (3.1)$$

where  $\lambda$  is the wavelength,  $d$  is the inter-planar distance of parallel planes,  $\theta$  is the Bragg angle and  $n$  is an integer which is called as the order of reflection.

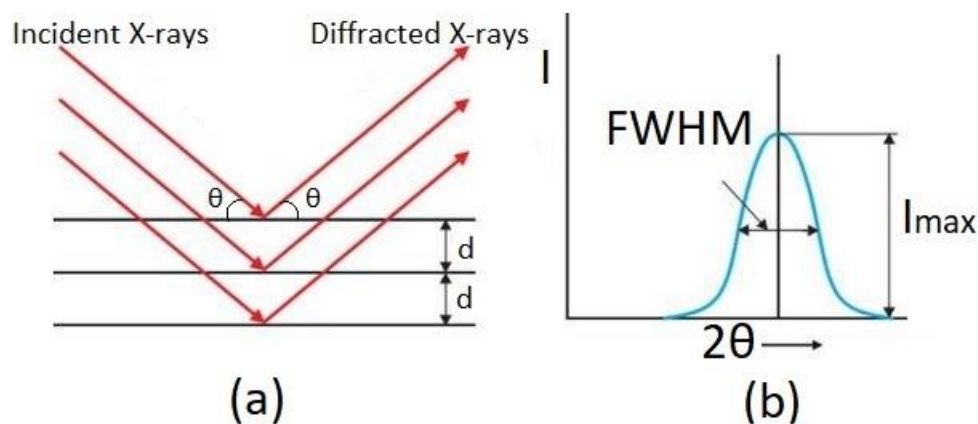


Figure 3.5. (a) X-rays diffraction from crystal planes, (b) observed diffraction peak.

For a perfect crystal structure with perfect instrumentation, the diffracted peak is a delta function. However, observed diffraction peak is broadened peak. The peak broadening may be due to imperfect crystallinity, strain, instrumental conditions etc. As indicated in Figure 3.5 (b), the width of a peak is measured by its full width at half maximum (FWHM) and it is used to calculate the average grain size of material with the help of Scherrer's equation [83];

$$GS = \frac{0.94\lambda}{\beta \cos \theta} \quad (3.2)$$

where GS,  $\beta$ ,  $\theta$ ,  $\lambda$  are the average grain size, FWHM in radians, Bragg angle and X-ray wavelength, respectively.



Figure 3.6. X-ray diffraction system.

In this work, Rigaku Miniflex XRD system equipped with  $\text{CuK}\alpha$  X-ray radiation source ( $\lambda = 1.504 \text{ \AA}$ ) was used to determine the structural properties of deposited thin films (Figure 3.6). The obtained XRD patterns were evaluated by using International Centre for Diffraction Data (ICDD) cards. With the identification of diffraction peak, the detailed knowledge about the thin films were obtained.

### 3.4.2. Raman Scattering Spectroscopy

Raman scattering which is based on Raman effect is the most powerful technique to obtain physical and chemical fingerprint of materials. On the contrary to XRD measurement, it is a local probe and it is utilized to detect inhomogeneity or secondary phases [84]. The Raman spectrum of a material is characteristic and thus, Raman spectroscopy is also utilized to identify the material. This technique is free from the charging effects[85].

When the monochromatic light interacts with the surface of a material, the scattered light is mostly found to be the same wavelengths with the incident light (Rayleigh scattering); a small number of photons (per million or less) interact with the material and undergo inelastic scattering. If the incident light interacts with the optical phonons, this is called as Raman scattering. On the other hand, if the incident light interacts with the acoustic phonons, this is called as Brillouin scattering.

Raman scattering consists of three physical process: photon absorption, absorption or emission of phonon and finally photon emission. In a Stokes process, emission of phonon occurs and the energy of emitted phonon is lower than the absorbed photon. On the other hand, in an anti-Stokes process, absorption of phonon occurs and its energy is higher than the absorbed photon (Figure 3.7) [86]–[88].

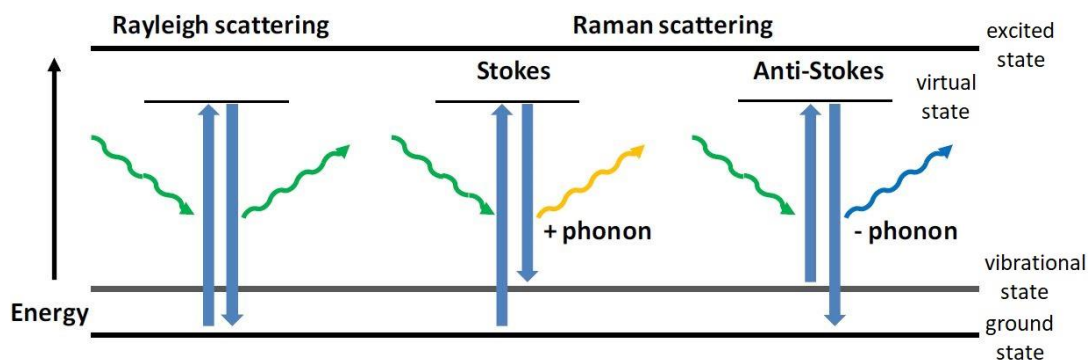


Figure 3.7. Schematic representation of Rayleigh and Raman Scattering [86].

In this characterization technique, laser is used as light source for excitation of material and scattered light from the material is detected by CCD detector.

In this thesis, Horiba-Jobin Yvon iHR550 imaging spectrometer with Peltier CCD camera and 532 nm green laser beam for laser source were used to analyze the quality of prepared CZTSSe thin films as shown in Figure 3.8.



Figure 3.8. Raman Spectroscopy System.

### 3.4.3. Scanning Electron Microscopy (SEM)

The scanning electron microscope (SEM) can be used to observe the surface details of organic or inorganic materials on a nanometer (nm) to micrometer ( $\mu\text{m}$ ) scale. The observation of grain size, shape, dendrites, voids and cracks is the typical applications [89].

In the SEM, the surface area is observed by using focused electron beam. When interacting the electron beam with the material; secondary electrons, back-scattered electrons, characteristic x-rays are generated. These signals are used to analyze some properties of materials including surface topography, composition contrast, and elemental analysis. The penetration depth of incident electrons is related to accelerating voltage. Accelerating voltage in between 20-30 keV can provide the image resolution up to 1nm or better. The SEM consists of three main parts: electron

column, specimen chamber and computer control system. There is an electron gun at the top part of the electron column generating an electron beam. Electromagnetic lenses are also located in the column to focus the beam. To provide the generation of electron beam and increasing the mean free path of electrons; the electron column and the specimen chamber are kept under the high vacuum [89].

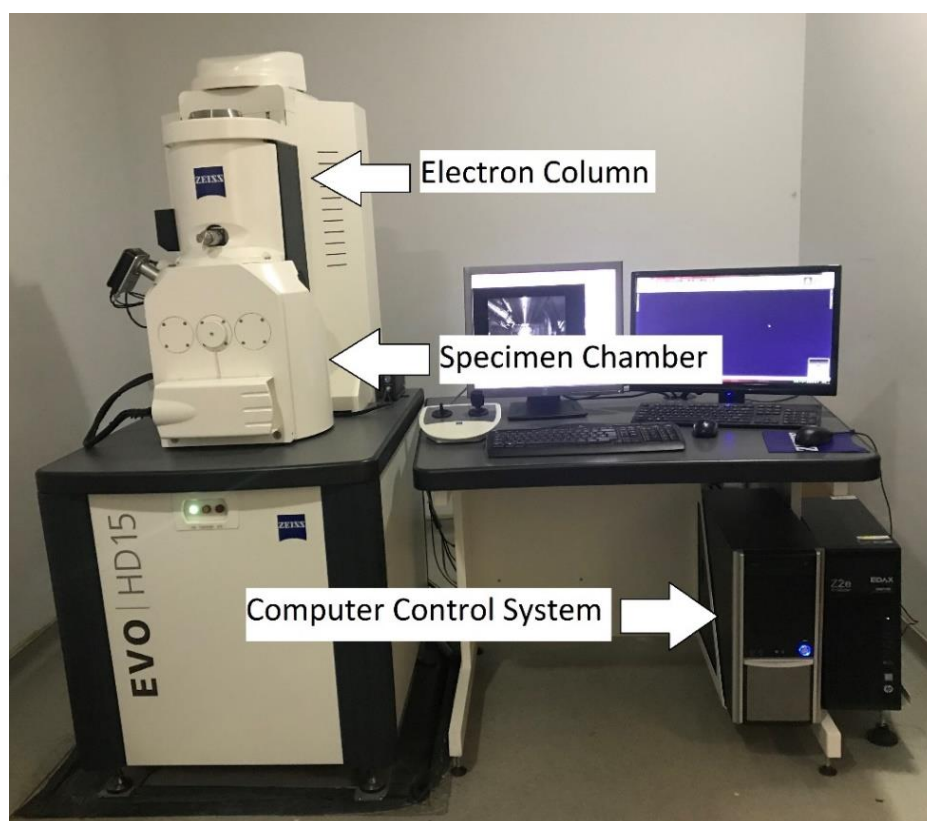


Figure 3.9. An image showing the main parts of the SEM system.

In this work, the examination of the film surface was carried out by using Quanta 400F field emission scanning electron microscope (FE-SEM) and Zeiss EVO HD scanning electron microscope (SEM) as shown in Figure 3.9.

### 3.4.4. Energy Dispersive X-ray Spectroscopy (EDS)

Energy dispersive X-ray spectroscopy (EDS) is a way to obtain chemical information of materials examining in the SEM. When the interaction of electron beam and material occurs, characteristic X-rays are generated. And these X-ray signals are collected and analyzed with respect to its energy and intensity by means of EDS detector. The output of EDS detector is given by EDS spectrum of material. For EDS measurement, in this thesis, Ametek EDAX energy dispersive X-ray spectroscope was used.

### 3.4.5. Atomic Force Microscopy (AFM)

Atomic force microscopy (AFM) is a useful method to obtain the shape of a material surface in three dimensional (3D) detail. All materials can be imaged by AFM including biological structures, polymers and ceramics regardless of conductivity or opaqueness.

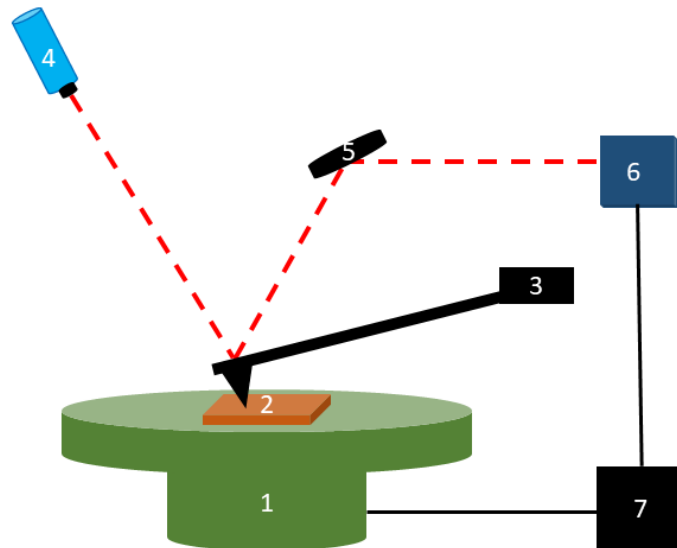


Figure 3.10. The schematic diagram of AFM. 1: piezo-electric scanner, 2: sample, 3: chip with cantilever, 4: laser diode, 5: mirror, 6: position-sensitive photodetector, 7: electronics (computer system).

This technique is based on the forces between the surface of the sample and tip on a cantilever as shown in Figure 3.10.

In AFM measurement, a laser beam is reflected from the back surface of the cantilever and detected by position-sensitive detector. The force deflect the cantilever and this changes the reflection of laser beam. All variations of reflected laser beam are the measure of applied force [90].

In this thesis, Veeco diMultiMode V was employed for AFM measurements (Figure 3.11). The obtained data from AFM measurement was analyzed by using Gywidion 2.44.



Figure 3.11. AFM setup used in this study.

#### **3.4.6. Transmission and Reflection Measurements**

Transmission and reflection measurements are crucial characterization tools to determine the optical band gap and optical constants of thin films. In an ordinary transmission measurement, the intensity of transmitted light from the sample is measured by using a spectrophotometer. A spectrophotometer enables us to measure the both transmission and reflection. It consists of light source, sample holder, a

monochromator and detector to catch the transmitted and reflected light. Transmitted or reflected light is measured as a function of wavelength. In this study, Perkin Elmer Lambda 45 UV/Vis/NIR spectrometer in the wavelength of 300-1100nm and Bentham PVE 300 measurement system were used for optical measurements. They are given in Figure 3.12.

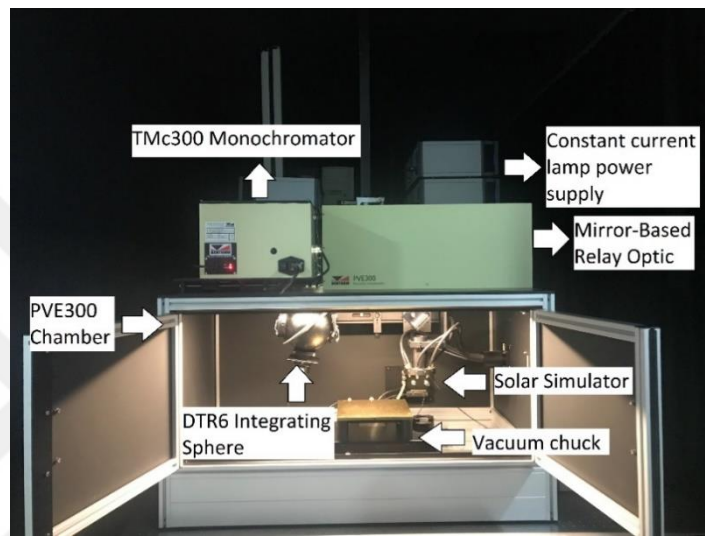


Figure 3.12. Bentham PVE 300 system.

#### 3.4.7. Resistivity Measurement

There are several type of sample geometry used for electrical characterization of thin films such as van der Pauw and Hall bar sample geometries. In this thesis, Van der Pauw geometry was used for electrical characterization of thin films due to the requirement of only four ohmic contact without measuring the distance between the contacts [91]. The geometry used in this work is shown in Figure 3.13.

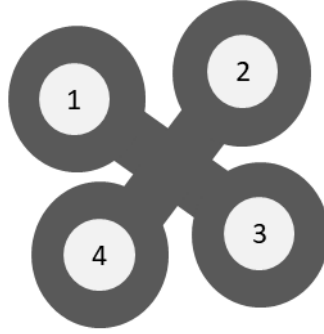


Figure 3.13. Schematic representation of van der Pauw geometry that was prepared for electrical characterization.

The definition of resistivity of a material is the ratio of potential gradient along the applied current which flows in the material to the current density. The unit of resistivity is Ohm.meter ( $\Omega.m$ ) in SI units. The resistivity measurement was performed by using closed cycle cryostat under vacuum in the temperature range of 100-340 K with 10 K increments. The applied current was maintained by Keithley 220 current source. A LakeShore 331 temperature controller was utilized to adjust the temperature of sample that inside the cryostat. LabVIEW software programming language was also used in all measurements. The schematic representation of experimental setup used in this study is given in Figure 3.14.

A typical resistivity measurement relies on applying the constant current through the contact pair and measuring the voltage dropped across other contacts. For example, the constant current  $I_{12}$  (I) is applied through the contacts 1 and 2, the potential difference between the contacts 3 and 4 is measured and recorded. This is defined as  $V_{12,34}$ . Other potential  $V_{23,41}$ ,  $V_{34,12}$ , and  $V_{41,23}$  are measured in a same way. Subsequently, the resistance of  $R_a = \frac{V_{12,34}}{I}$ ,  $R_b = \frac{V_{23,41}}{I}$ ,  $R_c = \frac{V_{34,12}}{I}$ ,  $R_d = \frac{V_{41,23}}{I}$  are calculated. According to theorem stated by Van der Pauw, when obtaining the values of  $R_a$ ,  $R_b$ ,  $R_c$  and  $R_d$ ; the resistivity of sample is defined as the following expression [91],

$$\rho = \frac{\pi t}{\ln(2)} \frac{(R_1 + R_2)}{2} f \left( \frac{R_1}{R_2} \right) \quad (3.3)$$

Where  $t$  is the thickness of film,  $R_1 = R_a + R_b$ ,  $R_2 = R_c + R_d$  and  $f$  is a geometrical correction factor which is taken 1 for the sample having symmetrical contact geometry.

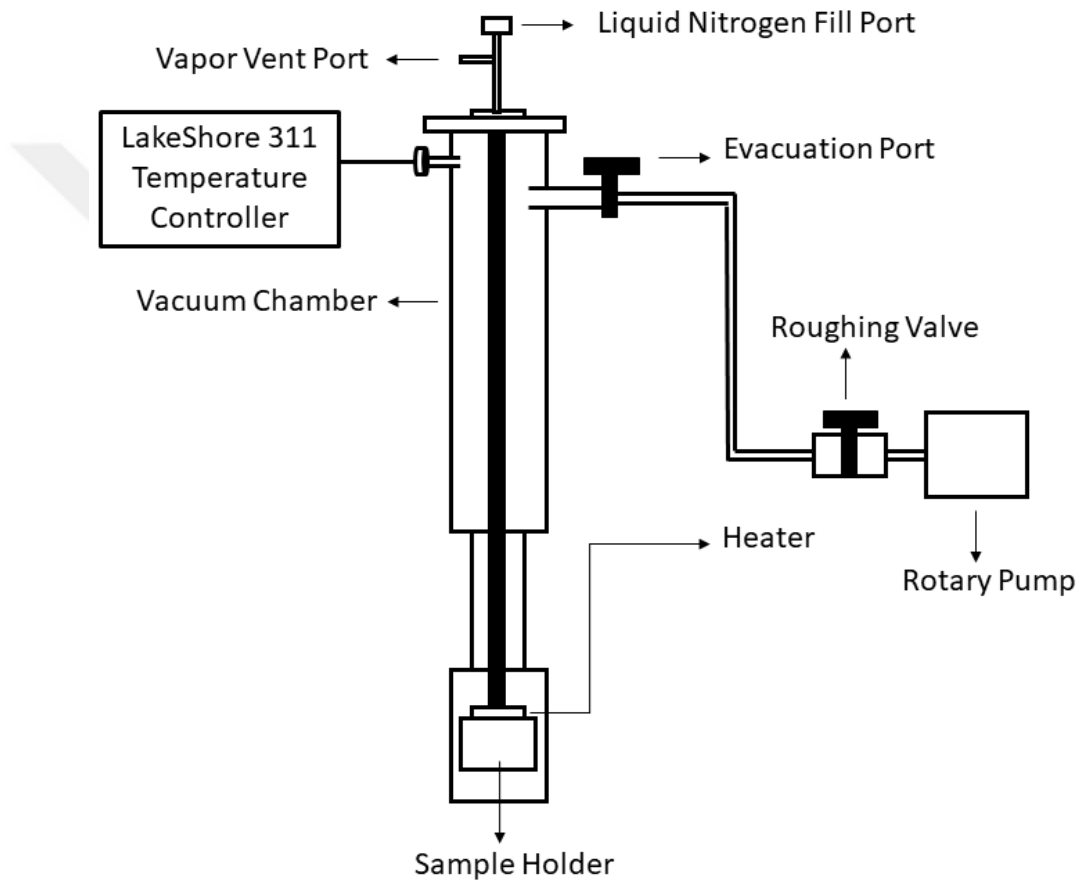


Figure 3.14. The illustration of the cryostat system.

### 3.4.8. Photoconductivity Measurement

The explanation of photoconductivity is the change in measured conductivity of a material under illumination. When absorbing of the photon having energy greater than

the band gap of a material, the generation of free carriers occur. This increases the conductivity of semiconductors. However, the recombination process limits the increase in conductivity. As a result of the balance between generation and recombination process, steady state photoconductivity condition occurs. The probability of recombination of electron and hole is proportional to product of their densities when taking into consideration of the assumption that the electron density of semiconductor in equilibrium is always larger than the generated carrier densities [92]. This expression can be written as,

$$-\frac{dn}{dt} = Anp = An_o p \quad (3.4)$$

where  $n_o$  is the density of electrons in equilibrium and A is the constant. Using the Eqn 3.4, the equation of excess carrier density is found as,

$$n(t) = n(0)\exp\left(-\frac{t}{\tau}\right) \quad (3.5)$$

where  $\tau$  is the recombination lifetime and defined as,

$$\tau = (An_o)^{-1} \quad (3.6)$$

In steady state condition, since the generation rate is equal to recombination rate, steady state photoconductivity is calculated by the following expression,

$$\sigma_{ph} = q\Phi_p\alpha\mu\tau \quad (3.6)$$

where  $\alpha$  is the absorption coefficient of material and  $\Phi_p$  is the incident photon flux. In addition, generation rate of free carriers,  $G$ , is defined as  $G \approx \Phi_p\alpha$ .

Photoconductivity measurement is beneficial to obtain the information about the trap levels in the band gap considerably. In this study, a Janis cryostat having liquid nitrogen cooling system was utilized to measure the photoconductivity of CZTSSe thin film. Measurements were carried out in the temperature range of 100-340 K.

Sample was illuminated by using 12 Watt halogen lamp where the lamp is placed above the sample. Different illumination intensities (20-115 mW/cm<sup>2</sup>) were used for this measurement with the help of Keithley 220 programmable current source. Also, Keithley 2400 sourcemeter was used for applying the bias voltage and measuring current between the contact pair. The setup in which all electrical characterization measurements of thin films including photoconductivity were done is given in Figure is 3.15.



Figure 3.15. Experimental setup of photoconductivity and Hall effect system.

### 3.4.9. Hall Effect Measurement

Hall Measurement is carried out to determine the electrical parameters of a material such as carrier concentration, semiconductor behavior, and mobility. Hall measurement was done by using the sample having Van der Pauw geometry as given in Figure 3.13. In this measurement, firstly, when applying a constant current between the contact pair 2 and 4 without the magnetic field, the potential drop between the contact 1 and 3 is measured. Thus,  $R_x = (V_3 - V_1)/I$  is calculated. Subsequently, a

constant current is applied to the same pair with the magnetic field. Then, potential difference of the contacts 1 and 3 is measured again and  $R'_x = (V_3 - V_1)/I$  is found. As a next step, constant current is applied between the other contact pair (1-3) in the case of no magnetic field. Then, voltage difference between the contact 2 and 4 is measured and  $R_y = (V_2 - V_4)/I$  is calculated. Finally, the same process is carried out under the magnetic field and  $R'_y = (V_2 - V_4)/I$  is found. At the end of all measurement,  $\Delta R_x = (R_x - R'_x)$  and  $\Delta R_y = (R_y - R'_y)$  are calculated to find the Hall coefficient ( $R_H$ ) and it is defined by the following equation [91],

$$R_H = \frac{t}{B} \frac{(\Delta R_x + \Delta R_y)}{2} f \quad (3.7)$$

where  $t$  is the thickness of sample,  $B$  is the applied magnetic field and  $f$  is the correction factor which is assumed as 1 due to symmetrical contact configuration. In addition, the conductivity type of material is determined by the sign of  $R_H$ . The carrier concentration of material is calculated by using the relation as below,

$$n \text{ ( or } p) = \frac{r}{qR_H} \quad (3.8)$$

where  $r$  is the Hall factor,  $n$  ( or  $p$ ) stands for the concentration of electron (or hole). Hall mobility can be also found as,

$$\mu = \sigma R_H \quad (3.9)$$

In this study, Nanomagnetic Hall effect system was employed for determining electrical properties of CZTSSe thin films. Measurements were carried out at room temperature and applying a magnetic field strength of 0.9 T produced by Walker Magnion Model FFD-4D electromagnet. The system used for Hall-effect is shown in Figure 3.15.

### 3.5. Device Characterization Techniques

#### 3.5.1. Current-Voltage Measurements

To obtain rectifying behavior and determine the current conduction mechanism of diode structure, temperature dependent current voltage (I-V) measurements can be performed. In this study, current conduction mechanism of CZTTe/Si structure was investigated in details. For this, Keithley 2401 sourcemeter controlled by the LabVIEW program was employed during the measurements. Cooling and heating processes were maintained by CTI-Cryogenics Model 22 refrigerator system with helium compressor and temperature of sample was controlled by Lakeshore DRC-91C controller. The system is given in Figure 3.16.

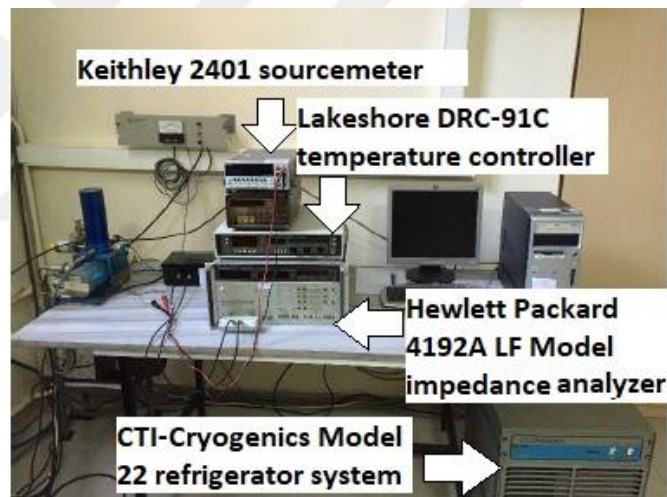


Figure 3.16. The experimental setup of temperature dependent current-voltage and frequency dependent capacitance-voltage measurement system.

#### 3.5.2. Capacitance-Voltage Measurements

Frequency dependent capacitance-voltage (C-V) measurements are employed for analysis of the interface states or deep trap levels at the junction of diode structure. In

addition, built in potential ( $V_{bi}$ ) of a junction can be found by means of C-V measurement.

In this study, frequency dependent C-V measurements were completed at room temperature by using Hewlett Packard 4192A LF model impedance analyzer (Figure 3.16). . The frequency limit of used the impedance analyzer is in the range of 5Hz-13MHz. All measurements was controlled by LabVIEW program. Applying voltage and frequency values were determined by depending on the properties of structure. The experimental setup is given in Figure 3.16.

### 3.5.3. Solar Cell Measurements

Electrical characteristic of solar cell are determined by using I-V measurement under AM 1.5G illumination condition. This measurement provide us to find the main solar cell parameters such as open circuit voltage ( $V_{oc}$ ), short circuit current ( $J_{sc}$ ), efficiency ( $\eta$ ), fill factor (FF), series resistance ( $R_s$ ) and shunt resistance ( $R_{sh}$ ). In this thesis, solar cell measurements were conducted by using Newport Solar Simulator and the schematic representation of used experimental setup is given in Figure 3.17.

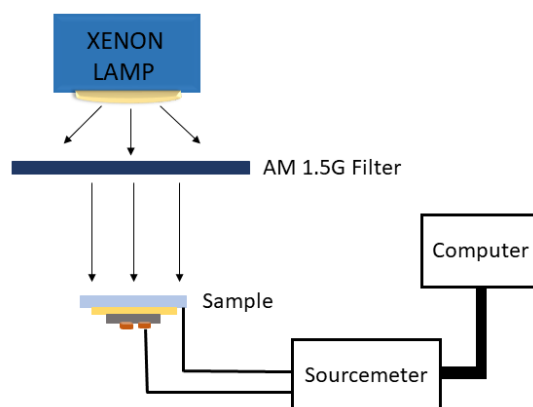


Figure 3.17. Schematic presentation of solar simulator.

## CHAPTER 4

### DEPOSITION AND CHARACTERIZATION OF THERMALLY EVAPORATED CZTSSE THIN FILMS AND ANALYSIS OF CURRENT CONDUCTION MECHANISM OF CZTSSE/SI STRUCTURE

#### 4.1. Introduction

The main aims of this study are to produce CZTSSe thin films using a cost-effective way that does not require any additional post-deposition steps such as sulphurization or selenization process and to investigate the current conduction mechanism of CZTSSe/Si structure. Although there are few studies on the device performance of CZTSSe/Si structure, to the best of our knowledge this work is the first attempt to investigate current conduction mechanism of CZTSSe/Si structure. For this purpose, CZTSSe thin films were grown on SLG and n-type Si wafer substrates by thermal evaporation technique as single-step production. In this process, sintered CZTSSe powder was used as the evaporation source. Then, structural, morphological, optical and electrical properties of films were investigated in details. On the other hand, using the optimized CZTSSe layer, CZTSSe/Si diode structure was fabricated in order to obtain diode parameters for possible promising applications in various technologies. The electrical properties and main diode parameters of this heterostructure were also studied using temperature dependent current-voltage (I-V), frequency dependent capacitance-voltage (C-V) and conductance-voltage (G/w-V) measurements. The temperature dependence of forward bias I-V analysis which is based on thermionic emission (TE) theory revealed that there is an anomaly which indicates the barrier height inhomogeneity at the interface. For this reason, the conduction mechanism was modified by considering the assumption of thermionic emission with a Gaussian distribution of barrier heights. Both the mean barrier height ( $\bar{\Phi}_{B0}$ ) and standard deviation ( $\sigma_0$ ) at zero bias were found as 1.27 eV and 0.18 eV, respectively. In

addition, using modified Richardson plot, Richardson constant was recalculated as  $120.46 \text{ A.cm}^{-2}\text{K}^{-2}$ . Using the results of frequency dependent C-V and G/w-V measurements at room temperature, density of interface states as a function of voltage and frequency was obtained by means of high-low frequency capacitance values ( $C_{\text{HF}}$ - $C_{\text{LF}}$ ) and Hill-Coleman methods, respectively.

## 4.2. Experimental Procedure

The experimental part of this study consists of three main parts: production of the crystalline  $\text{Cu}_2\text{ZnSn(S,Se)}_4$  powder, CZTSSe thin film evaporation process, and fabrication of In/CZTSSe/Si/Ag heterostructure. To obtain  $\text{Cu}_2\text{ZnSn(S,Se)}_4$  crystalline powder, firstly, the sintering process was performed. For this, a stoichiometric mixture of constituent elements having high purity (99.99%) of Cu, Zn, Sn, S, and Se was put into the quartz ampoule which was chemically cleaned. Then, quartz ampoule with a mixture of elements was evacuated in which vacuum level was around of  $10^{-5}$  Torr. Subsequently, ampoule was sealed and it was loaded into the vertical furnace as seen in Figure 4.1(a). Sealed ampoule was heated from room temperature to  $1150^\circ\text{C}$  with the rate of  $100^\circ\text{C/h}$  and it was kept at  $1150^\circ\text{C}$  for 48 hours. Then, quartz ampoule was cooled down to the room temperature with the same rate. After that, it was placed into the Crystalox MSD-4000 model three zone vertical Bridgman-Stockbarger system to get a crystalline form of  $\text{Cu}_2\text{ZnSn(S,Se)}_4$  compound (Figure 4.1 (b)). Temperatures of the top, middle and bottom zones of this system were adjusted as  $1050^\circ\text{C}$ ,  $850^\circ\text{C}$  and  $750^\circ\text{C}$ , respectively. The process carried out in 72 hours with the translation rate  $4.00 \text{ mm/h}$ . Then, the ingot was divided into pieces and elemental composition of pieces was determined by means of EDS measurements. And subsequently, the piece having stoichiometric composition was crunched in a powder form which was used as the evaporation source. CZTSSe thin films were grown on soda-lime glass (SLG) substrates and n-type Si (100) wafers with the resistivity value of  $1\text{-}10 \text{ }\Omega\text{.cm}$  by thermal evaporation. The substrate temperature was

kept at room temperature and the base pressure of the evaporation system was around  $10^{-5}$  Torr during the deposition. Before the deposition, the glass substrates were cleaned ultrasonically in acetone, isopropanol and  $\text{H}_2\text{O}_2:\text{H}_2\text{O}$  (1:3) for 10-minutes in each step. On the other hand, in order to remove natural oxide layers on the surfaces of the Si wafers, the etching treatment by  $\text{HF}:\text{H}_2\text{O}$  (1:10) solution was applied. In addition, the back surfaces of wafers were coated silver (Ag) as a metal contact by thermal evaporation and annealed at  $350^\circ\text{C}$  under nitrogen ( $\text{N}_2$ ) flow to provide the ohmic behavior of the contacts. Following the deposition of the CZTSSe thin film, all samples were annealed at  $350^\circ\text{C}$  under  $\text{N}_2$  atmosphere to improve the CZTSSe structure. Subsequently, the front indium (In) ohmic contact was deposited to the film surface by using copper dot masks  $500\ \mu\text{m}$  in diameter to complete In/CZTSSe/Si/Ag sandwich structure.



Figure 4.1. (a) Vertical furnace, (b) Bridgman-Stockbarger system.

The morphological and compositional properties of the deposited films were examined by Quanta 400 FEG model scanning electron microscope (SEM) equipped with energy dispersive X-ray spectroscopy analysis (EDS) system. Atomic force microscopy (AFM) technique by using a Veeco Multimode V AFM system, was performed to investigate the surface morphology of the thin films. The thicknesses of the as-grown and annealed films on SLG substrate were determined by a Dektak 6M profilometer. X-ray diffraction (XRD) measurements with Rigaku Miniflex XRD system equipped with CuK $\alpha$  radiation source having wavelength 1.54 Å, were carried out. Raman scattering measurements were performed by using a Horiba-Jobin Yvon iHR550 imaging spectrometer with a three-grating monochromator and a laser with the wavelength of 532 nm used as an excitation source. Spectral transmission and reflection measurements were carried out with Perkin-Elmer LAMBDA 45 UV/VIS/NIR spectrophotometer in the wavelength region of 300-1000 nm. Also, Hall-effect measurement was also measured to determine the electrical properties of the films by using Nanomagnetic Hall Effect system at a magnetic field strength of 0.9 T. Temperature dependent conductivity measurements under illumination and in dark were also applied in the range of 100-340K by means of Janis liquid nitrogen cryostat and Lake-Shore 331 temperature controller. To investigate the device parameters of In/CZTSSe/Si structure, temperature dependent current-voltage (I-V) measurements were done in dark using the computer-controlled measurement setup with a Keithley 2401sourcemeater, Model 22 CTI Cryogenics closed-cycle helium cryostat and LakeShore DRC-91C temperature controller. In addition, HP 4192A LF Impedance Analyzer was used for the measurements of capacitance-voltage (C-V) and conductance-voltage (G-V) of the devices. A study of the photo-electrical measurements was carried out to determine the photovoltaic behaviors by using Newport solar simulator and basic parameters were extracted by performing forward biased I-V curve analysis under dark and with illumination of 100 mW/cm<sup>2</sup>.

### 4.3. Results and Discussions

#### 4.3.1. Structural Properties of CZTSSe Thin Film

The EDS result of the deposited film showed that the atomic weight percentage of Cu, Zn, Sn, S, Se is 8, 10, 24, 24, 34 %, respectively, which indicates that the film is Cu-poor, Sn-rich. The elemental composition of the deposited film was obtained with different stoichiometry, although stoichiometric CZTSSe powder was used as a source during the thermal evaporation process. This can be explained by the differences in vapor pressures of constituent elements, which plays an important role in thermal evaporation process to enable the stoichiometric film composition. That is, CZTSSe pentanary alloy may be decomposed into constituent element or binary/ternary compound during the thermal evaporation process.

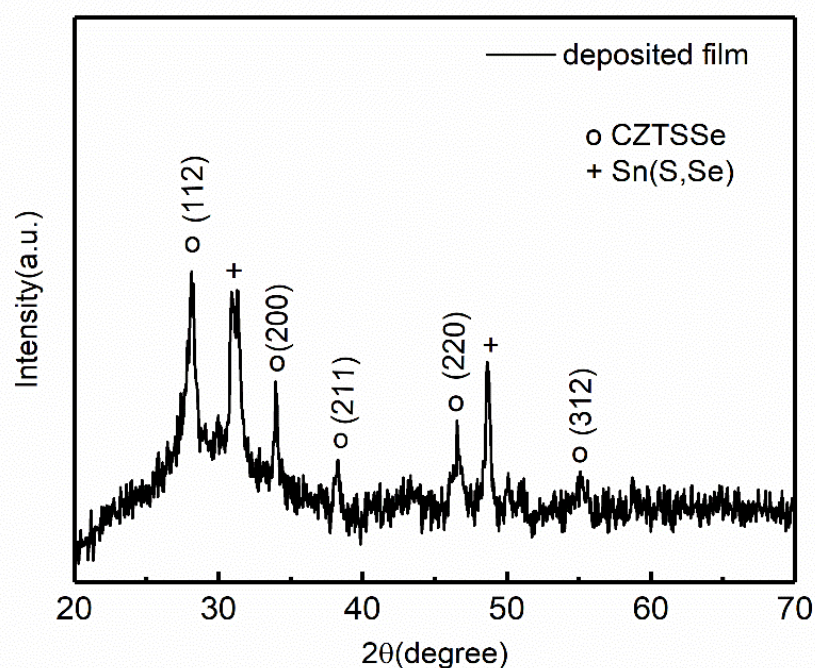


Figure 4.2. The XRD pattern of deposited film.

Figure 4.2 shows the XRD pattern of the film in the range of  $2\theta = 10^\circ$  to  $70^\circ$ . In literature, the main peak which is the reflection from the (112) plane is known to be at  $27^\circ$  in XRD spectrum of pure CZTSe phase, while the position of (112) plane of pure CZTS phase is observed at  $28.5^\circ$ . On the other hand, in CZTSSe phase, the peak position of (112) plane is expected to shift towards the higher diffraction angle depending on the ratio of S/(S+Se) in the XRD spectrum [93], [94]. As observed from Figure 4.2, the (112) plane is detected at  $2\theta = 28.1^\circ$ , which is in good agreement with the kesterite CZTSSe phase (ICDD data #00-052-0868 CZTSe and ICDD data#00-026-0575 CZTS). In addition, secondary phases which are labeled as Sn(S,Se) are also observed in XRD spectrum of the film (ICDD data#00-048-1224 SnSe and ICDD data#00-039-0354 SnS). In order to confirm the presence of CZTSSe structure and identify the secondary phases in the film composition, Raman scattering measurement was performed by using 532 nm excitation wavelength.

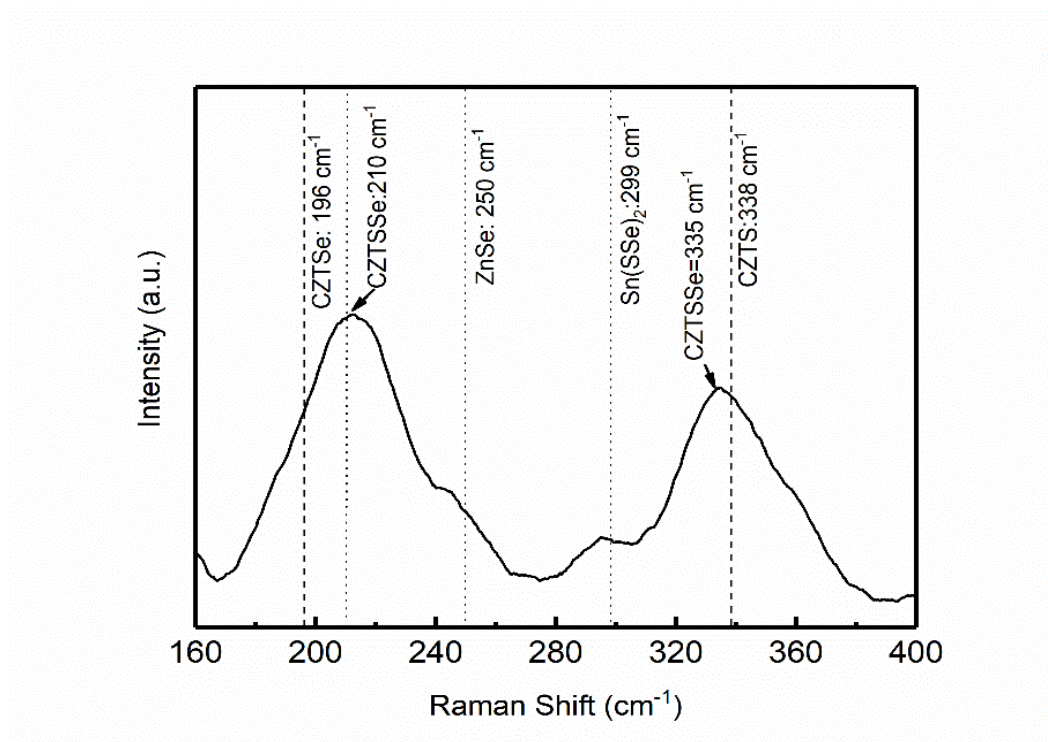


Figure 4.3. Raman spectrum of the deposited film.

Figure 4.3 demonstrates the Raman spectrum of deposited thin film. The  $A_1$  Raman mode frequency of the pure CZTSe structure is known to be at  $196\text{ cm}^{-1}$ , which is attributed to vibration of selenium atoms in the lattice. On the other hand, the  $A_1$  Raman mode frequency of pure CZTS structure is observed at  $338\text{ cm}^{-1}$ , which corresponding to the vibration of sulfur atoms. However, Raman spectrum of CZTSSe compound has two-mode behavior [95].

It is expected that there is a shift of  $A_1$  Raman modes of CZTSe and CZTS depending on the sulfur concentration in CZTSSe. As indicated in Figure 4.3, the Raman spectrum of the deposited film showed two-mode behavior and peaks were detected at  $210\text{ cm}^{-1}$  and  $335\text{ cm}^{-1}$ , which is in agreement with the reported results.

The broaden Raman peak indicates that there is a structural disorder due to the random distribution of S and Se atoms in the lattice, which gives rise to fluctuation in the masses and the force constants with neighbors [95]. In addition, to identify the secondary phases, Raman spectrum was fitted by using the mixed of Lorentzian and Gaussian function and two peaks at  $250\text{ cm}^{-1}$  and  $299\text{ cm}^{-1}$  were determined attributing to ZnSe and  $\text{Sn}(\text{S},\text{Se})_2$ , respectively [96], [97] .

In Figure 4.4, the cross-sectional and top-view SEM micrographs of CZTSSe/Si structure are presented. As observed in Figure 4.4, the thickness of the CZTSSe film is about 900 nm, which is consistent with the result of Dektak thickness profilometer. It is seen that the surface of the film had compact and densely packed morphology without any void on the surface.

To understand the surface morphology of deposited films better, AFM measurements were carried out as given in Figure 4.5. The surface was observed to be rough and the average surface roughness of CZTSSe film was found to be around 44 nm. On the other hand, in 2D AFM images, grain boundaries were observed clearly, which is in good agreement with the results of SEM images.

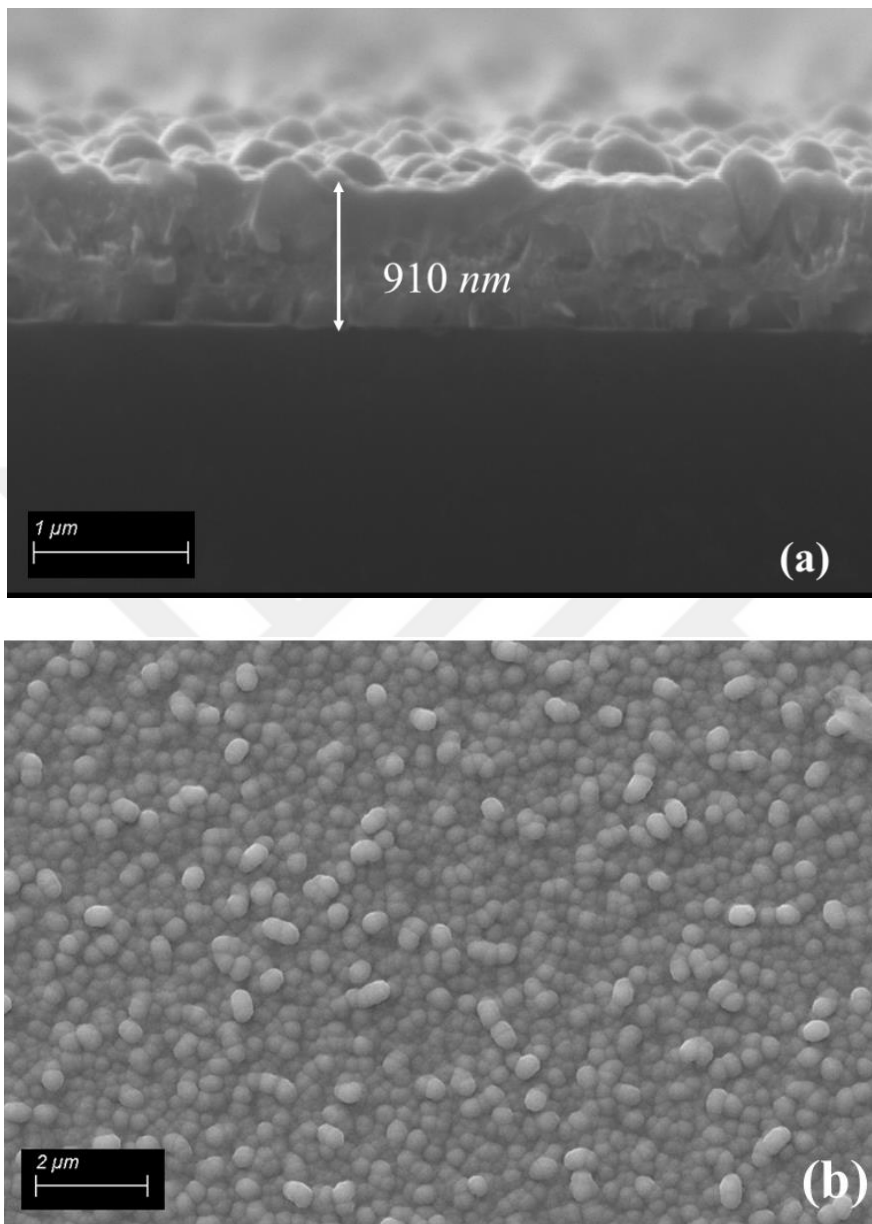
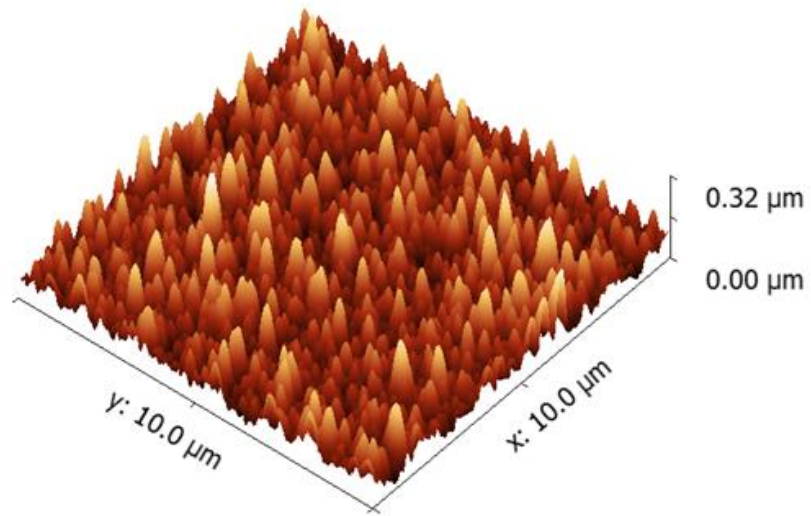
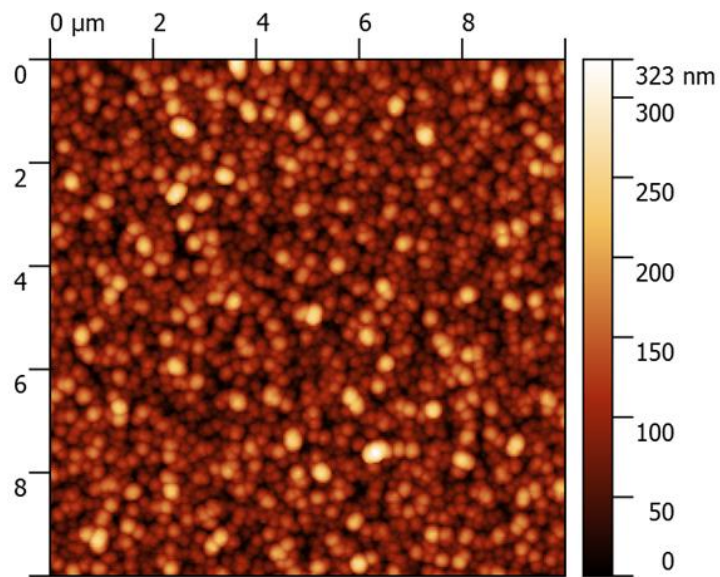


Figure 4.4. (a) Cross-sectional, (b) top-view SEM images of CZTSSe/Si structure.



(a)



(b)

Figure 4.5. (a) 3D, (b) 2D  $10\mu\text{m} \times 10\mu\text{m}$  AFM images of deposited film.

### 4.3.2. Optical Properties of CZTSSe Thin Film

After detailed structural analyses, the transmittance (T) and reflectance (R) measurements were conducted in the range of 300-1000 nm. Figure 4.6 demonstrates the transmittance and absorbance spectrum of CZTSSe films on SLG.

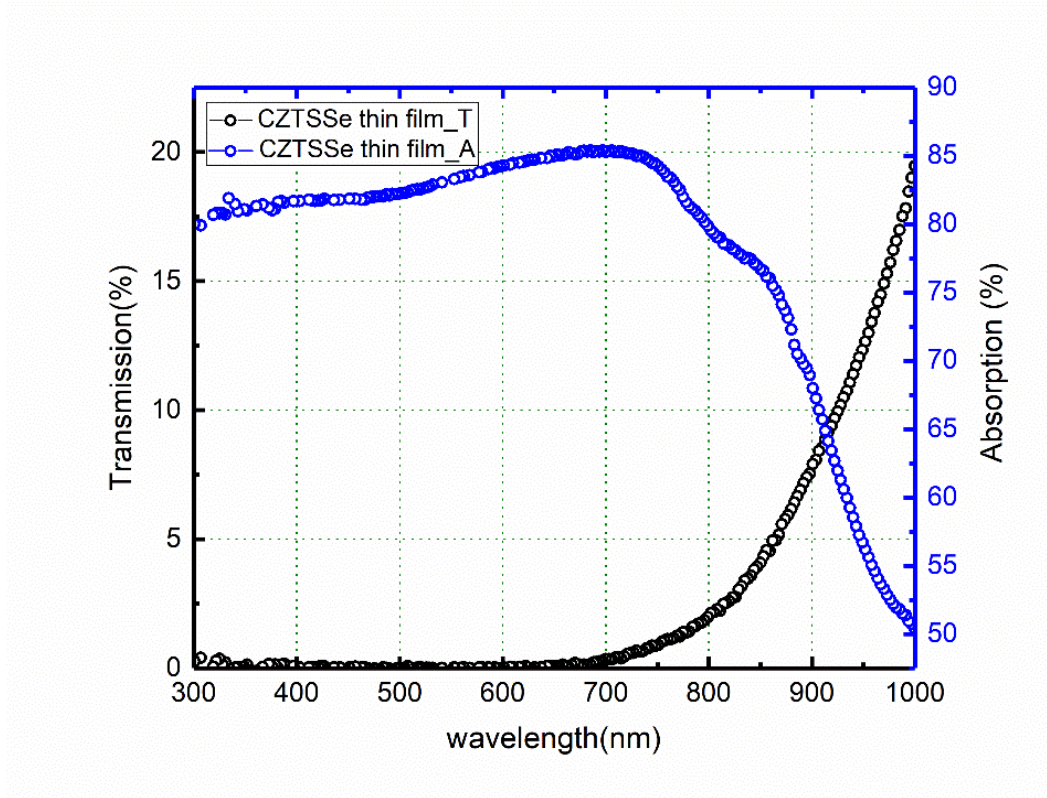


Figure 4.6. Transmission and absorption spectrum of CZTSSe thin film.

As seen in Figure 4.6, the deposited film has a high absorbance in the visible region. In addition, the spectral dependence of the absorption coefficient of CZTSSe film was calculated using the following expression

$$T = (1 - R)^2 e^{-\alpha t} \quad (4.1)$$

where  $\alpha$  is the absorption coefficient and  $t$  is the thickness of the sample. The absorption coefficient of the CZTSSe thin film was found to be larger than  $10^4 \text{ cm}^{-1}$  as indicated in Figure 4.7. It is in good agreement with the reported researches [4], [98]. Then, to determine the direct band gap energy of the deposited film, equation 4.2 was used [99],

$$(\alpha h\nu) = A(h\nu - E_g)^{1/2} \quad (4.2)$$

where  $A$  is constant,  $h\nu$  is the incident photon energy and  $E_g$  is the optical band gap energy. The optical band gap of the film was determined by using the extrapolation of linear part of  $(\alpha h\nu)^2$  versus  $(h\nu)$  graph and found as 1.46 eV. So, it is well-consistent with reported band gap values of CZTSe and CZTS compounds lying between 1.0 and 1.5 eV [17], [100].

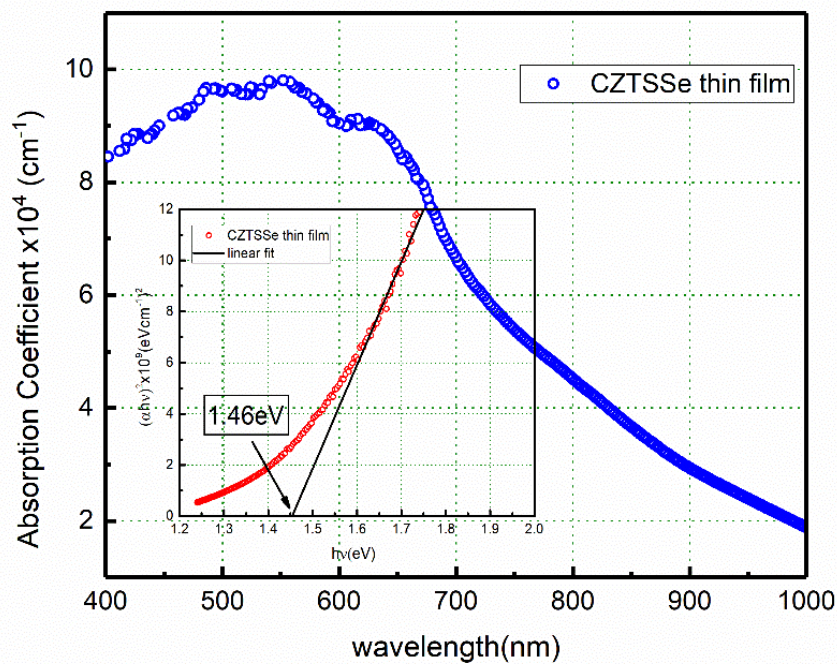


Figure 4.7. Absorption coefficient of deposited film and the inset shows Tauc plot used for band gap calculation of CZTSSe thin film.

### 4.3.3. Electrical Properties of CZTSSe Thin Film

A sample having van der Pauw geometry was utilized to determine the electrical properties of the deposited film. For this, Hall effect measurement at room-temperature and temperature dependent conductivity measurements under dark and illumination with intensity of 20, 35, 55, 80, 115 mW/cm<sup>2</sup> were conducted. With the help of the Hall effect measurement, the resistivity, carrier concentration and mobility of sample were found as 2.84 Ω.cm, 2.41x10<sup>17</sup>cm<sup>-3</sup> and 9.12 cm<sup>2</sup>/V.s, respectively. Sample showed p-type semiconductor behavior. On the other hand, conductivity measurement showed that conductivity is under the illumination is larger than dark conductivity as shown in Figure 4.8.

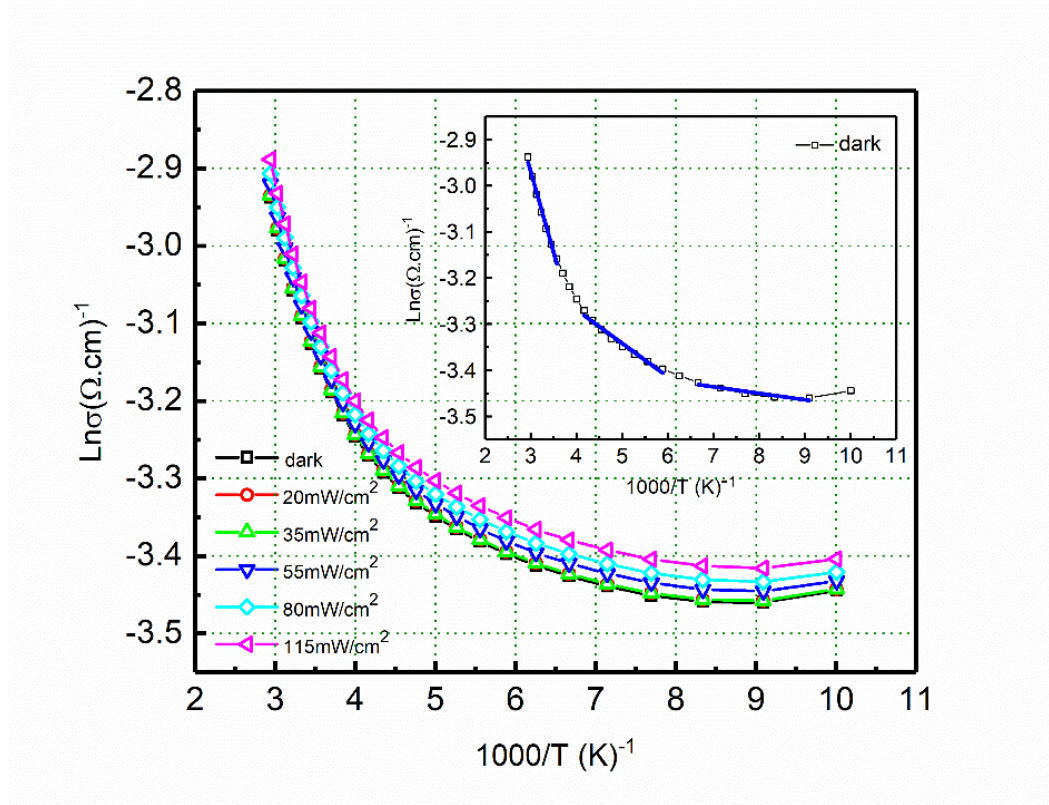


Figure 4.8. Temperature dependent electrical conductivity of deposited film. Inset shows the linearity of different temperature regions in dark.

Exponential behavior was observed in the conductivity with increasing ambient temperature, which justifies the semiconductor behavior of deposited film. The variation of conductivity can be expressed by the following equation [101] ,

$$\sigma = \sigma_o \exp\left(\frac{-E_a}{kT}\right) \quad (4.3)$$

where  $\sigma_o$  is the pre-exponential factor,  $E_a$  is the activation energy, k is the Boltzmann constant and T is the ambient temperature.

And also, the variation of dark conductivity can be studied by using three linear region; low, middle and high temperature regions (the inset of Figure of 4.8). Using the Eqn. 4.3, activation energy of each region was calculated as 1.2, 6.2 and 29.3 meV for 100-140 K, 150-240 K and 250-340 K temperature regions, respectively. The calculated activation energies indicate the intrinsic defects of the CZTSSe film.

#### 4.3.4. Device Behavior of In/CZTSSe/Si/Ag Structure

Having completed the analysis of the deposited thin film, the main diode parameters and dominant conduction mechanism through the junction of fabricated In-n-Si/CZTSSe/Ag structure were investigated by using the temperature dependent current voltage (I-V) measurements in the range of 250-350K. The schematic diagram of In/n-Si/CZTSSe/Ag was given in Figure 4.9.

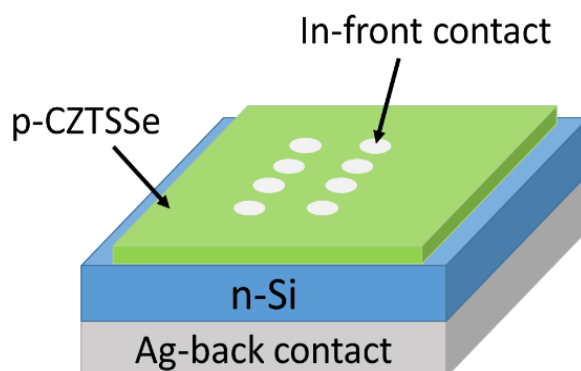


Figure 4.9. The schematic diagram of fabricated diode structure.

As shown the figure 4.10, the forward bias current showed exponential behavior with increments of bias voltage while reverse bias current of this diode demonstrated a good saturation behavior. The rectifying I-V behavior justified the formation of depletion region at the interface of CZTSSe/Si. In addition, the rectification factor (RF) which is defined as the ratio of forward current to reverse current ( $I_F/I_R$ ) at applied voltage was found to be two orders of magnitude at the room temperature. This ratio of current was observed in increasing behavior with increase in bias voltage at each temperature and decreasing behavior with increase in temperature at each bias voltage. This type of variation in RF value with temperature and bias voltage can be due to the effect of trap levels localized at the interface and inhomogenous trap distribution in the bulk of heterostucture [102], [103]. From the thermionic emission (TE) model, the measured I-V characteristics were analyzed by using standard diode equation [87], [104],

$$I = I_0 \left[ \exp\left(\frac{qV}{nkT}\right) - 1 \right] \quad (4.4)$$

where n is the ideality factor, q is the elementary charge, k is the Boltzmann constant, V is the applied voltage, T is the absolute temperature and  $I_0$  is the reverse saturation current defined as,

$$I_0 = AA^*T^2 \exp\left(-\frac{q\Phi_{B0}}{kT}\right) \quad (4.5)$$

where  $\Phi_{B0}$  is the zero-bias barrier height, A is the device area,  $A^*$  is the effective Richardson constant, which is calculated as  $112A\text{cm}^{-2}\text{K}^{-2}$  by applying TE theory for n type Si [105], [106].

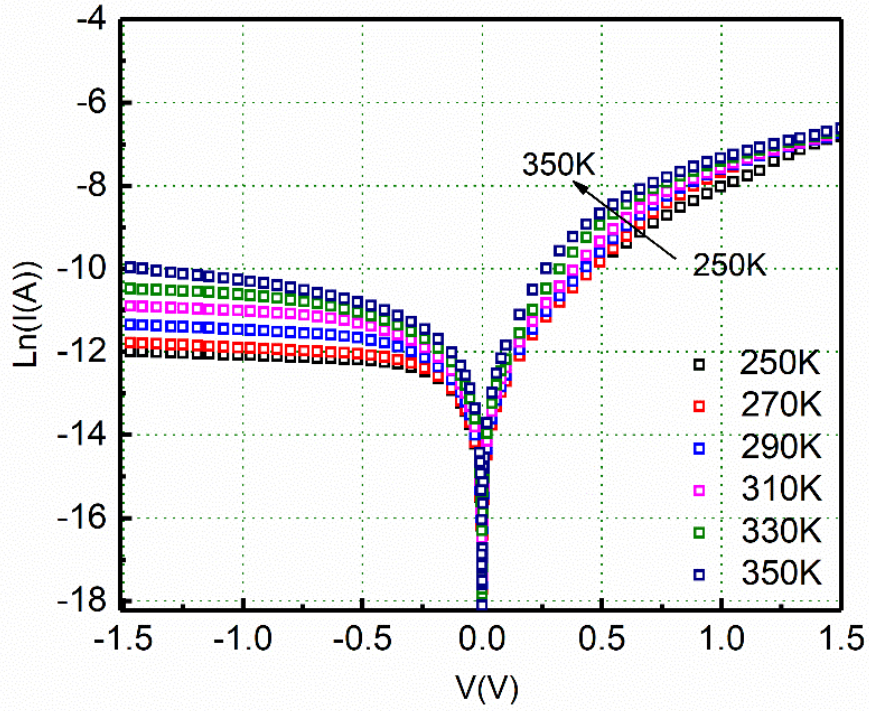


Figure 4.10. Temperature dependent current-voltage graph of Ag/Si/CZTSSe/In structure.

Ideality factor,  $n$ , is calculated from the slope of the linear part of the forward bias in semi logarithmic I-V characteristics using the following expression,

$$\frac{1}{n} = \frac{kT}{q} \frac{d(\ln I)}{dV} \quad (4.6)$$

The values of  $n$  and  $I_0$  which were derived from the fitting of  $\ln(I)$ -V graphs and the values of  $\Phi_{B0}$  which were calculated by using the Eqn. 4.5 at different temperatures were listed in Table 4.1. It was observed that ambient temperature affects the values of  $n$  and  $\Phi_{B0}$  strongly. Ideality factor exhibits decreasing behavior with increasing temperature, while zero bias barrier height displays the increasing behavior. These variations as a function of temperature are given in Figure 4.11. This implies the

deviation from the TE theory since these variations indicate the presence of defective structure and inhomogeneous interface [107], [108].

Table 4.1. Device parameters extracted from the analysis of temperature dependent I-V measurements

Temperature (K)	$n$	$I_o$ (A)	$\Phi_{B0}$ (eV)
250	4.82	$1.17 \times 10^{-6}$	0.55
270	4.42	$1.23 \times 10^{-6}$	0.58
290	4.10	$1.25 \times 10^{-6}$	0.62
310	3.80	$1.45 \times 10^{-6}$	0.66
330	3.29	$1.63 \times 10^{-6}$	0.71
350	2.89	$2.12 \times 10^{-6}$	0.75

In general, ideality factor of an ideal diode is expected to be the unity, corresponding to pure thermionic emission mechanism. However, other conduction mechanisms contribute to carrier transport when ideality factor is higher than the unity.

According to Tung's theory, both temperature dependency of  $n$  and  $\Phi_{B0}$  and the linear relationship between  $n$  and  $\Phi_{B0}$  and the linearity (given in Figure 4.12) indicates the presence of lateral inhomogeneity of barrier height with low barrier patches [109], [110].

Such behavior is explained that there is a potential fluctuations at the junction consisting of low and high barrier regions. So, in the diode, the current will flow through the lower barriers preferentially. The fluctuations of the potential are attributed to the interfacial states at the interface [109], [110].

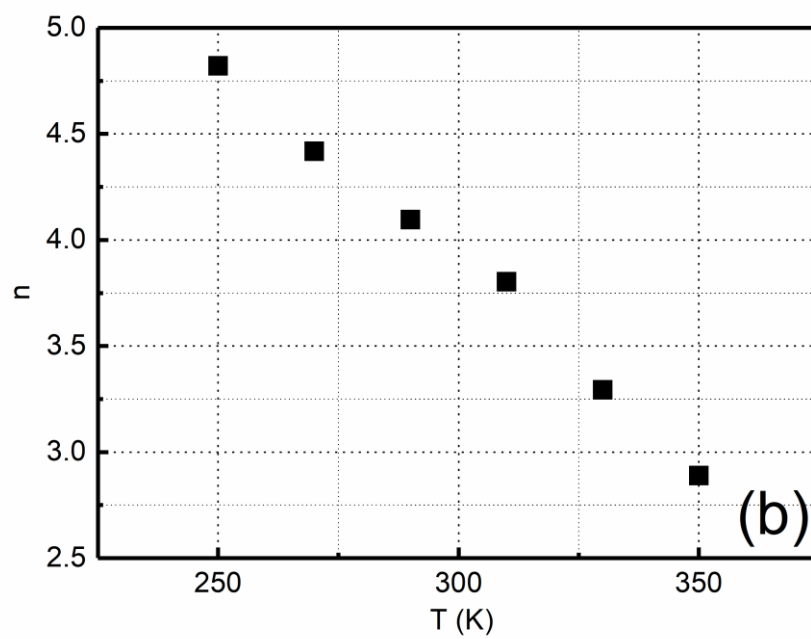
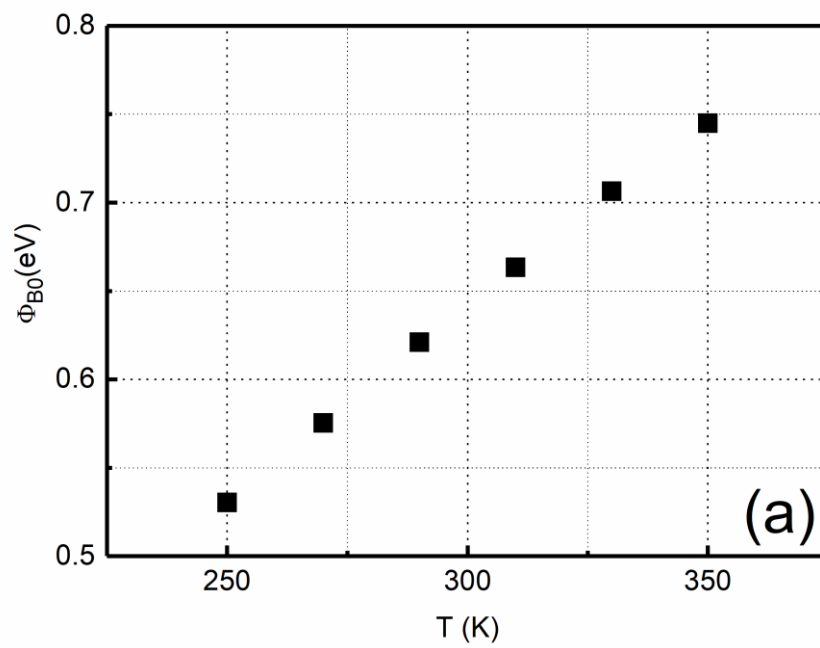


Figure 4.11. The variations of (a) zero bias barrier height and (b) ideality factor with temperature.

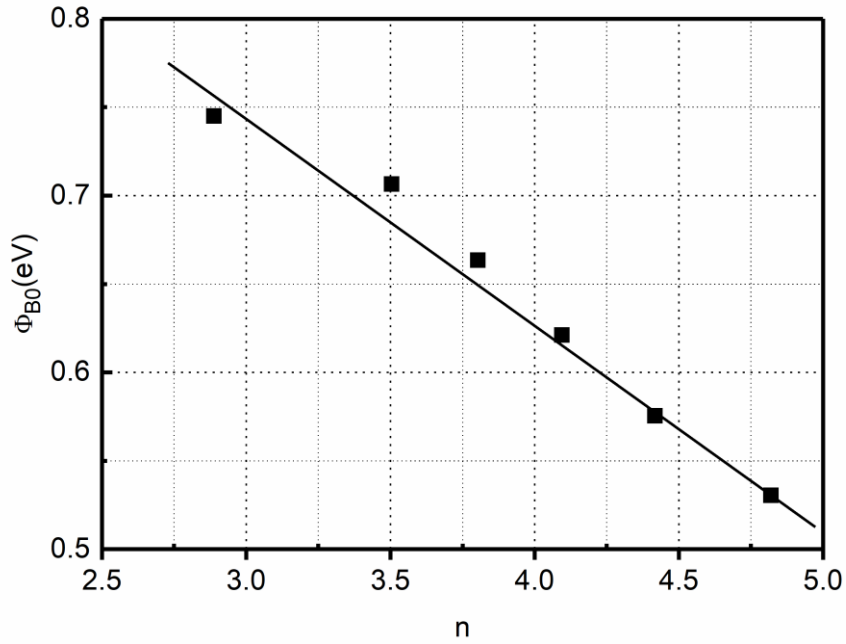


Figure 4.12. Zero bias barrier height vs ideality factor graph of CZTSSe/Si structure.

The extrapolation of Figure 4.12 to the unity ( $n=1$ ) showed value of the homogenous barrier height as 1.10 eV. It can be deduced that there is a significant decreases in zero bias barrier height and increases in ideality factor at low temperature region especially, which results from the barrier inhomogeneity at the interface. Thus, the observed abnormal behaviors can be expressed by taking into consideration potential fluctuations model which is based on inhomogeneous barrier heights at the interface [111]–[114]. For this purpose, Gaussian distribution (GD) of the barrier heights with a mean value  $\bar{\Phi}_{B0}$  and standard deviation  $\sigma_0$  is introduced as follows [115],

$$P(\Phi_{ap}) = \frac{1}{\sigma_0\sqrt{2\pi}} \exp\left[-\frac{(\Phi_{ap} - \bar{\Phi}_{B0})^2}{2\sigma_0^2}\right] \quad (4.7)$$

where  $\frac{1}{\sigma_0\sqrt{2\pi}}$  is the normalization constant of the GD and the total current I is defined by,

$$I(V) = \int_{-\infty}^{+\infty} I(\Phi_{ap}, V) P(\Phi_{ap}) d\Phi_{ap} \quad (4.8)$$

On integration, total current at a bias V is defined as,

$$I = AA^*T^2 \exp \left[ \left( -\frac{qV}{kT} \right) \left( \bar{\Phi}_{B0} - \frac{q\sigma_0^2}{2kT} \right) \right] \exp \left( \frac{qV}{n_{ap}kT} \right) \left[ 1 - \exp \left( -\frac{qV}{kT} \right) \right] \quad (4.9)$$

with modified reverse saturation current,

$$I_0 = AA^*T^2 \exp \left( -\frac{q\Phi_{ap}}{kT} \right) \quad (4.10)$$

where  $I_0$  is the saturation current,  $\Phi_{ap}$  is the apparent barrier height and  $n_{ap}$  is the apparent ideality factor. In addition, in this model, the apparent barrier height is expressed as [116],

$$\Phi_{ap} = \bar{\Phi}_{B0} (T = 0 \text{ K}) - \frac{q\sigma_0^2}{2kT} \quad (4.11)$$

As given in the Figure 4.13 , using the graphical representation of the apparent barrier heights as a function of  $q/2kT$ , the mean barrier height and standard deviation were found as 1.27 eV and 0.18, respectively. In this model,  $\sigma_0$  is a measure of barrier inhomogeneity in which the lower value of  $\sigma_0$  indicates more homogenous barrier height. It was observed that the value of  $\sigma_0$  is the 14% of the obtained  $\bar{\Phi}_{B0}$  , which means larger inhomogeneity at the interface of CZTSSe/Si [117].

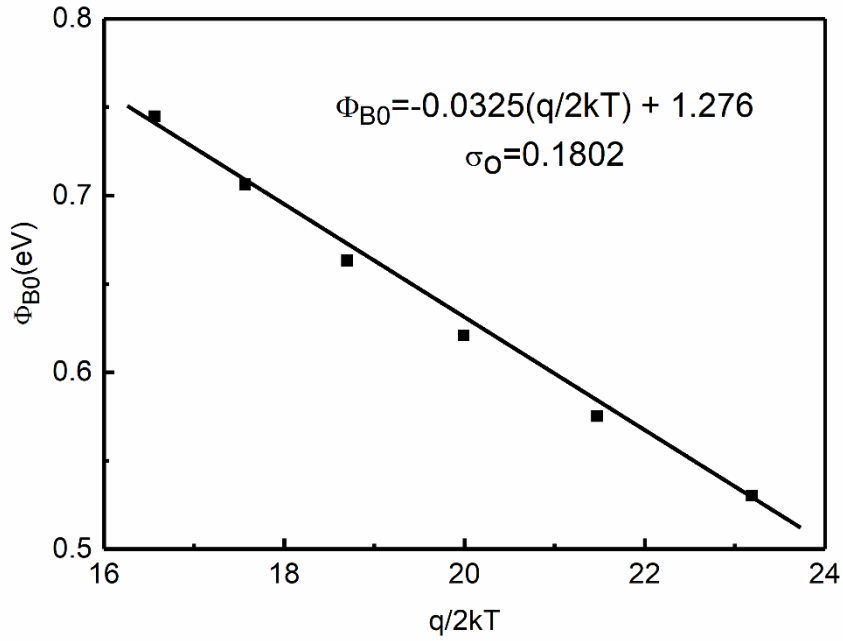


Figure 4.13. The plot of  $\Phi_{B0}$  vs  $q/2kT$  for CZTSSe/Si structure.

In this model, the expression of apparent ideality factor is given by,

$$\left( \frac{1}{n_{ap}} - 1 \right) = -\rho_2 + \frac{q\rho_3}{2kT} \quad (4.12)$$

where  $\rho_2$  and  $\rho_3$  are the voltage coefficients which quantify the deformation of barrier height distribution with voltage. Using the linearity of the  $(n^{-1}-1)$  versus  $q/2kT$  plot,  $\rho_2$  and  $\rho_3$  were found as 0.0187 V and 0.3725 V, respectively (Figure 4.14). The linearity of this plot also confirms the presence of voltage deformation of Gaussian distributed barrier heights [111].

Moreover, the conventional Richardson plot is modified by combining the Eqn. 4.10 and 4.11 due to the inhomogeneity of the barrier heights as follows;

$$\left(\frac{I_0}{T^2}\right) - \left(\frac{q^2 \sigma_s^2}{2k^2 T^2}\right) = \ln(AA^*) - \frac{q\bar{\Phi}_{B0}}{kT} \quad (4.13)$$

As shown in Figure 4.15, the modified Richardson plot was fitted a straight line and the slope and intercept of this line yield the  $\bar{\Phi}_{B0}$  and  $A^*$  which were calculated as 1.28 eV and  $120.46 \text{ Acm}^{-2}\text{K}^{-2}$ , respectively. It is clearly seen that value of  $\bar{\Phi}_{B0} = 1.28 \text{ eV}$  is in good agreement with the obtained value from the plot of  $\Phi_{B0}$  vs  $q/2kT$ . Also, the modified Richardson constant  $A^* = 120.46 \text{ Acm}^{-2}\text{K}^{-2}$  is in close agreement with the theoretical value of n-Si [105].

To evaluate the photovoltaic behavior of CZTSSe/Si structure, I-V characteristics under dark and illumination ( $100 \text{ mW/cm}^2$ ) were carried out at room temperature.

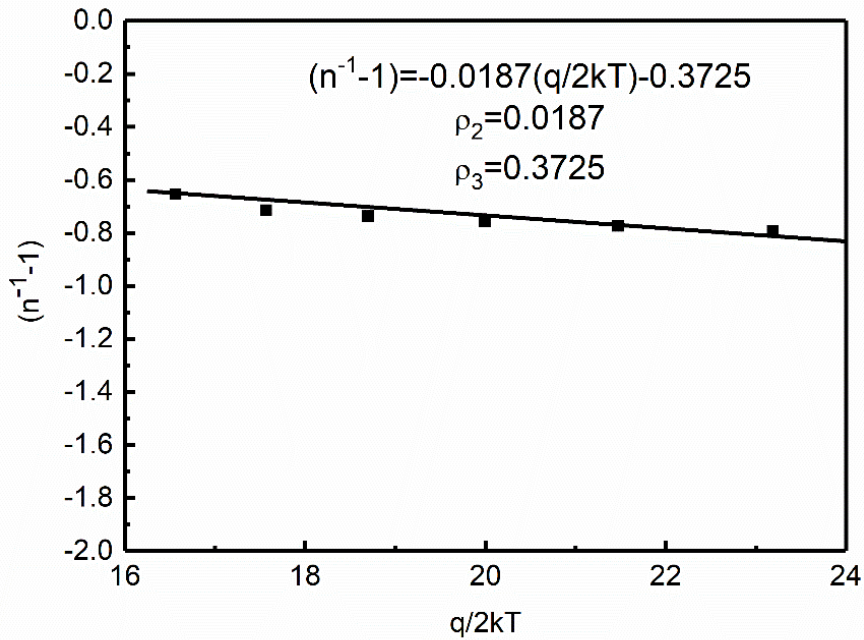


Figure 4.14. The plot of  $(n^{-1} - 1)$  vs  $q/2kT$ .

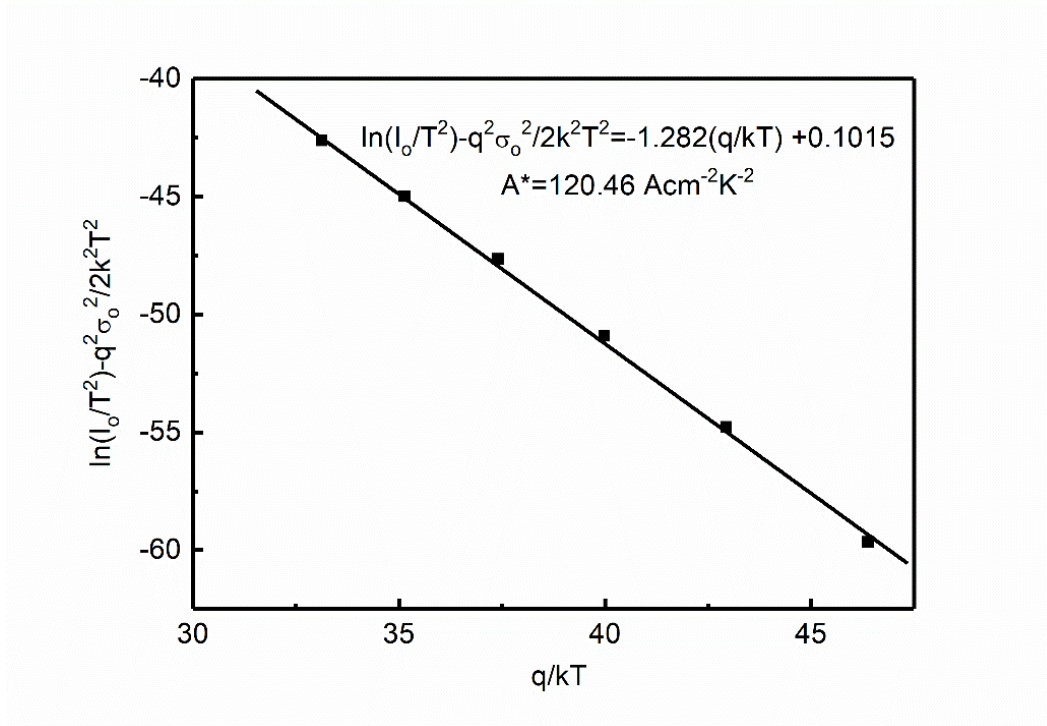


Figure 4.15. The modified Richardson plot of  $\ln(I_0/T^2) - (q^2\sigma_0^2)/(2k^2T^2)$  vs  $q/kT$ .

Semi-logarithmic I-V graph of CZTSSe/Si structure at room temperature was given in Figure 4.16a. It was observed that this structure demonstrates the low response to illumination. And also, open circuit voltage ( $V_{oc}$ ) and short circuit current density ( $J_{sc}$ ) were found as 50 mV and  $0.44 \text{ mA}\cdot\text{cm}^{-2}$ , respectively (Figure 4.16b).

Interfacial states play an important role in the electronic properties of devices. To calculate the interface state density ( $D_{it}$ ), frequency dependent capacitance-voltage and (C-V) and conductance- voltage (G/w-V) characteristics of CZTSSe/Si structure in the range of 5-1000 kHz were studied at room temperature. C-V and G/w-V characteristics of this structure were depicted in Figure 4.17 and 4.18, respectively. As shown in Figure 4.17, it was observed that decreasing behavior in the capacitance with the applying ac signal, which is attributed to the switching the majority carriers between the majority carrier band of semiconductor and interface states.

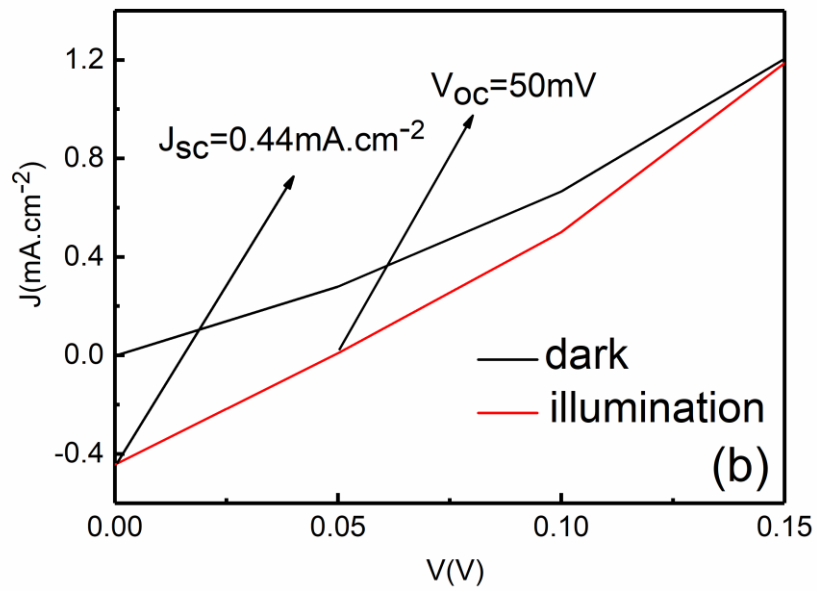
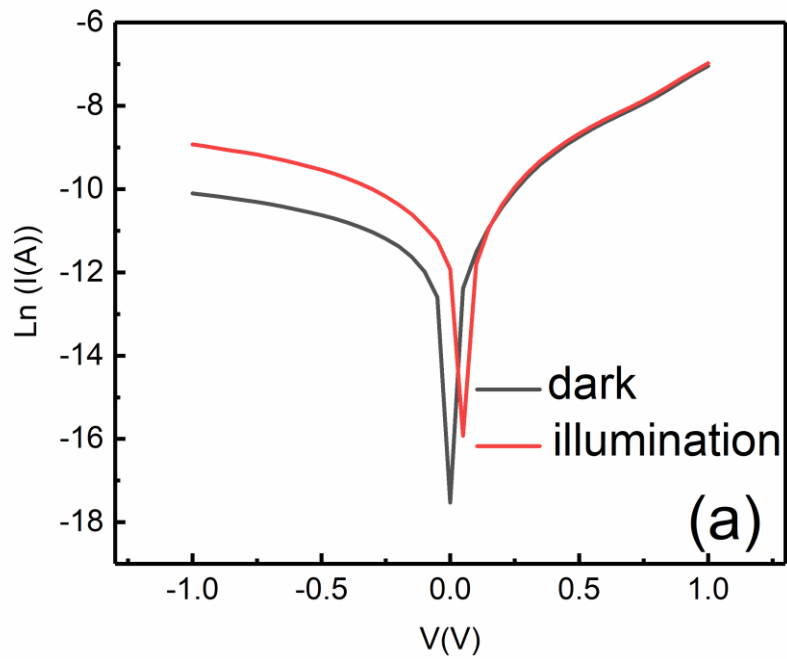


Figure 4.16. Under dark and illumination at room temperature, the plots of (a) semi logarithmic I-V and (b) J-V in the voltage range of 0 and 0.15 V.

It was also obtained decreasing trend in both C-V and G/w-V characteristics with increasing frequency. In addition, anomalous peak was obtained in the C-V profile and this peak decreased with increasing frequency. Such behavior imply the presence of localized interface states since interface states could follow the *ac* signal at low frequency which results in excess capacitance. However, at high frequency, interface states could not follow the ac signal due to the response time of interface states [105].

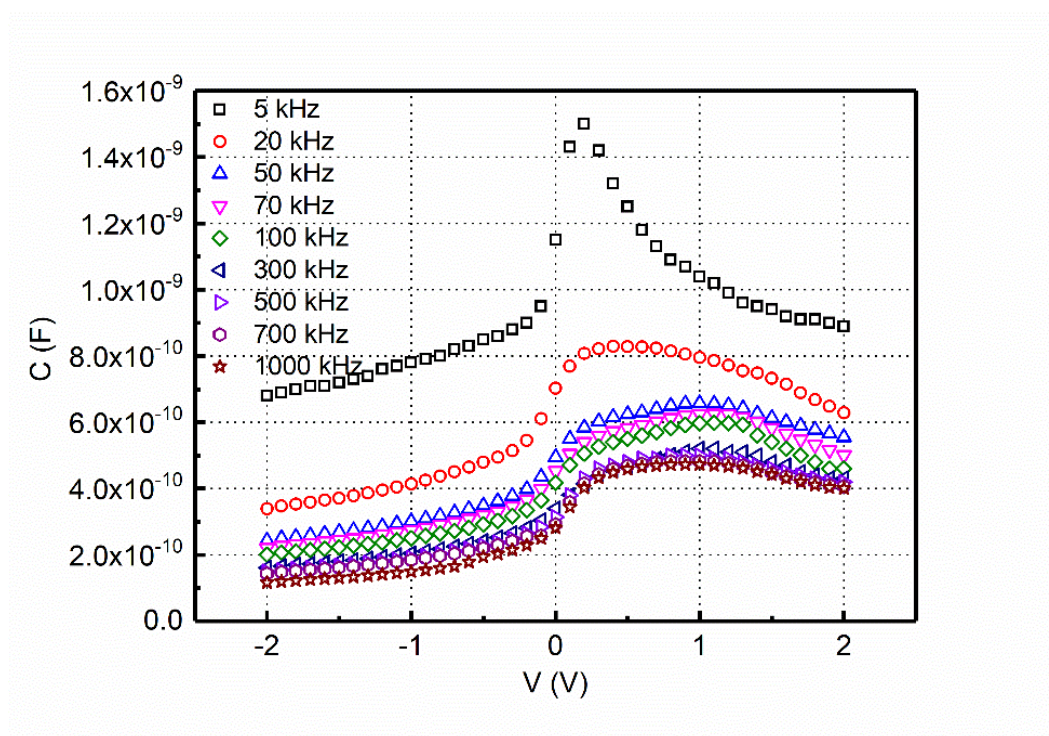


Figure 4.17. Frequency-dependent capacitance voltage characteristics of CZTSSe/Si structure.

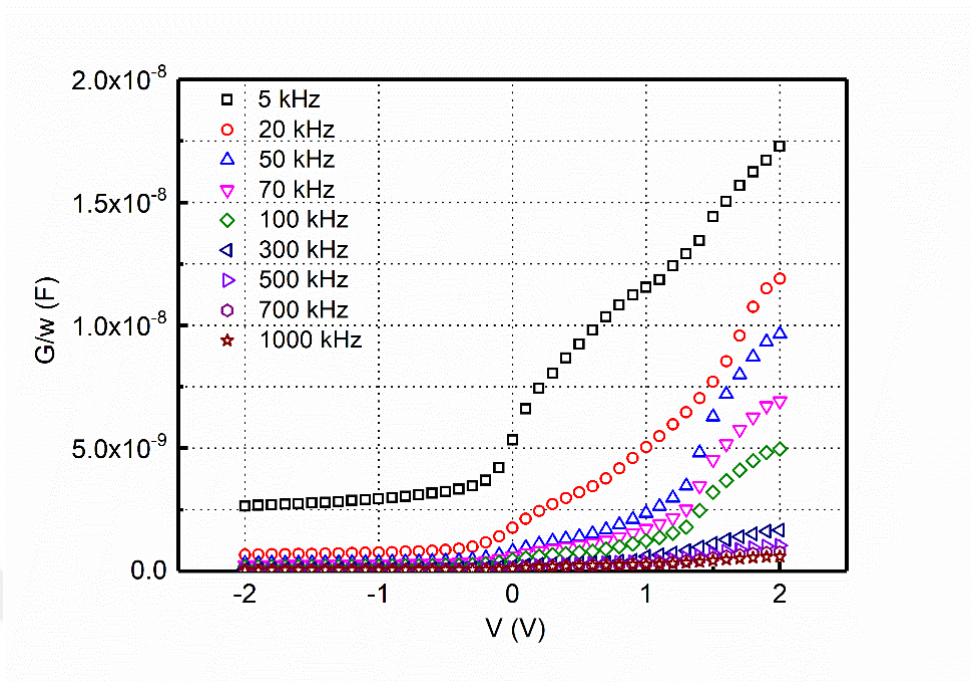


Figure 4.18. Frequency-dependent conductance voltage characteristics of CZTSSe/Si structure.

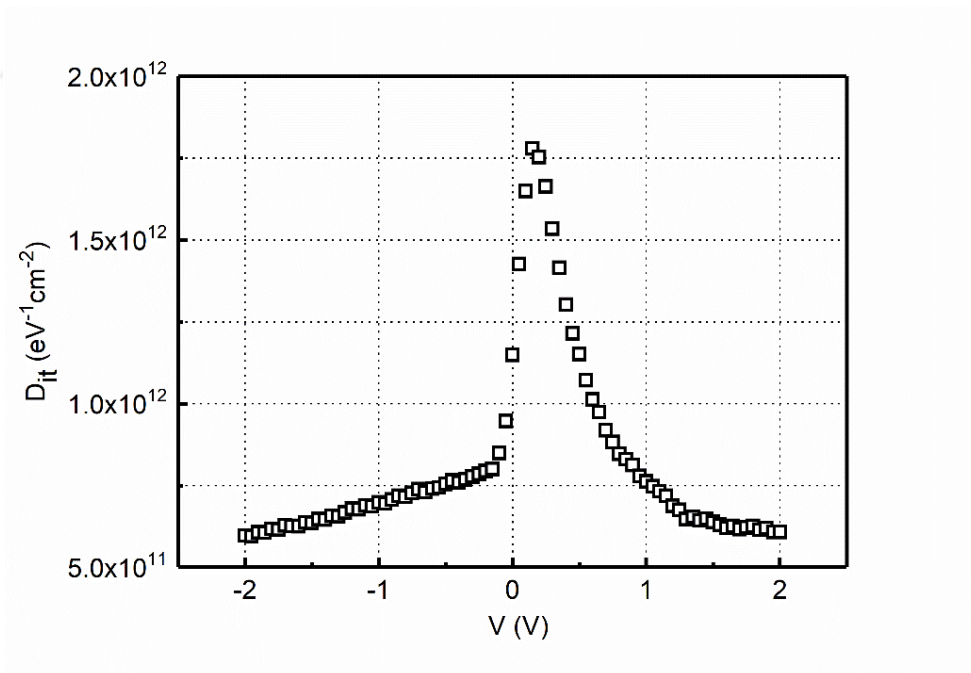


Figure 4.19. The profile of density of interface states achieved from  $C_{HF}-C_{LF}$  capacitance method.

Several methods have been utilized to calculate the density of interface states. In this study, high-low frequency capacitance ( $C_{HF}$ - $C_{LF}$ ) method and Hill-Coleman method were applied among them since they are most appropriate methods to obtain density of interface states as a function of voltage and frequency, respectively [118], [119].

In the  $C_{HF}$ - $C_{LF}$  method, interface layer capacitance ( $C_i$ ) is connected in a series with the parallel combination of interface states capacitance ( $C_{it}$ ) and space charge capacitance ( $C_{sc}$ ).  $C_{it}$  is defined as follows,

$$C_{it} = \left( \frac{1}{C_{LF}} - \frac{1}{C_i} \right)^{-1} - C_{sc} \quad (4.14)$$

Since interface states cannot response to external *ac* signal at high frequency as mentioned above, they does not contribute the total capacitance. So, the equivalent capacitance is expressed by the series connection of  $C_i$  and  $C_{sc}$  as given below,

$$\frac{1}{C_{HF}} = \frac{1}{C_i} + \frac{1}{C_{sc}} \quad (4.15)$$

and thus,  $D_{it}$  is evaluated at given bias by combining the Eqn 4.14 and 4.15 as follows,

$$qAD_{it} = C_{it} = \left[ \frac{1}{C_{LF}} - \frac{1}{C_i} \right]^{-1} - \left[ \frac{1}{C_{HF}} - \frac{1}{C_i} \right]^{-1} \quad (4.16)$$

where  $q$  is the elementary charge,  $A$  is the active diode area,  $C_{HF}$  is the measured the highest frequency capacitance (1MHz) and  $C_{LF}$  is the lowest frequency capacitance (5 kHz). The variation of  $D_{it}$  as a function of voltage was given in Figure 4.19. It was obtained a peak at 0.15 V in the profile of  $D_{it}$ -V. For the evaluation of  $D_{it}$ , Hill-

Coleman method can be also applied. According to Hill-Coleman,  $D_{it}$  is defined as [120],

$$D_{it} = \left(\frac{2}{qA}\right) \frac{(G_m/w)_{max}}{[(G_m/w)_{max}/C_i]^2 + (1 - C_m/C_i)^2} \quad (4.17)$$

where  $w$  is the angular frequency ( $= 2\pi f$ ),  $C_m$  and  $(G_m/w)_{max}$  are the measured capacitance and conductance value, corresponding to the peak values and  $C_i$  is the capacitance of insulator layer. The values of  $D_{it}$  decreased with increasing frequency indicating characteristic of  $D_{it}$  as a function of frequency in Figure 4.20. Thus, it is seen that the interface state density values determined by two different methods are approximately in the same order.

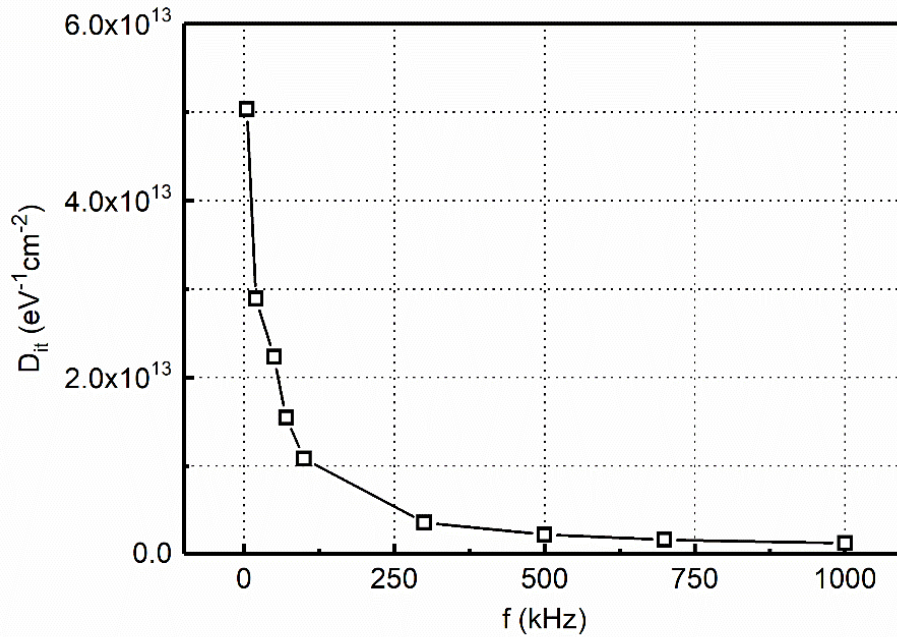


Figure 4.20. The density profile of states obtained by from the Hill-Coleman method.



## CHAPTER 5

### CONSTRUCTION OF SELF ASSEMBLED NANOFILAKES ON CZTSSSE THIN FILMS

#### 5.1. Introduction

CZTSSe is a promising alternative absorber material to achieve high power conversion efficiencies, besides its property of involving low-cost and earth-abundant elements when compared to Cu(In,Ga)Se<sub>2</sub> (CIGS) and cadmium telluride (CdTe), to be used in solar cell technology. On the other hand, low dimensional nanostructure materials such as nanowires, nanosheets and nanoflakes have been attracting much attention due to their versatile properties and potential applications in recent years. It has been reported that nanostructures with high surface area allow for increasing light trapping and decreasing minority carrier recombination [121]–[123].

In this work, a novel method was introduced to fabricate CZTSSe thin films with self-assembled nanoflakes on the surface by using RF magnetron sputtering through fine tuning of the deposition conditions in which sequential stacked layers were used as precursors. The effect of post-annealing on the structural properties of CZTSSe thin films was studied and various characterization techniques were utilized to elucidate the formation of CZTSSe thin film having a surface decorated with vertical nanoflakes. Possible mechanism behind the vertical growth was discussed in details. Also, it was obtained that the size of nanoflakes is tunable by adjusting the thickness of stacked layers. To further explore the formation of vertically standing layers, the effect of substrate temperature was investigated. As a result, it was deduced that these processes are repeatable, controllable and suitable for large-scale production.

## 5.2. Experimental Procedure

CZTSSe thin films having self-assembled nanoflakes on the film surface were deposited on SLG substrate by three magnetron RF sputtering technique using stacked precursors without post selenization or sulphurization. 3 inch-diameter sputtering targets ZnSe (99.99%), CuSe (99.99%) and SnS (99.99%) were used as precursors with the stacking order of glass/ZnSe/CuSe/SnS/ZnSe/CuSe/SnS in order to eliminate the metallic film surface as given in figure 5.1. Sequential stacked deposition of precursors provides to control the compositional ratio of film by adjusting the thickness of stacking layer easily. Thickness of each stacked precursors was determined to obtain 2  $\mu\text{m}$  stoichiometric CZTSSe thin film as 250, 500 and 250 nm for ZnSe, CuSe and SnS precursors, respectively.



Figure 5.1. Schematic presentation of stacking order of precursors

This study was mainly focused on the effect of each stacked precursors on the surface characteristics of thin film structure, thickness and substrate temperature dependencies of vertically standing CZTSSe layers on the film surface. Therefore, in addition to the analysis of chemical mapping analysis of the proposed stacked layers, this work was built on the basis of the results obtained from four different depositions by following the same deposition route. Each deposition was carried out in the same deposition route optimized as in the proposed six stacked precursors sequence. The base pressure

of the chamber was pumped down to about  $10^{-6}$  Torr prior to deposition. All targets oriented in a confocal position 10 cm below the substrate holder were pre-sputtered in the argon atmosphere for 10 minutes to get rid of impurities that might be on the target surface. The chimney and shutter systems in front of each sputter flange can help to grow uniform and pure layer on the substrate surface in an expected stacking order. It was observed that there were minor effects on the nanoflake formation in the optimization processes of chamber pressure, argon flow and RF magnetron power density on targets. Therefore, for each deposition, the deposition pressure of RF sputtering was adjusted to  $1 \times 10^{-3}$  Torr with continuous 6 sscm argon flow after reaching pre-deposition chamber pressure at about  $10^{-6}$  Torr. All layers were deposited in optimized layer thicknesses by RF magnetron sputtering of ZnSe, CuSe and SnS targets with a power density of  $1.75 \text{ W/cm}^2$ . During the deposition, the deposition rate was kept in the range of  $2\text{-}5 \text{ \AA/s}$  and substrates were also rotated to give high homogeneity to each film layer. For all of the film samples, the thickness of the film was adjusted to  $2 \text{ }\mu\text{m}$  by monitoring and controlling each layer thickness using Inficon XTM/2 thickness monitor. It was chosen as considering that a few micrometer thick films is enough due to strong absorption comparing the optimum values reported in the literature. The sample deposited at  $150 \text{ }^\circ\text{C}$  substrate temperature is named as D1 and the thickness dependency of the formation of nanoflakes was investigated via second deposition with  $1 \text{ }\mu\text{m}$  final thickness (D2) following the same deposition route with half-thick layers. After the deposition, samples were allowed to cool down to the room temperature and named as as-deposited. Furthermore, to investigate the effect of deposition temperature on the formation of self-assembled nanoflakes, the samples were also grown at different substrates temperatures of  $100^\circ\text{C}$  (D3) and  $200^\circ\text{C}$  (D4) by keeping other growth conditions the same and deposition parameters were also given in Table 5.1. The morphological and compositional properties of the deposited films were investigated by Quanta 400 FEG model scanning electron microscopy (SEM) equipped with energy dispersive X-ray spectroscopy analysis (EDS) system and transmission electron microscopy (TEM, Jeol 2100F HRTEM). The thicknesses of the as-deposited and annealed films on SLG substrates were also measured

electromechanically by a Dektak 6M profilometer in the error limit of 1 nm using a stylus tip radius of 12.5  $\mu\text{m}$ . The X-ray diffraction (XRD) measurements were performed by using a Rigaku Miniflex XRD system equipped with a  $\text{CuK}\alpha$  radiation source with average wavelength of 1.54  $\text{\AA}$ . Raman scattering measurements were also carried out by using Renishaw inVia confocal Raman microscope and a laser with the wavelength of 532 nm used as an excitation source.

Table 5.1. Experimental conditions and process parameters of D1, D2, D3 and D4

<i>Deposition Paramaters</i>	<i>D1</i>	<i>D2</i>	<i>D3</i>	<i>D4</i>
Substrate temperature ( $^{\circ}\text{C}$ )	150	150	100	200
Recorded thickness ( $\mu\text{m}$ )	~2	~1	~2	~2
Deposition pressure (Torr)	$1 \times 10^{-3}$	$1 \times 10^{-3}$	$1 \times 10^{-3}$	$1 \times 10^{-3}$
Ar flow (sscm)	6	6	6	6
RF power to ZnS target (W)	80	80	80	80
RF power to CuSe target(W)	80	80	80	80
RF power to SnS target(W)	80	80	80	80
Targets diameter (inch)	3	3	3	3
Target to substrate distance (cm)	10	10	10	10
Deposition rate ( $\text{\AA}/\text{sec}$ )	2-5	2-5	2-5	2-5

The optical characterization of the samples was performed by using 8-inch, 5port integrating sphere (Oriel 7067NS) and photoluminescence measurement was conducted with 532 nm ND-Yag laser 200mW, Oriel ms257 monochromator equipped with Hamamatsu C7040 CCD detector.

### 5.3. Results and Discussion

#### 5.3.1. Effect of Precursor Thickness on the Nanoflakes

XRD patterns of the as-deposited and annealed thin film samples of D1 and D2 were given in Figure 5.2 indicating polycrystalline structure in as-deposited form and improvement in single phase crystallization after the post-annealing process. Strong diffraction peaks were detected at  $27.8^\circ$ ,  $45.9^\circ$ ,  $54.3^\circ$ ,  $74.2^\circ$  corresponding to diffraction of (112), (220), (312) and (316) planes of CZTSSe structure (ICDD data #00-052-0868 CZTSSe and ICDD data#00-026-0575 CZTS) [124].

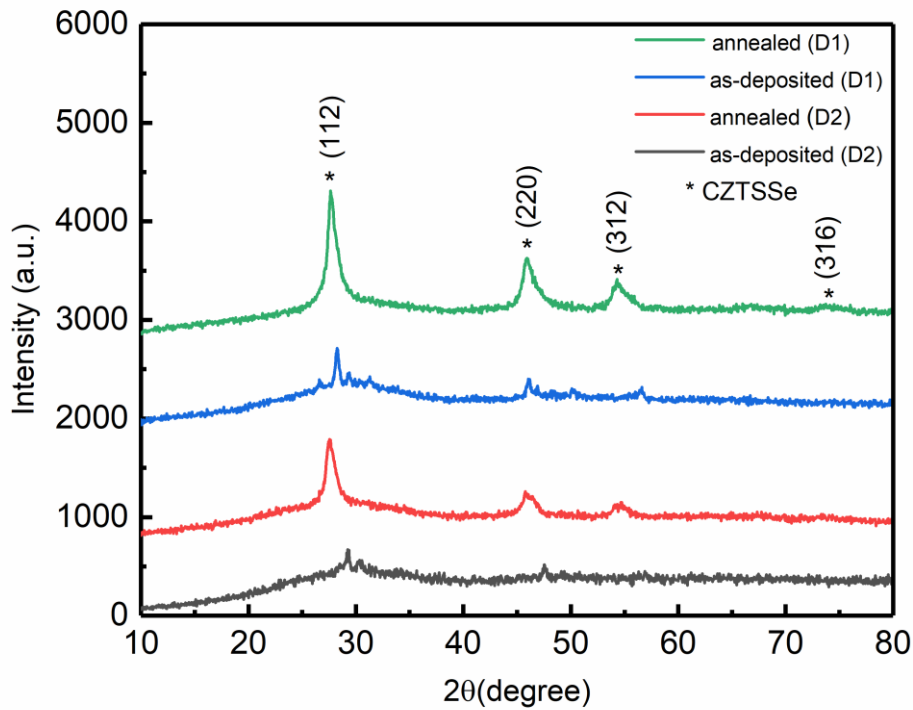


Figure 5.2. XRD spectra of as-deposited and annealed samples of D1 and D2

Different from the main quaternary structure, any other reflections indicating the secondary phases were not detected in XRD pattern of the annealed samples within the instrumental accuracy, which demonstrates the effect of thermal annealing on the

structural properties of the samples. As mentioned in the experimental details of the work, the effect of the film thickness on the size of the nanoflakes that randomly distributed on the surface of the film was investigated via the half-thick sample (D2) in which, each stacked layer was deposited by half of its previous value (D1).

Table 5.2. Structural parameters of CZTSSe films acquired from XRD patterns of annealed D1 and D2 samples

<i>Parameters</i>	<i>annealed (D1)</i>	<i>annealed (D2)</i>
Peak degree (°)	27.8	27.6
Diffraction plane	(112)	(112)
Crystallite size (nm)	13.4	11.8
Dislocation density ( $\delta$ ) ( $m^{-2}$ )	$5.57 \times 10^{15}$	$7.18 \times 10^{15}$
Microstrain ( $\epsilon$ )	0.003	0.003
Lattice strain (LS)	0.012	0.013

After the deposition, as-deposited D2 samples were also exposed to heat-treatment to observe the effects of post-annealing treatment. Similar to the thick sample (D1), single CZTSSe phase was observed in XRD pattern of as-deposited D2 samples and strong crystallization with a preferred (112) orientation in annealed samples as inferred from Figure 5.2. At the substrate temperature of 150°C, the structural parameters of the strongly crystallized samples were calculated in order to detail the structural quality in these films.

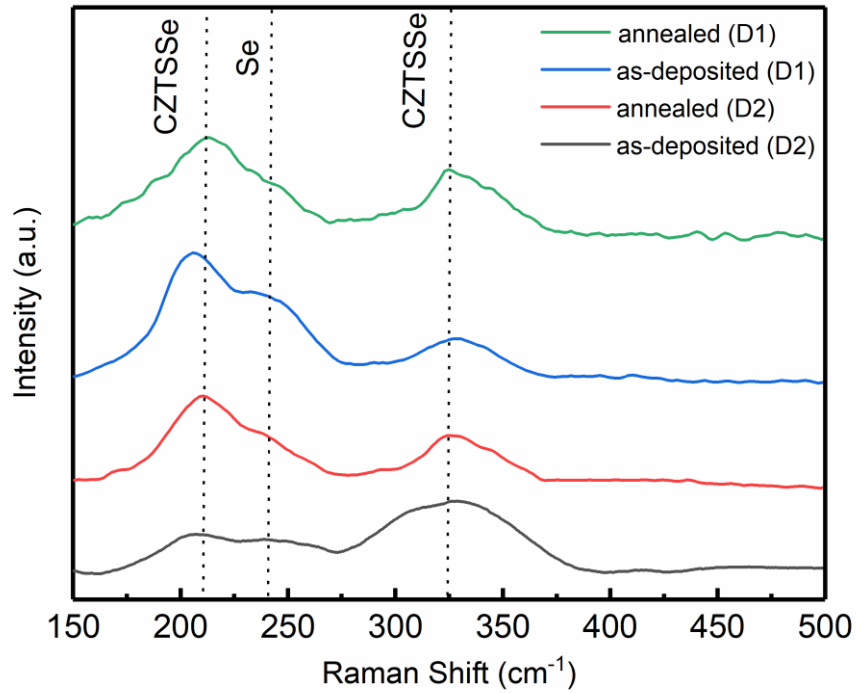


Figure 5.3. Raman spectra of as-deposited and annealed films of D1 and D2

Using the XRD profiles of annealed films, average grain size values were estimated using the well-known Debye-Scherrer's equation as follows ,

$$GS = \frac{0.94\lambda}{\beta \cos \theta} \quad (5.1)$$

where  $\lambda$  is the wavelength of x-ray ( $\lambda = 1.54 \text{ \AA}$ ) and  $\beta$  is the full width half maxima (FWHM) which is calculated in radians and  $\theta$  is the Bragg diffraction angle. In addition, related to the crystal defect and lattice mismatch in the structure, the parameters such as dislocation density ( $\delta$ ), microstrain ( $\varepsilon$ ) were calculated by using the equations below [125],

$$\delta = 1/(GS)^2 \quad (5.2)$$

$$\varepsilon = (\beta \cos \theta) / 4 \quad (5.3)$$

Also, lattice strain (LS) was evaluated by taking into consideration of the following equation,

$$LS = \frac{\beta}{4 \tan \theta} \quad (5.4)$$

All calculated parameters for the annealed samples of D1 and D2 were tabulated in Table 5.2. These results showed that the decrease in each layer thickness and as a result in the total film thickness triggers the increase in the imperfections in the structure.

In order to verify the phase purity of CZTSSe structure, Raman analysis was also carried out using 532 nm laser excitation source. The characteristic peaks of CZTSSe structure centered at around  $210 \text{ cm}^{-1}$  and  $324 \text{ cm}^{-1}$  were detected in Raman spectrum of the deposited films, as illustrated in Figure 5.3 [126].

These peaks are attributed to  $A_1$  mode vibration of Se and S atoms, respectively since CZTSSe compound shows bimodal behavior in Raman spectrum and centered position of  $A_1$  modes may shift to the higher wavenumber in Raman spectra with the increasing ratio of S/(S+Se). The broaden Raman peaks show that there is a structural disorder related to the random distribution of S and Se atoms in the lattice [95]. In addition, in the Raman spectrum of the as-deposited sample, one more peak was detected at  $240 \text{ cm}^{-1}$  corresponding to elementary Se peak [127]. This could be explained due to the Se aggregation at some region of the film surface before the annealing process. The atomic compositions of the CZTSSe thin films which were obtained by EDS measurements with  $\pm 2\%$  detection error were given in Table 5.3. Results of EDS measurements showed that the post-annealing process has no significant effect on the elemental composition of thin films. It was also observed that both as-deposited and annealed samples of D1 are Zn-poor and Sn-rich slightly, while the ratios of Cu/(Zn+Sn) are around unity.

Table 5.3. Elemental compositional analysis of CZTSSe thin films acquired from EDS measurements

<i>Samples</i>	<i>Cu(at%)</i>	<i>Zn (at%)</i>	<i>Sn (at%)</i>	<i>S (at%)</i>	<i>Se (at%)</i>	<i>Zn/Sn</i>	<i>Cu/(Zn+Sn)</i>
as-deposited (D1)	22	9	13	21	35	0.69	1.00
annealed (D1)	25	9	14	19	33	0.64	1.08
as-deposited (D2)	16	10	12	22	40	0.83	0.72
annealed (D2)	21	12	12	20	35	1.00	0.88
as-deposited (D3)	21	8	10	17	44	0.80	1.16
annealed (D3)	26	11	11	16	36	1.00	1.18
as-deposited (D4)	23	9	12	24	32	0.75	1.09
annealed (D4)	24	10	13	22	31	0.76	1.04

On the other hand, the stoichiometry was not obtained with decreasing the thickness of the film (D2) , and the change in the relative atomic ratios of the constituent elements may be due to the limited distribution of the precursors on the substrate surface in a shorten time interval.

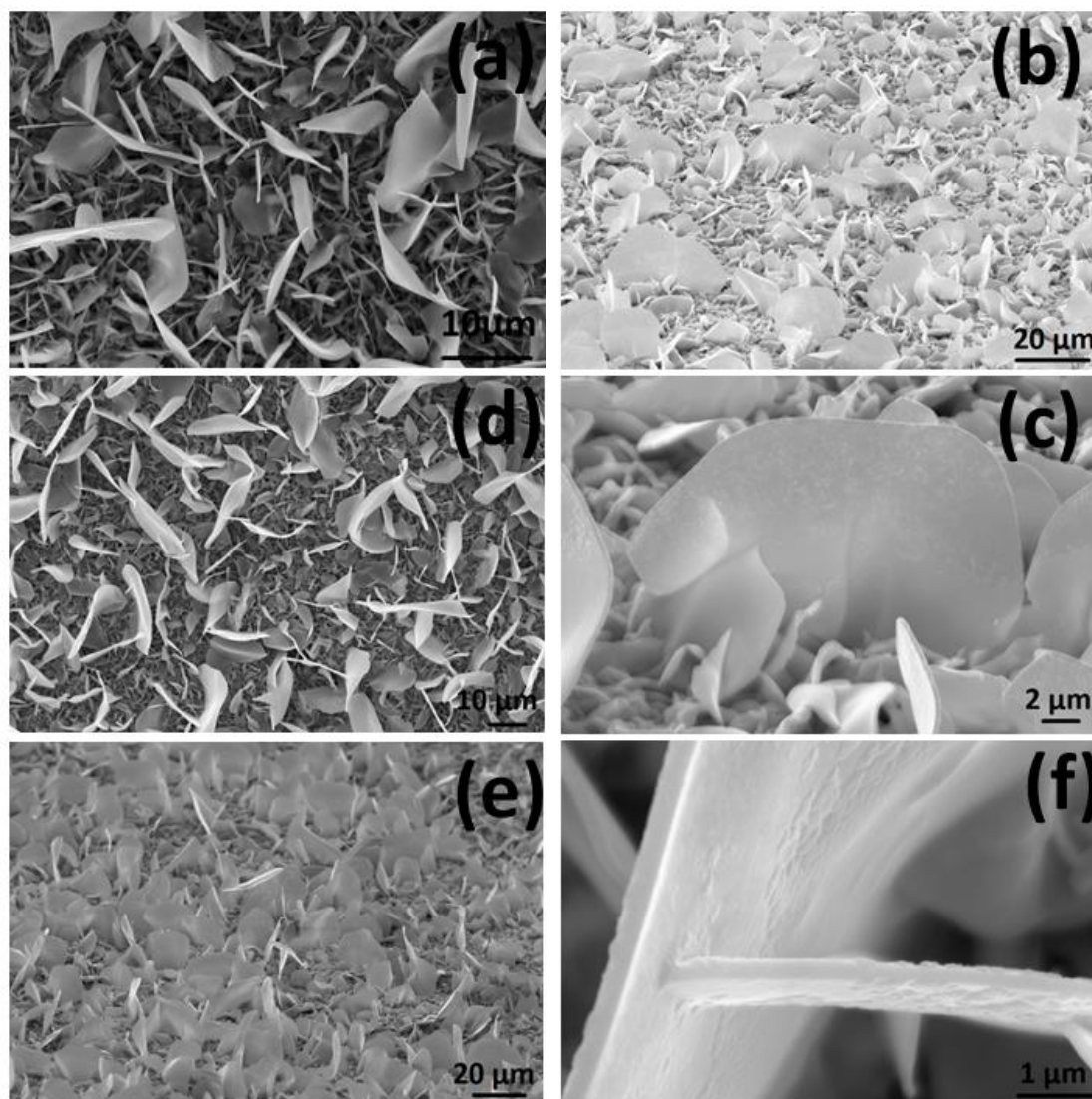


Figure 5.4. (a) Top view, (b) and (c) tilted SEM images of as deposited D1 film, (d) top view, (e) and (f) tilted SEM images of annealed D1 film.

Figure 5.4 shows the top view and tilted SEM images of as-deposited and annealed D1 films. It can be seen that surface of the substrates covered randomly distributed vertical nanoflakes having about 20  $\mu\text{m}$  length. The thickness of these self-assembled nanoflakes was measured to be around 250 nm. As shown in Figure 5.4, no change has occurred in the shape of nanoflakes on the surface after thermal treatment. However, the post-annealing process provides structural improvement as mentioned above.

To obtain detailed information about the elemental composition of the annealed film, EDS elemental mapping was also performed on the surface of D1. As shown in Figure 5.5, the image is given in the form of EDS maps for Cu-K (light green), Zn-K (dark green), S-K (red), Se-K (purple) and Sn-L (orange). As inferred from Figure 5.5, Cu, S, Se and Sn are distributed on the whole surface of CZTSSe film uniformly. There is no obvious contrast difference of their images. However, image of Zn-K has the regions with darker contrast. It means that this regions is Zn-poor. And, this regions of the CZTSSe film surface indicate the location of vertical nanoflakes.

In addition, STEM/EDS maps were generated to gain insights into the elemental composition of nanoflakes. For this purpose, the cross-section of the CZTSSe thin film was prepared by Focused Ion Beam (FIB). Before the preparation process, the surface of the film was coated with 20 nm thick Au layer to prevent from the possible FIB-induced damage. High-Angle Annular Dark Field (HAADF) images and elements distribution of the cross section of the CZTSSe thin film were given in Figure 5.6.

In Figure 5.6, it is seen that elements of Cu and Se are uniformly distributed throughout the cross-section of the film. And, distribution of S and Sn is also homogeneous except a thin of layer at the bottom of CZTSSe thin film. In contrast, when the distribution of Zn is examined, there is contrast difference obviously. The concentration of Zn is low in the upper parts of nanoflakes although is relatively high in the root regions of nanostructures.

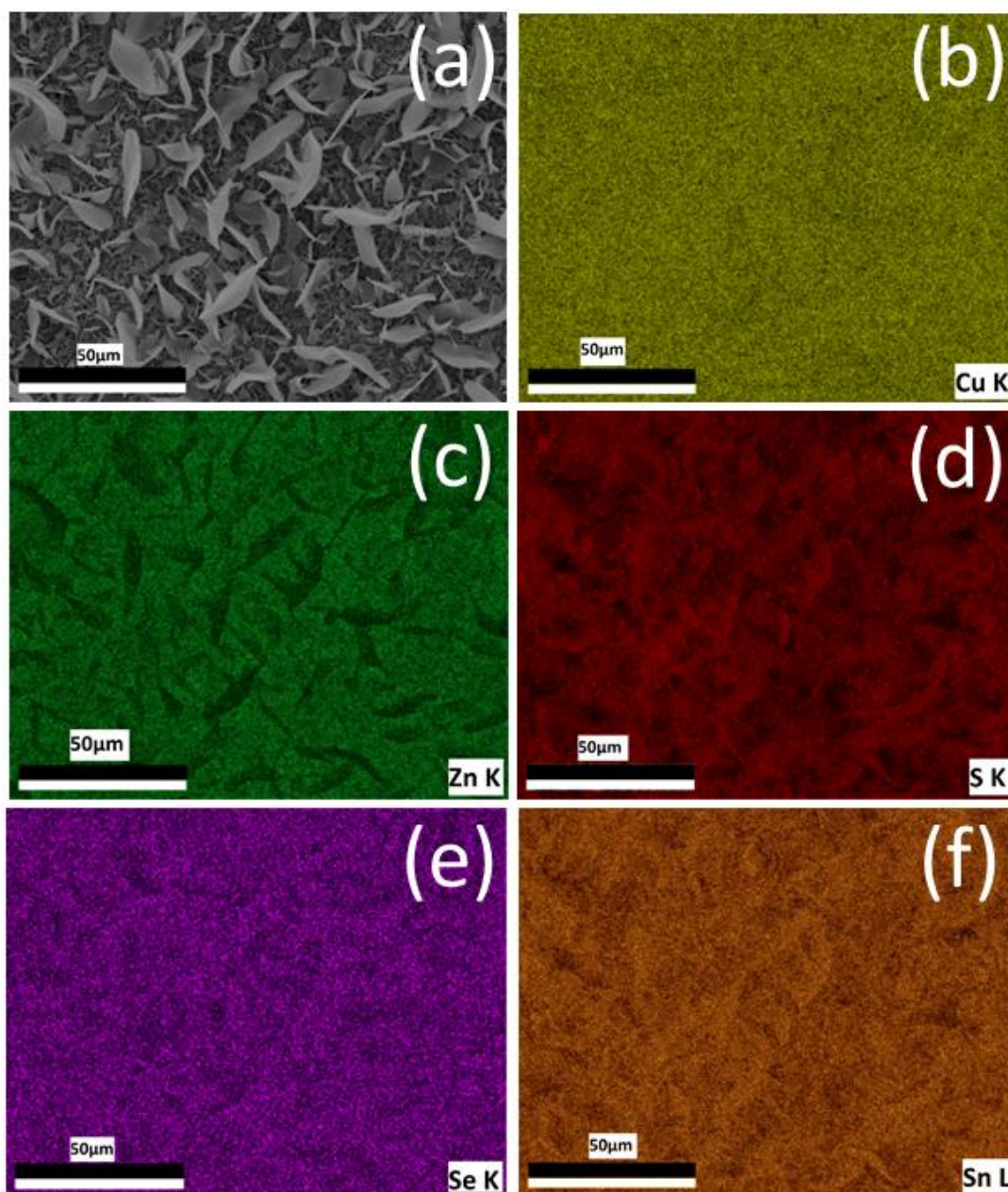


Figure 5.5. (a) SEM images of annealed sample surface of D1 and elemental EDS mapping of sample surface for (b) Cu, (c) Zn, (d) S, (e) Se and (f) Sn

In order to deeply comprehend the physical mechanism behind the formation of self-assembled nanostructures, each successive stacked layers starting from the first layer (ZnSe) were analyzed. For this purpose, ZnSe layer which was the first layer of the

intended 6 stacked layers, was deposited on SLG solely under the same conditions and surface of the film was investigated by SEM measurements.

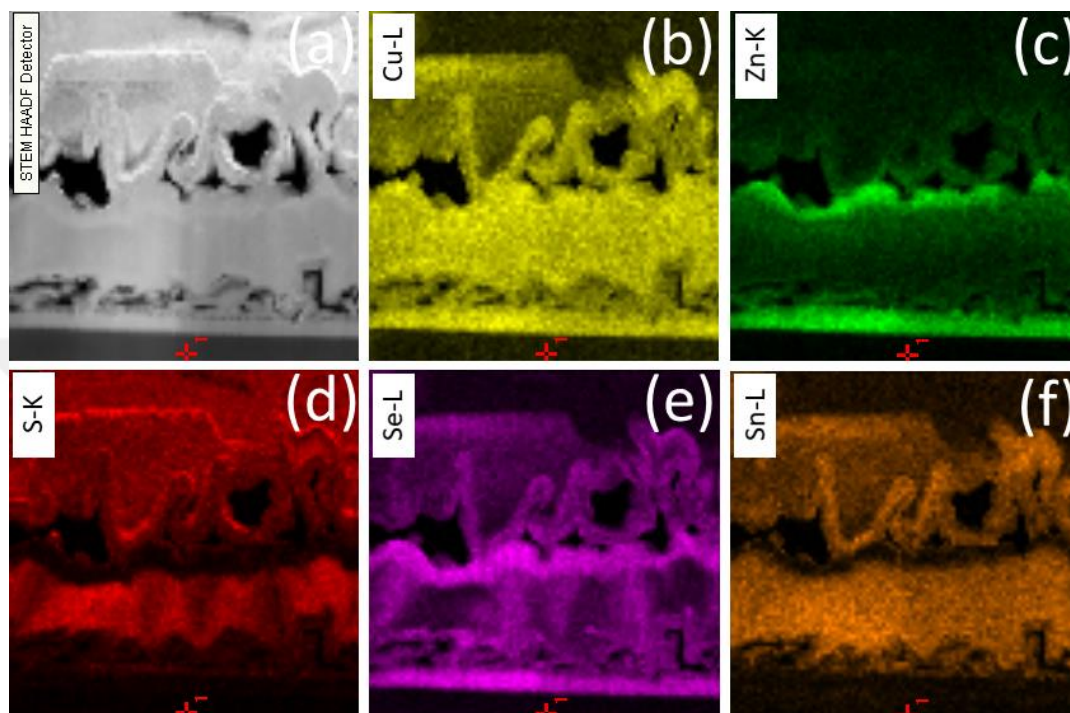


Figure 5.6. (a) High angle annular dark field STEM image of annealed film (D1); EDS mapping of (b) Cu, (c) Zn, (d) S, (e) Se and (f) Sn.

As seen Figure 5.7 (a), there is no trace for the formation of nanostructures and the surface of the film has the densely packed morphology. Secondly, ZnSe/CuSe stacked layers were deposited under the same deposition conditions. Figure 5.7 (b) shows the surface of film covered with the randomly distributed nanoflakes having a length of about  $2\mu\text{m}$ . The thickness of nanoflakes is also measured as about 30 nm from SEM measurement.

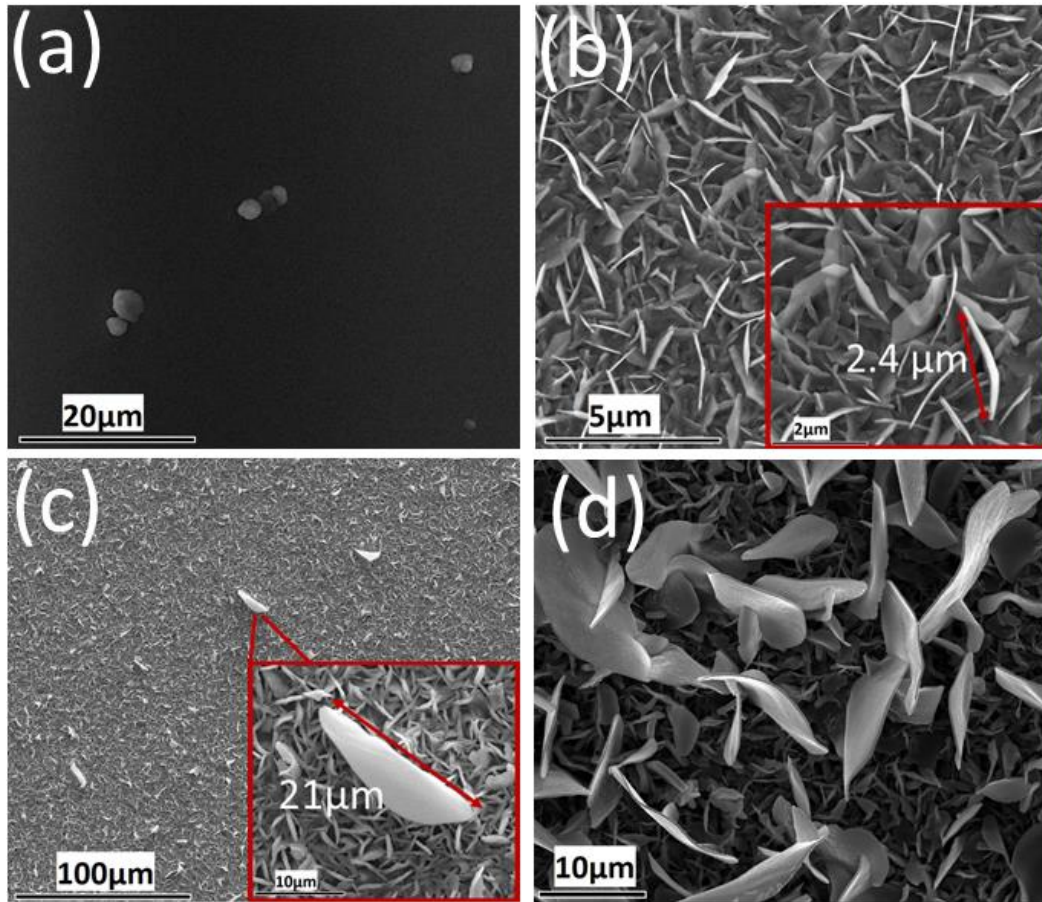


Figure 5.7. The evolution of the nanoflakes on the film surface; SEM micrographs after (a) ZnSe layer, (b) ZnSe/CuSe stacked layers, (c) ZnSe/CuSe/SnS stacked layers and (d) sixth layers depositions of D1

Then, ZnSe/CuSe/SnS stacked layers were deposited by keeping all conditions as the same, and it is observed that in some regions the length of the nanoflakes were reached to 20  $\mu\text{m}$  as seen in Figure 5.7 (c). Finally, when six stacked layers were produced; continuous grown and also uniform distribution of these 20  $\mu\text{m}$  nanoflakes was observed on the surface of the film (Figure 5.7 (d)). It can be deduced that the formation of nanoflakes is triggered at the interface of the deposited first and the second layers, that is, the nucleation for the nanoflake formation initiated on the surface of ZnSe film which is the first deposited layer. We hypothesize that Zn behaves like a catalyst related to self-oriented vertical nanoflakes and evolution of the

CZTSSe nanoflake is based on the presence of CuSe nanoflakes. CuSe may play an important role in the formation of vertical nanostructures since very thin randomly distributed nanoflakes on the film surface of ZnSe/CuSe stacked layers were observed. Figure 5.8 shows the SEM image of D2 samples and it is clearly seen that the size of self-assembled nanostructures is controlled by adjusting the thickness of the film. Although the uniformity of nanoflake formation was obtained on the surface of the film, the size of them was reduced with decreasing film thickness.

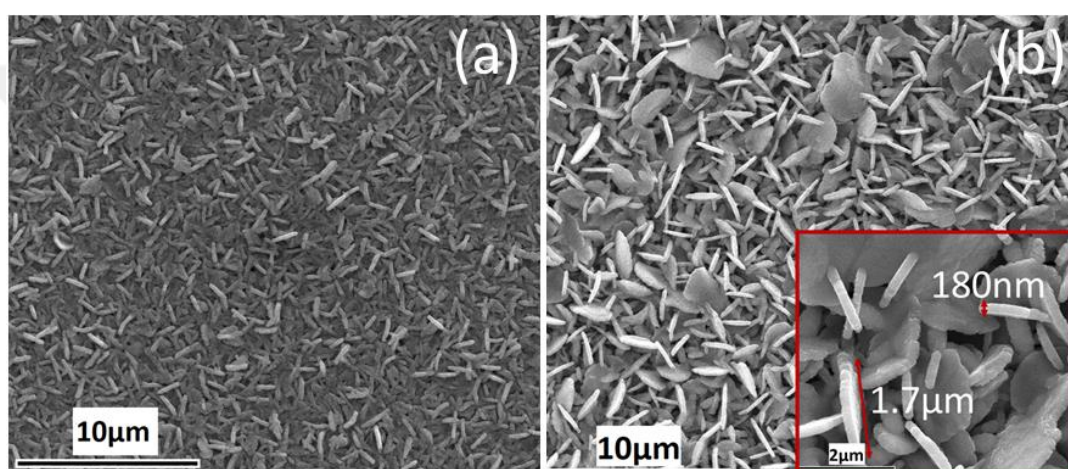


Figure 5.8. The top view SEM images of (a) as-deposited, (b) annealed sample of D2.

Reflection and transmission spectra of as-deposited and annealed (D1) CZTSSe films were given in Figure 5.9. It was observed that thin films having self-assembled nanoflakes located on the surface of the film have low reflectance and transmittance, which could be related with the naturally textured structure of CZTSSe thin film and also high absorption characteristic of this type of quaternary chalcopyrite structure. In addition, there seems to be an improvement in the surface reflection which leads the absorption of more light after the post-annealing treatment to both of the films, D1 and D2.

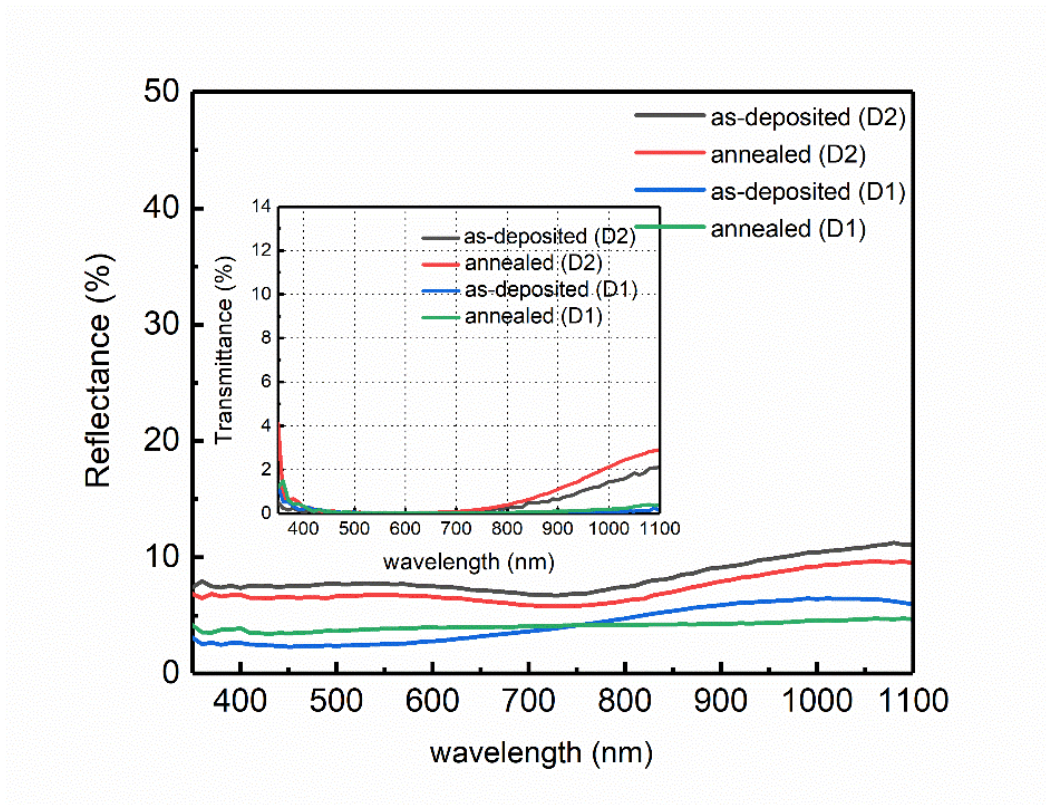


Figure 5.9. Reflectance and transmittance spectra of as-deposited and annealed samples of D1 and D2.

Figure 5.10 shows the peak of photoluminescence (PL) of annealed CZTSSe sample of D1 excited with 532 nm incident laser light at room temperature is at 1.25 eV, which is attributed to band to impurity level recombination at room temperature [128].

The electrical properties of the annealed film of D1 were examined by room temperature Hall-effect and temperature dependent conductivity measurements on the film layer deposited in van der Pauw geometry. The room temperature resistivity value was obtained as 2.2  $\Omega$ .cm according to the standard technique of four-contact van der Pauw method. As a result of Hall-effect measurement, CZTSSe film was found to have p-type semiconductor behavior. In addition, carrier concentration and mobility of the sample were obtained as  $1.8 \times 10^{17} \text{ cm}^{-3}$  and  $1.4 \times 10^1 \text{ cm}^2/\text{V.s}$ , respectively. The temperature variations of the dark conductivity ( $\sigma$ ) were shown in Figure 5.11.

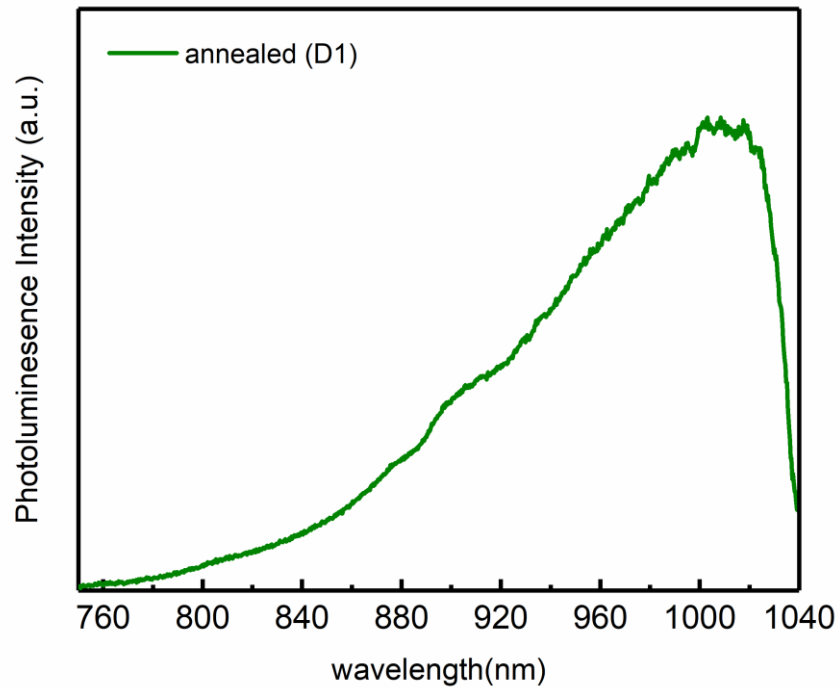


Figure 5.10. PL spectrum of annealed CZTSSe film of D1 at room temperature.

This conductivity profile of CZTSSe thin film indicates Arrhenius behavior which is an increasing exponential variation with increasing temperature. Observed temperature dependent behavior was modeled according to the Eqn 4.3. In this analysis, the activation energies,  $E_a$ , were calculated as 0.2 meV, 3 meV and 14 meV using the relation between  $\ln(\sigma)$  and  $1000/T$  for three different temperature regions as 100-150 K, 160-240 K, 250-340 K for which the variations are linear. This is attributed to the existence of possible shallow trap centers in the structure. And, the conductivity variations under different illumination intensities show almost same behavior with an increase in the conductivity values at each temperature as expected.

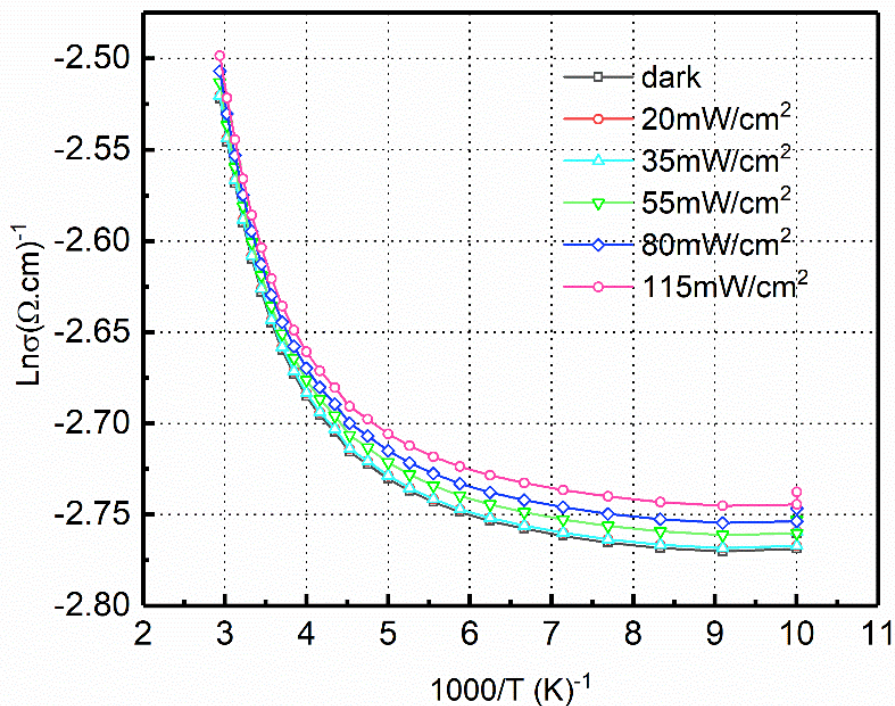


Figure 5.11. Temperature dependent electrical conductivity of annealed CZTSSe film of D1 under dark and illumination.

### 5.3.2. Effect of Substrate Temperature on the Formation of Nanoflakes

In order to investigate the influence of the deposition temperature on the CZTSSe thin film structure with nanoflakes, the depositions were carried out under the same growth conditions except for the deposition temperature which were kept at 100°C and 200°C for the samples D3 and D4, respectively.

For these films, XRD measurements and Raman scattering measurements indicate the formation of quaternary CZTSSe structure with the post annealing treatment as seen in Figure 5.12 and 5.13. According to the EDS analyses results listed in Table 5.3, the as-deposited D3 sample has Se rich composition as compared to D1; however,

expected stoichiometric composition is obtained with the post-annealing treatment on this sample.

On the other hand, D4 sample showed relative concentration of elements closer to D1, and it was observed that there is no significant effect of post-heating on these ratios.

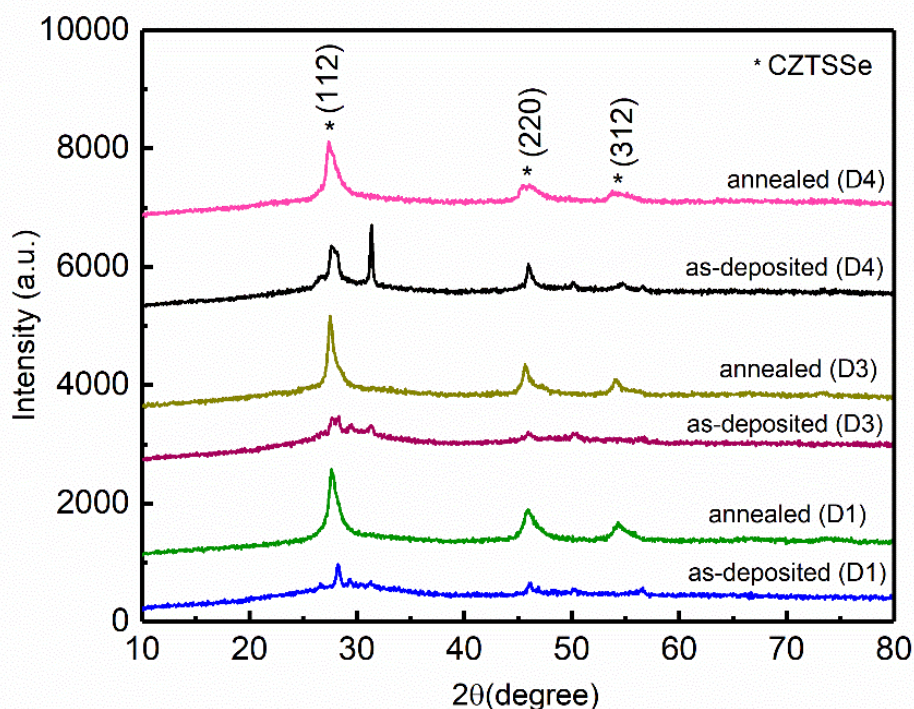


Figure 5.12. XRD patterns of D1, D2, D3 and D4 samples.

Moreover, as shown in the SEM image of both of these films (Figure 5.14), the decrease in the substrate temperature affects the formation of nanoflakes on the surface of the films. Although there are continuous distribution of nano-platelet array on the surface of D3 samples, they are not found as in the D1 samples in which these nanostructures were grown vertical to the surface.

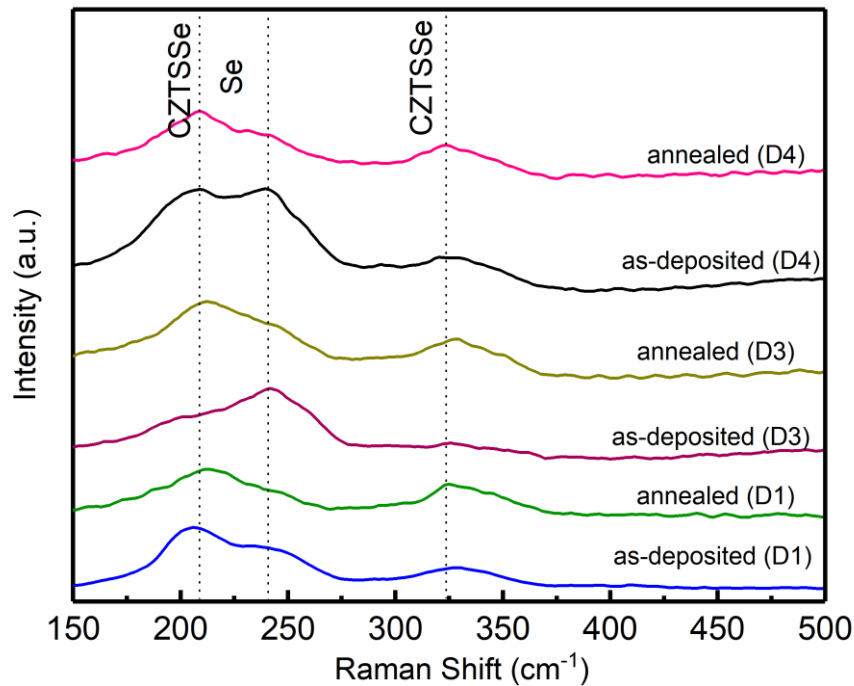


Figure 5.13. Raman spectra of D1, D2, D3 and D4 samples.

On the other hand, the surface of the as-deposited D4 sample has compact and densely packed morphology without any nanostructure. After the post-annealing, even if the nucleation for the nanoflakes was started, buckling formation due to stress relaxation of the thin film in some areas was become dominant in the surface characteristic of these films as seen in Figure 5.14 (d). In the optical characterization step, reflectance measurements of the as-deposited and annealed films fabricated at different temperatures were performed in the range of 350-1100 nm. Similar to the D1 sample, optical results indicate that these CZTSSe thin films in as-deposited and annealed forms have low reflectance values, as shown in Figure 5.15. However, the best result was obtained from the D1 samples, which is the strong effect of vertical nanoflakes.

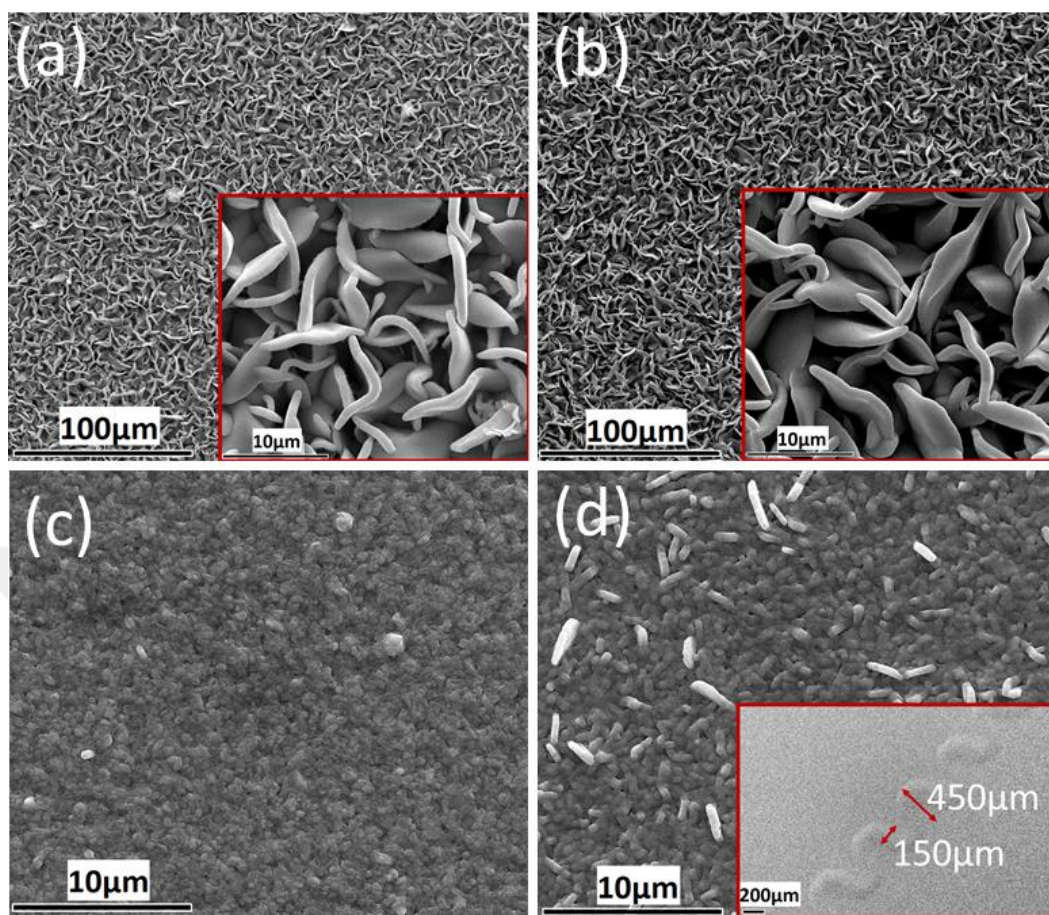


Figure 5.14. The top view SEM micrographs of (a) as-deposited, (b) annealed films of D3, (c) as-deposited, (d) annealed films of D4.

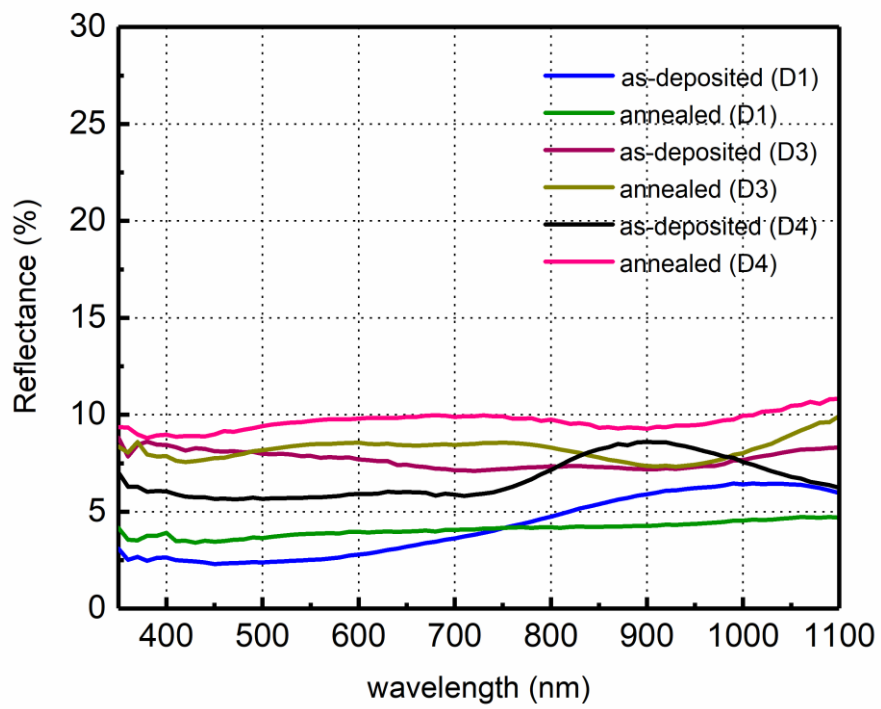


Figure 5.15. Reflectance versus wavelength plot of D1, D3 and D4 samples.

## CHAPTER 6

### CZTSSE THIN FILMS FABRICATED BY SINGLE STEP DEPOSITION FOR SUPERSTRATE SOLAR CELL APPLICATIONS

#### 6.1. Introduction

The focus of this study is the characterization of CZTSSe thin films deposited by RF magnetron sputtering as one step process and fabrication of CZTSSe solar cell in superstrate configuration. In this study, CZTSSe absorber layer was grown by RF magnetron sputtering technique using stacked layer procedure. SnS, CuSe and ZnSe solid targets were used as precursors and no additional step like the selenization process was applied. Firstly, deposited film quality was investigated. Following the characterization of deposited CZTSSe thin films, superstrate-type configuration of glass/ITO/CdS/CZTSSe/metal was entirely fabricated by totally vacuum-based processes. Then, device characterization of this structure was carried out.

As a next step, structure of glass/FTO/TiO<sub>2</sub>/CdS/CZTSSe/metal structure was prepared. For this purpose, titanium dioxide (TiO<sub>2</sub>) was coated on top of FTO layer to enhance the power conversion efficiency of CZTSSe solar cell in superstrate configuration due to its being a hole blocking and wide band gap material. The thickness effect of TiO<sub>2</sub> layer was analyzed by applying 3 different thickness values of 20, 50 and 90 nm and the optimum thickness of TiO<sub>2</sub> layer was determined. Furthermore, the effect of different contact materials on the device performance was examined. As a result, the glass/FTO/TiO<sub>2</sub>/CdS/CZTSSe/Au structure showed the best cell performance and the main solar cell parameters were found as  $V_{oc}$ : 185mV,  $J_{sc}$ : 2.54mA/cm<sup>2</sup> and FF: 25% and  $\eta$ : 0.12%.

## 6.2. Experimental Procedure

This study consists of two parts. In the first part of this study, CZTSSe based solar cells were prepared in superstrate-type architecture utilizing indium tin oxide (ITO) coated glass substrates with the sheet resistivity of  $10\Omega/\text{sq}$ . Before the cadmium sulfide (CdS) deposition, ITO coated glass substrates were subjected to a sequence of ultrasonic cleaning steps (acetone, isopropanol and DI water for 10 min. each) and UV ozone treatment. Subsequently, samples were dried in  $\text{N}_2$  atmosphere. CdS layers were deposited on ITO coated glass substrates at room temperature using thermal evaporation with CdS (99.99%) powder as the source material. The base pressure of the evaporation chamber was about  $5 \times 10^{-6}$  Torr during the deposition and the thickness of CdS layers was about 100nm. Then, SnS, CuSe and ZnSe precursor layers were deposited on both glass substrate and CdS/ITO/glass using RF magnetron sputtering technique. CZTSSe/glass samples were used for the material characterization of deposited CZTSSe films. The RF power applied for SnS (99.99%), CuSe (99.99%) and ZnSe (99.99%) targets was 80 W in a typical sputtering run. The optimized deposition order was determined as SnS (150 nm)/CuSe (300 nm)/ZnSe (150 nm)/SnS (150 nm)/CuSe (300 nm)/ZnSe (150 nm)/SnS (100 nm) stacked layers in order to eliminate the metallic behavior on the top surface of film and to provide the adhesion of thin film on ITO coated glass as given in Figure 6.1.

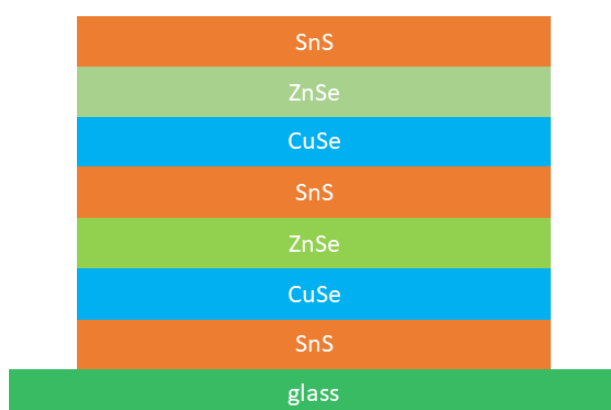


Figure 6.1. The schematic presentation of precursor sequence.

The substrate temperature was kept at 150°C and the chamber pressure was nearly  $6 \times 10^{-3}$  Torr during the deposition of precursors under 6 sccm Ar flow. After the deposition process, samples were subjected to post-annealing at 350°C under N<sub>2</sub> atmosphere for 30 min. Then, Au was thermally evaporated as a back contact using Cu hard masks with dots of 500 μm radius.

In the second part of this study, to enhance the performance of superstrate type solar cell, TiO<sub>2</sub> layer was deposited by spin coating method on FTO coated glass substrate using the spinning rates of 1500 rpm 6 sec and 3000 rpm 20 sec sequentially and annealed at 500°C for 30 min. Then, samples were cooled and immersed in 45 mM TiCl<sub>4</sub> solution for 45 min at 70°C and annealed at 500°C for 30 min again. The flow diagram of solar cell fabrication was given in Figure 6.2. In addition, 3 different metals were used as back contact layer to determine the suitable material. For this, Ag-Au, Cr-Au alloys and pure Au contact were deposited by thermal evaporation method.

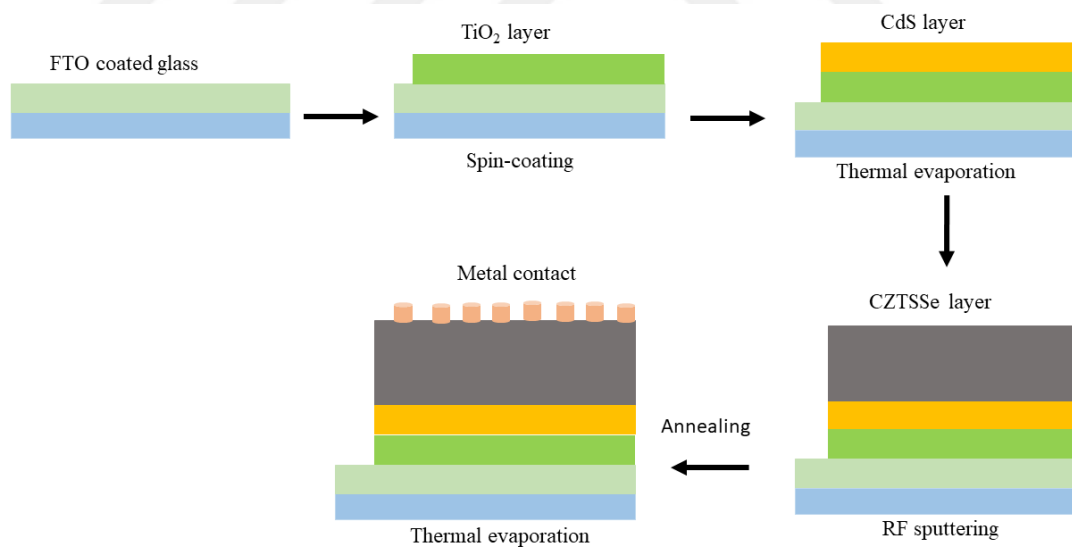


Figure 6.2. Flow diagram of solar cell fabrication in superstrate configuration.

To investigate the morphological and compositional properties of deposited films, Quanta 400 FEG model scanning electron microscopy (SEM) equipped with energy dispersive X-ray spectroscopy analysis (EDS) system were used. The X-ray diffraction (XRD) measurements were performed using a Rigaku Miniflex XRD system equipped with a CuK $\alpha$  radiation source. Raman scattering measurements were carried out by using a Horiba-Jobin Yvon iHR550 imaging spectrometer with the three-grating monochromators and a laser with the wavelength of 532 nm used as an excitation source. Dektak 6M profilometer was used to measure the thickness of thin film layer. The optical characterization of the CZTSSe thin film on glass substrate was performed by Perkin-Elmer Lambda 45 spectrophotometer. Hall-effect measurement was carried out to determine the electrical properties of the film by using Nanomagnetic Hall Effect system at a magnetic field strength of 0.9 T. In addition, temperature dependent conductivity measurements in the temperature range of 100-340 K were performed by using different illumination intensity in between 20 and 115 mW/cm<sup>2</sup> with the help of a Janis liquid nitrogen cryostat and Lake-Shore 331 temperature controller. External quantum efficiency (EQE) measurement of the CZTSSe solar cell were carried out by Bentham PVE 300 system. The current-voltage characteristics of the device were measured using computer controlled Keithley 2400 sourcemeter under dark and illumination of an AM 1.5 global spectrum.

### **6.3. Results and Discussion**

#### **6.3.1. Structural, Optical and Electrical Properties of the Absorber Layer**

The chemical composition of the absorber film layer was determined by EDS analysis and the obtained spectrum showed characteristic peaks associated with the constituent elements without any impurity content. The relative atomic percentage of the elements in the deposited thin film was found as Cu:Zn:Sn:S:Se= 20:11:18:25:26 %, which

indicates that absorber layer has in Sn-rich behavior. The crystalline nature of this film layer was investigated performing XRD and Raman scattering measurements. The XRD profile of the CZTSSe thin film was given in Figure 6.3. In this figure, three diffraction peaks around angles of 27.9, 46.1 and 54.6 were observed and these reflections of X-rays were associated with the crystalline orientations in the plane directions of (112), (220) and (312) in a good agreement with kesterite CZTSSe structure, respectively (ICDD data #00-052-0868 CZTSe and ICDD data#00-026-0575 CZTS). The Miller indices associated with peaks were also given in the figure. XRD pattern of CdS layer was also given in the inset of Figure 6.3 (a). It has polycrystalline structure and the predominant diffraction peak at  $2\theta = 26.2^\circ$  was indexed as (111) plane, corresponding to the hexagonal wurtzite phase of CdS.

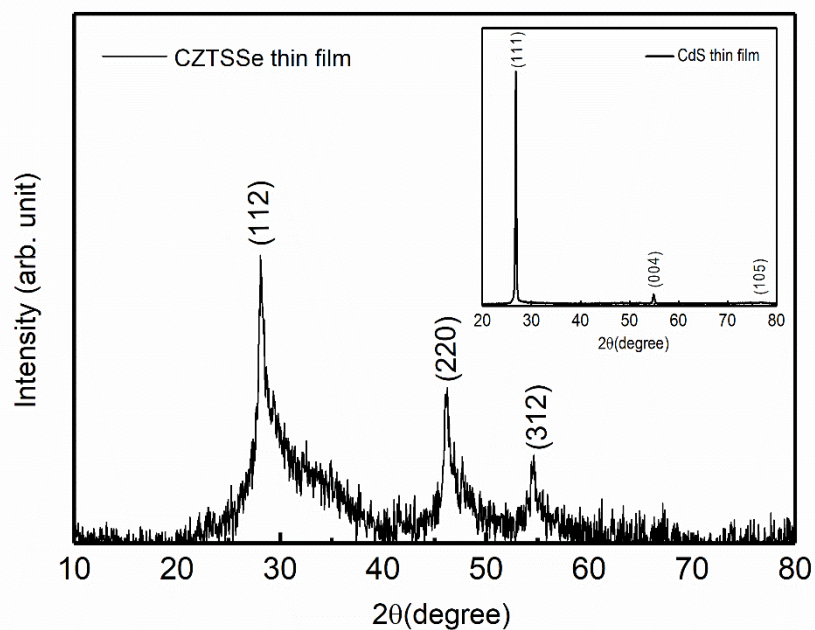


Figure 6.3. The XRD pattern of CZTSSe layer. The inset shows the XRD pattern of CdS layer.

The crystalline phase identification and the existence of possible secondary phases in the CZTSSe structure was performed by Raman scattering measurements. As shown in Figure 6.4, the detected peaks at 198  $\text{cm}^{-1}$  and 328  $\text{cm}^{-1}$  could be evaluated as being  $A_1$  mode frequencies of the CZTSSe structure. The shift of  $A_1$  vibration modes is observed in the Raman spectrum of CZTSSe structure due to the substitution of S by Se [129]. The additional Raman peak found at 240  $\text{cm}^{-1}$  is well-matched with the elementary Se contribution to the structure [127], [130], [131].

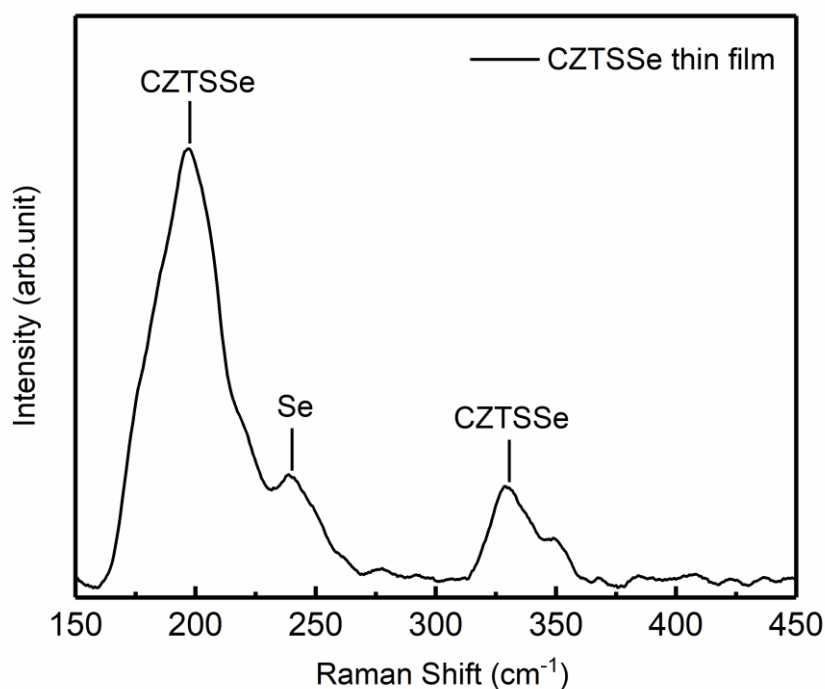


Figure 6.4. Raman spectrum of CZTSSe layer.

On the other hand, there is no another Raman peak originated by binary or ternary phases in the deposited CZTSSe film. The surface morphology of the CZTSSe thin film was observed utilizing SEM measurement. The obtained top-view SEM image of the sample surface indicates a series of close-packed CZTSSe grains without any void

on the surface of the film (Figure 6.5). This result can be the indication of well-deposited film surface that positively affects getting solar cell having better device parameters. The optical characteristics of the film layer were investigated by transmittance ( $T$ ) and reflectance ( $R$ ) measurements performed at room temperature. In the region of interest for photovoltaic applications, the film showed a very low optical transmittance below 5% and a reflectance of about 15% as presented in Figure 6.6. Based on these experimental results, the absorption coefficient ( $\alpha$ ) values were calculated by using the Eqn 4.1. The  $\alpha$  values were found above  $10^4 \text{ cm}^{-1}$  in the visible and near-IR region which are in a good agreement with the properties of the CZTSSe absorber films reported in the literature [17].

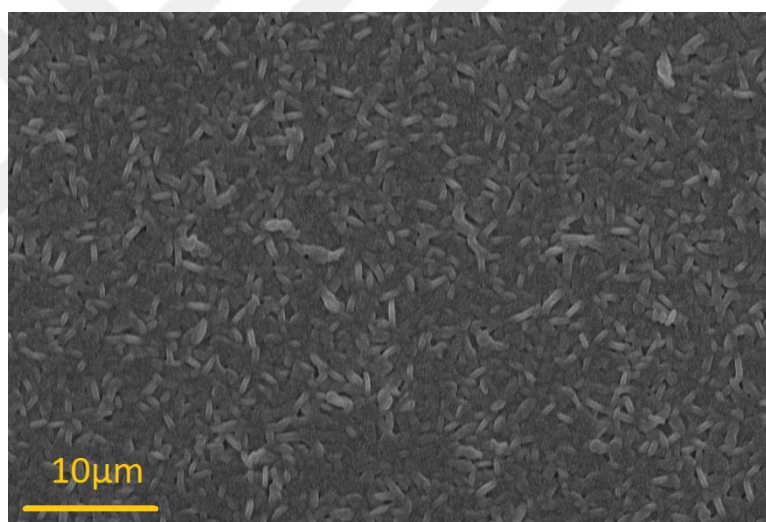


Figure 6.5. The SEM surface image of CZTSSe thin film.

According to the direct optical transition behavior, the optical band gap of the film was calculated by Tauc relation (Eqn 4.2). In the Tauc plot given in Figure 6.7,  $E_g$  value was found by extrapolating the linear part to the energy axis. As a result of linear fitting process, the gap value was determined as about 1.43eV, which is well-consistent with the reported values for CZTSSe [17], [132]. Furthermore, the direct

band gap value of the CdS layer was found to be 2.42 eV given in the inset of Figure 6.7.

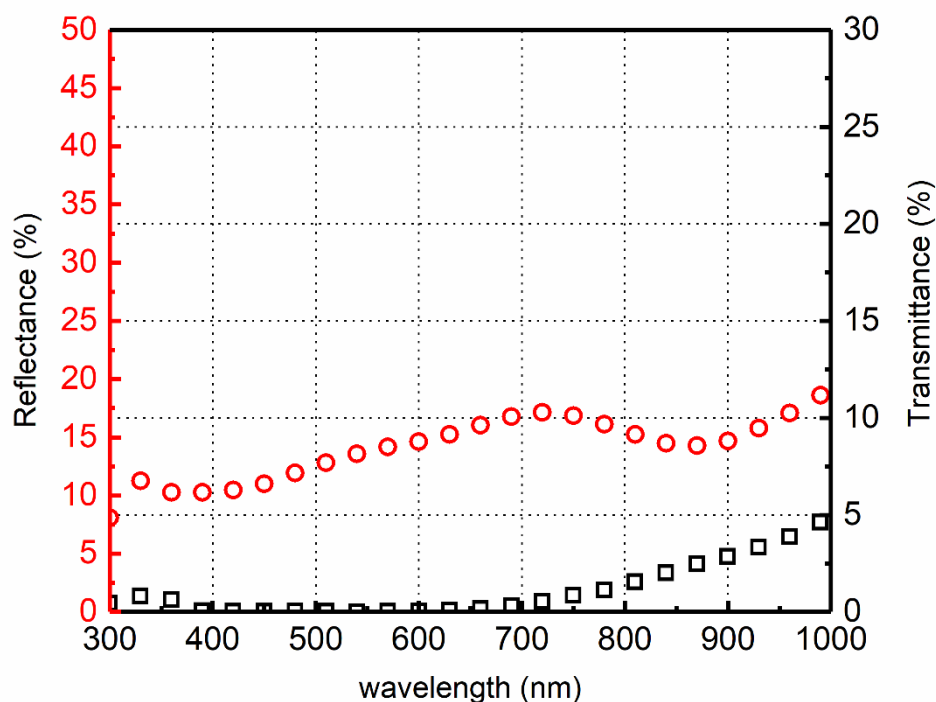


Figure 6.6. The plot of reflectance and transmittance of CZTSSe layer as a function of wavelength.

The electrical properties of the CZTSSe thin film structure were investigated by room temperature Hall-effect and temperature dependent conductivity measurements on the film layer deposited in Van der Pauw geometry and prepared with Au front metal contact evaporation through suitable contact geometry. The room temperature resistivity value was extracted as  $0.57 \Omega \cdot \text{cm}$  according to the standard technique of four-contact van der Pauw method. As a result of Hall-effect measurement, CZTSSe film was found in p-type semiconductor behavior from the sign of Hall voltage. In addition, carrier concentration and mobility of the sample were obtained as  $3.93 \times 10^{18} \text{ cm}^{-3}$  and  $2.77 \text{ cm}^2/\text{V} \cdot \text{s}$ , respectively.

The temperature variations in the dark conductivity ( $\sigma$ ) values are shown in Figure 6.8. This conductivity profile of CZTSSe thin film indicates Arrhenius behavior which is an increasing exponential variation with increasing temperature.

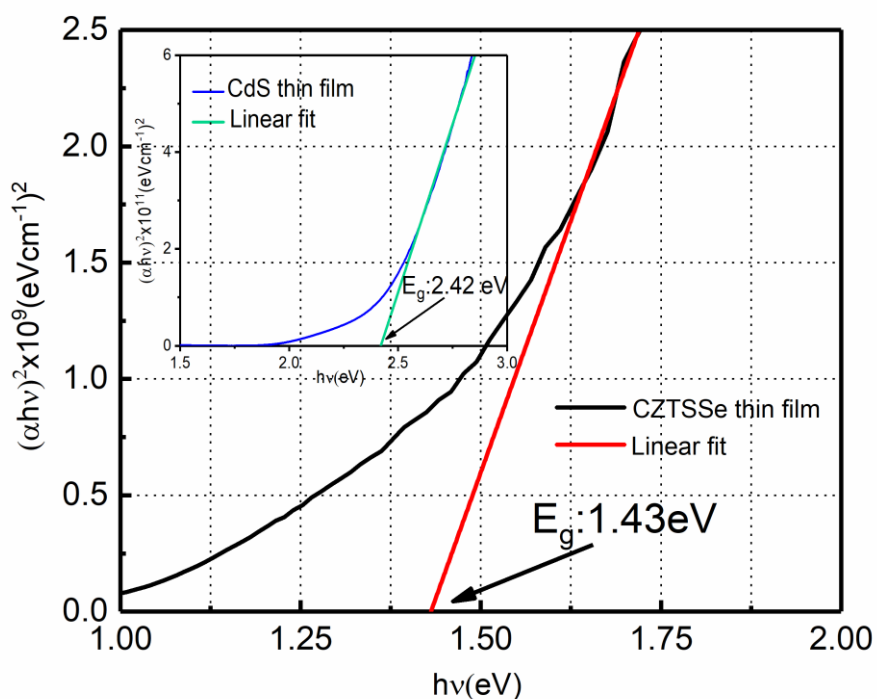


Figure 6.7.  $(\alpha hv)^2$  vs  $h\nu$  graph for CZTSSe thin film. Inset shows the  $(\alpha hv)^2$  vs  $h\nu$  graph for CdS layer.

This observed temperature dependent behavior was modeled according to the Eqn 4.3. In this analysis, the activation energies were calculated from the relation between  $\ln(\sigma)$  and  $1000/T$  and three linear regions with  $E_a$  values of 9.7 meV for 250-340 K, 2.8 meV for 150-200 K and 0.7 meV for 100-140K regions were obtained as inferred from the linear lines in the inset of Figure 6.8. These energy values can be related to the existence of possible shallow trap centers in the structure that can take part in the conduction process at specific temperature intervals [133], [134]. In addition, the

photoconductivity values were observed higher than the values in dark condition at each illumination intensity and temperature step due to the current contribution of excited carriers under illumination. As given in Figure 6.8, it was found that, at each temperature, the conductivity with the photo-excited carriers are directly proportional to the illumination intensity and at each illumination, contribution to the conductivity also increases exponentially with increase in temperature [135].

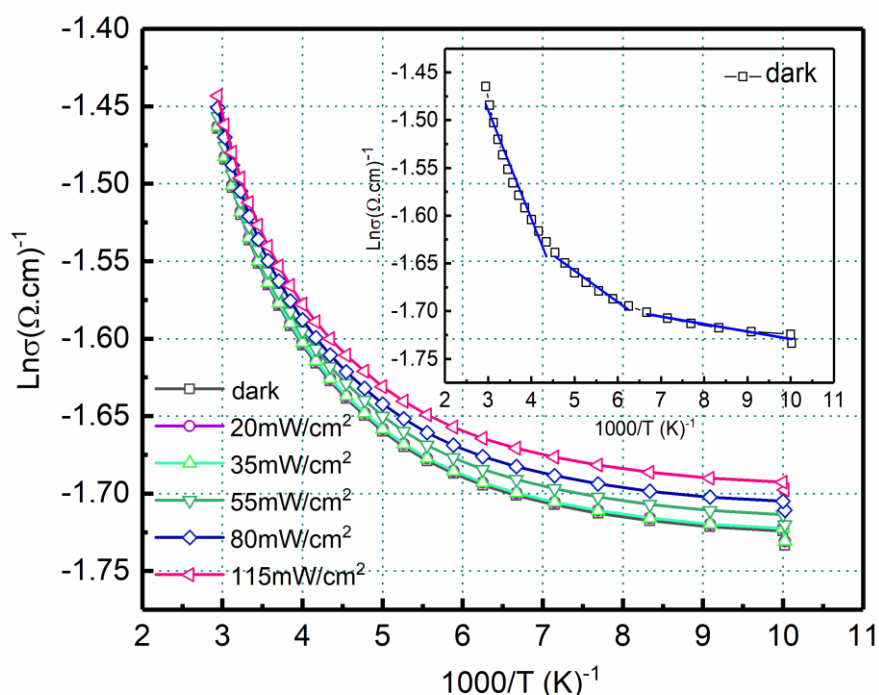


Figure 6.8. Temperature dependent dark and illuminated conductivity behavior of CZTSSe thin film. Inset shows the variation of dark conductivity.

### 6.3.2. Photovoltaic Properties of SLG/ITO/CZTSSe/CdS/Au Superstrate Structure

The photovoltaic performance of CZTSSe based solar cell in superstrate configuration was evaluated under irradiation of AM 1.5. The current-voltage curves under dark and illumination are given in Figure 6.9. This configuration could be illuminated from

either side. Illumination of the solar cell from the glass was labeled as primary illumination while illumination from back side of the solar cell was labeled as the secondary illumination. The main solar cell parameters were obtained from the primary illumination. The power conversion efficiency was 0.05% with a short-circuit density ( $J_{sc}$ ) of  $2.45 \text{ mA}\cdot\text{cm}^{-2}$ , open circuit voltage ( $V_{oc}$ ) of 77mV and fill factor (FF) of 25%.  $V_{oc}$  value is much lower than of superstrate type kesterite solar cells in the literature

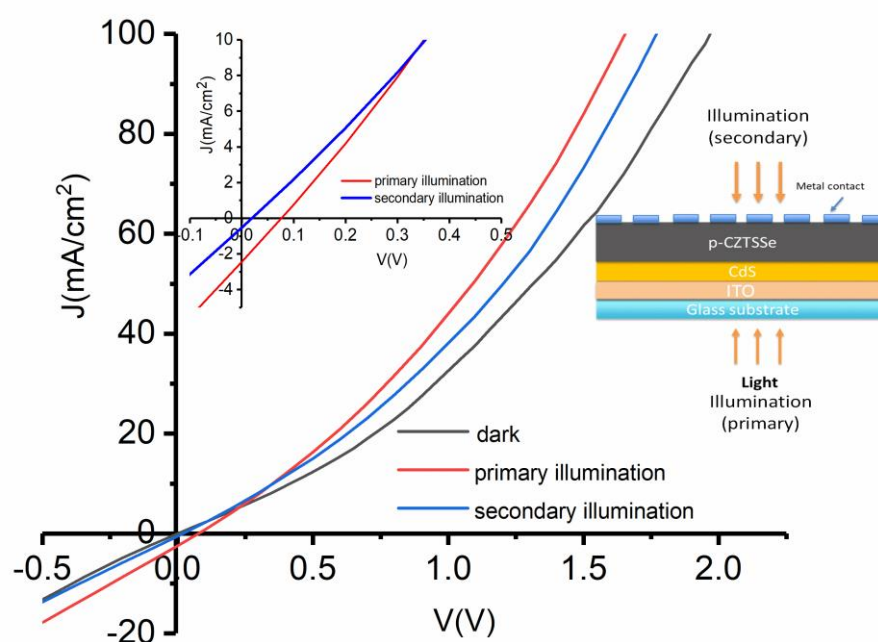


Figure 6.9. J-V graph for ITO/CdS/CZTSSe/Au solar cell under dark and illumination. Inset shows the J-V graph of the solar cell at the voltage range of 0 and 0.5 V.

Under illumination, the series resistance ( $R_s$ ) and shunt resistance ( $R_{sh}$ ) were found as  $16 \Omega\cdot\text{cm}^2$  and  $101 \Omega\cdot\text{cm}^2$ , respectively. The series resistance value is much higher

than the obtained value in the literature [49], [53], [57]. The key limiting factor in the efficiency of the CZTSSe solar cell is high  $R_s$  and low  $V_{oc}$  values, which were attributed to the poor quality of the film, interface recombination and some contact problems [136]. In addition, low-response to illumination was observed when the solar cell was illuminated from the contact side (secondary illumination), as observed from Figure 6.9.

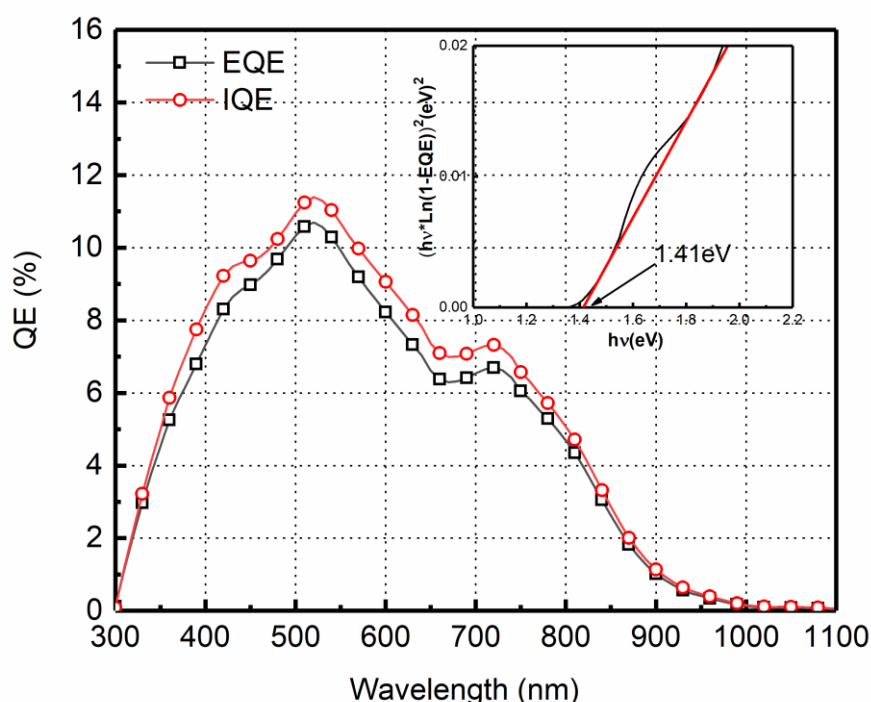


Figure 6.10. External quantum efficiency (EQE) spectrum of ITO/CdS/CZTSSe/Au structure. The inset shows the  $[hv \cdot \ln(1 - EQE)]^2$  vs  $h\nu$  plot of CZTSSe layer.

The external quantum efficiency (EQE) of CZTSSe solar cell as a function of wavelength was measured and the result is given in Figure 6.10. Moreover, internal quantum efficiency was calculated by using the following expression,

$$IQE = \frac{EQE}{1 - R} \quad (6.1)$$

The maximum value of EQE was found as 11% almost at 500 nm which could be attributed to optical absorption of CdS. Then, the signals decayed abruptly.

The short circuit current ( $J_{sc}$ ) was calculated  $2.3 \text{ mA/cm}^{-2}$  from the external quantum efficiency measurement, which is in good agreement with the value of  $J_{sc}$  obtained from the current-voltage measurement. In addition, the extrapolation to zero of linear fitting in the plot of  $[\text{hv} \cdot \ln(1 - \text{EQE})]^2$  versus  $\text{hv}$  gives the band gap energy of CZTSSe at 1.41 eV (inset of Figure 6.10).

### **6.3.3. The Effect of TiO<sub>2</sub> Layer on the Device Performance of CZTSSe Superstrate Structure**

In this section, TiO<sub>2</sub> layer was used in the superstrate-type configuration of glass/FTO/TiO<sub>2</sub>/CdS/CZTSSe/Ag-Au due to its hole blocking layer and wide band gap material. For this purpose, the thickness effect of TiO<sub>2</sub> layer was analyzed by applying 3 different thickness values of 20, 50 and 90 nm nearly.

#### **6.3.3.1. Physical Properties of TiO<sub>2</sub> Layer**

TiO<sub>2</sub> layer was deposited on FTO substrate by using spin coating technique. The XRD patterns of TiO<sub>2</sub> thin films showed the polycrystalline structure which indicates anatase phase of TiO<sub>2</sub> as given in Figure 6.11. The peaks from the FTO substrate were also marked in the XRD pattern.

The top-view SEM image of spin coated TiO<sub>2</sub> layer was given in Figure 6.12. SEM image shows that TiO<sub>2</sub> film has dense surface morphology covering complete surface area.

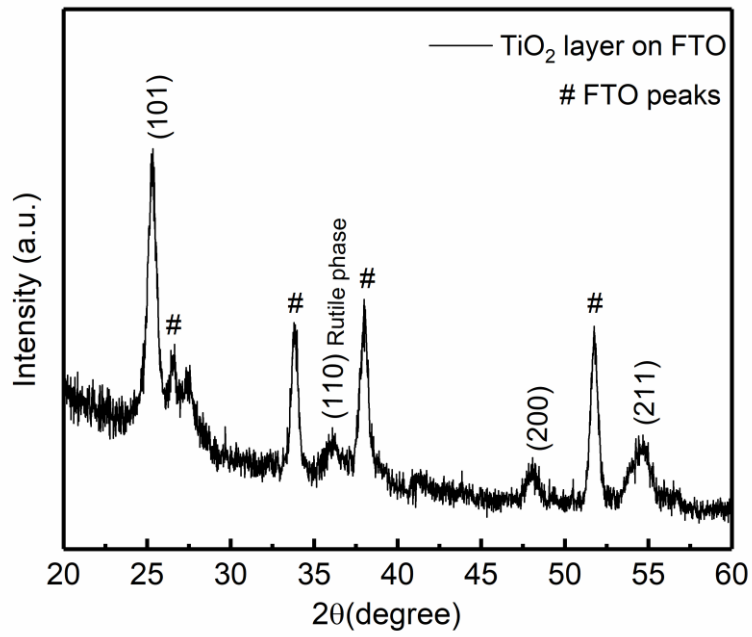


Figure 6.11. XRD results of anatase  $\text{TiO}_2$  layer (90 nm) on FTO substrate.

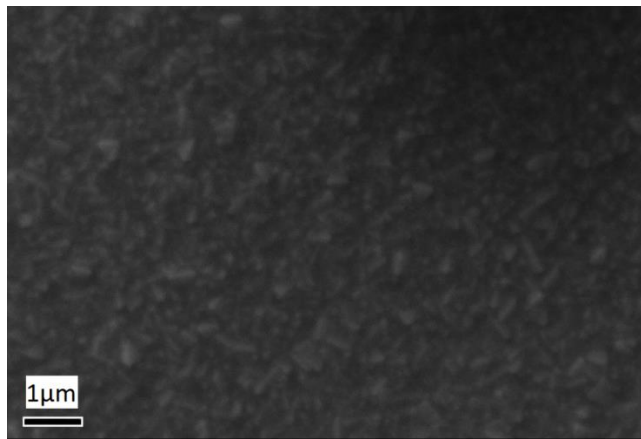


Figure 6.12. Top view SEM image of the  $\text{TiO}_2$  thin film with a thickness of 90 nm.

In addition, the transmission spectra of TiO<sub>2</sub> films with different thickness in the wavelength region of 350-1150 nm were given in Figure 6.12. It was observed that there is high transmittance values of films around 80-90% in the visible region.

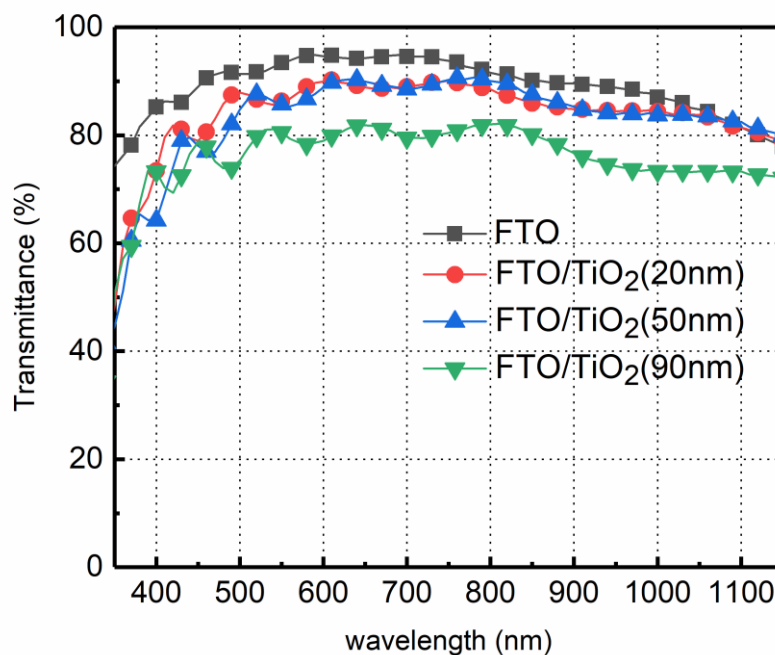


Figure 6.13. Transmission spectra of TiO<sub>2</sub> films with different thickness on FTO substrate.

### 6.3.3.2. The Effect of TiO<sub>2</sub> Thickness on Device Performance

The photovoltaic performance of SLG/FTO/TiO<sub>2</sub>/CdS/CZTSSe/Ag-Au structure was evaluated under irradiation of AM 1.5. The current-voltage curves of solar cells having different TiO<sub>2</sub> thickness in dark and under illumination were given in Figure 6.14. In addition, power conversion efficiency, short-circuit density ( $J_{sc}$ ), open circuit voltage ( $V_{oc}$ ), fill factor (FF), series resistance ( $R_s$ ) and shunt resistance ( $R_{sh}$ ) values of devices were given in Table 6.1. The positive effect of TiO<sub>2</sub> layer on the open circuit voltage was observed when compared to the case without TiO<sub>2</sub> layer. When the thickness of TiO<sub>2</sub> layer in superstrate structure increases, the increase in  $V_{oc}$  was observed.

However, the obtained high series resistance values when compared to reported values in the literature are attributed to the quality of film, interface recombination and the contact problems [136].

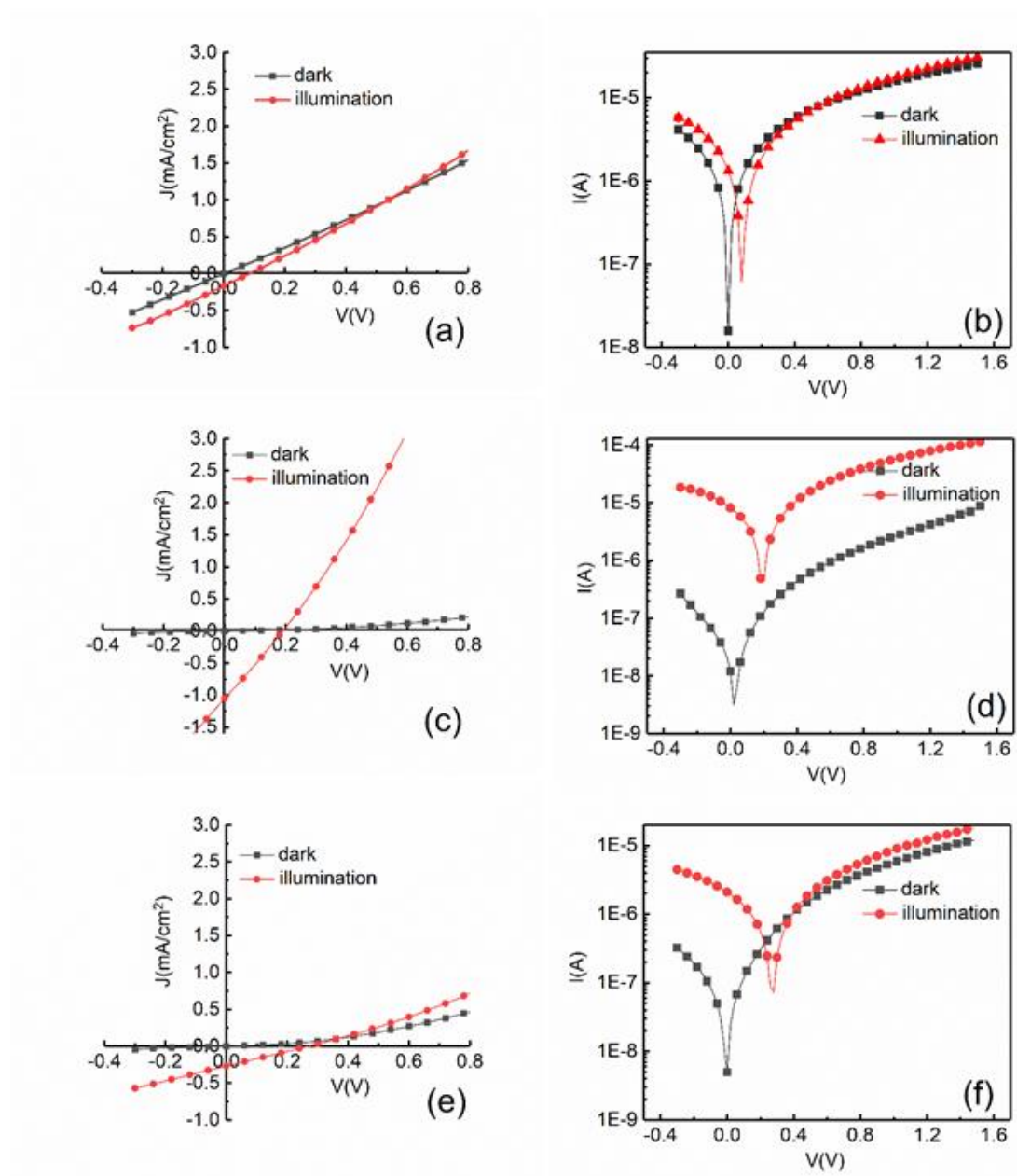


Figure 6.14. TiO<sub>2</sub> thickness dependence of J-V and I-V plots as linear and semi-logarithmic scales of SLG/FTO/TiO<sub>2</sub>/CdS/CZTSSe/Ag-Au structure in dark and under illumination. Thickness of TiO<sub>2</sub> layer is (a), (b) 20 nm; (c), (d) 50 nm; (e), (f) 90 nm.

Table 6.1. Solar cell parameters of SLG/FTO/CdS/CZTSSe/Ag-Au structure extracted from I-V curves under illumination

Samples	$TiO_2$ (20 nm)	$TiO_2$ (50 nm)	$TiO_2$ (90 nm)
$V_{oc}$ (mV)	80	190	280
$J_{sc}$ (mA/cm <sup>2</sup> )	0.17	1.05	0.27
FF (%)	26	26	25
$\eta$ (%)	0.003	0.050	0.020
$R_s$ ( $\Omega$ .cm <sup>2</sup> )	200	50	250
$R_{sh}$ ( $\Omega$ .cm <sup>2</sup> )	540	230	970

### 6.3.3.3. The Effect of Different Contact Materials on CZTSSe Superstrate Solar Cells

In this part of the study, the thickness of  $TiO_2$  layer of superstrate structure was set to about 90 nm since the best  $V_{oc}$  value was obtained under this conditions. And, the effect of contact materials on the device performance was investigated.

In first case, Au metal contact was thermally evaporated on SLG/FTO/ $TiO_2$ /CdS/CZTSSe as metal contact. In the second case, Cr-Au alloy was used as the metal contact for CZTSSe solar cells for which Cr was deposited by e-beam evaporation and Au was thermally evaporated on SLG/FTO/ $TiO_2$ /CdS/CZTSSe. Figure 6.15 shows the results of J-V and I-V measurement of SLG/FTO/ $TiO_2$ /CdS/CZTSSe/Au and SLG/FTO/ $TiO_2$ /CdS/CZTSSe/Cr-Au structures as linear and semi-logarithmic plots in dark and under illumination.

The best conversion efficiency was attained for SLG/FTO/ $TiO_2$ /CdS/CZTSSe/Au configuration as 0.1 % with a short-circuit density ( $J_{sc}$ ) of 2.54 mA.cm<sup>-2</sup>, open circuit voltage ( $V_{oc}$ ) of 185 mV and fill factor (FF) of 24 %. Series resistance ( $R_s$ ) and shunt resistance ( $R_{sh}$ ) values were found as 25  $\Omega$ .cm<sup>2</sup> and 70  $\Omega$ .cm<sup>2</sup>, respectively.

On the other hand, solar cell parameters extracted from the J-V curve of SLG/FTO/ $TiO_2$ /CdS/CZTSSe/Cr-Au were found as short-circuit density ( $J_{sc}$ ) of 0.07

mA.cm<sup>-2</sup>, open circuit voltage ( $V_{oc}$ ) of 160 mV and fill factor (FF) of 24% and efficiency of 0.002%. In addition, series resistance ( $R_s$ ) and shunt resistance ( $R_{sh}$ ) values were found as 90  $\Omega$ .cm<sup>2</sup> and 350  $\Omega$ .cm<sup>2</sup>, respectively.

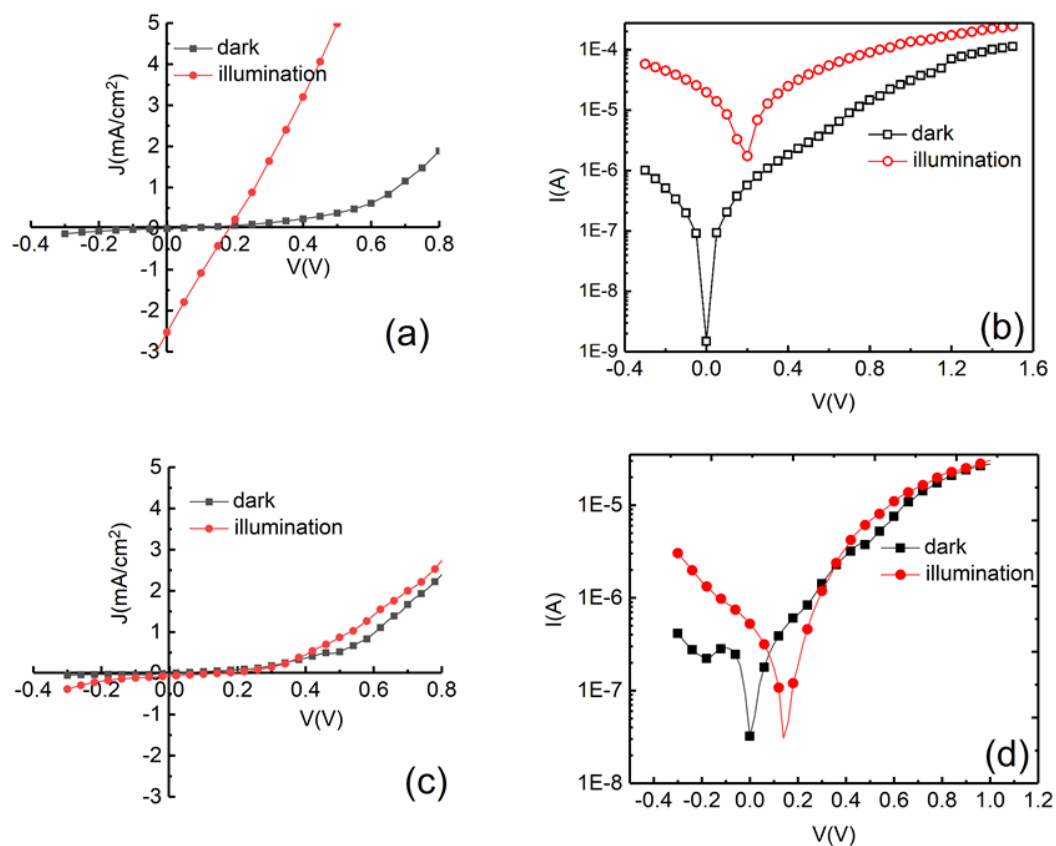


Figure 6.15. J-V and I-V plots in linear and semi-logarithmic scales in dark and under illumination for (a), (b) of SLG/FTO/TiO<sub>2</sub>/CdS/CZTSSe/Au; (c), (d) of SLG/FTO/TiO<sub>2</sub>/CdS/CZTSSe/Cr-Au structures.

The comparison between the solar cell parameters of superstrate structure with different metal contacts was given in Table 6.2. As a result, the maximum power conversion efficiency and minimum series resistance value was obtained in the case of pure Au metal contact.

Table 6.2. Device performance results of SLG/FTO/TiO<sub>2</sub>/CdS/CZTSSe/metal structure with different contact materials

Cell Parameters	<i>Ag-Au alloy</i>	<i>Pure Au</i>	<i>Cr-Au alloy</i>
V <sub>oc</sub> (mV)	280	185	160
J <sub>sc</sub> (mA/cm <sup>2</sup> )	0.27	2.54	0.07
FF (%)	25	24	24
η (%)	0.020	0.120	0.002
R <sub>s</sub> (Ω.cm <sup>2</sup> )	250	25	90
R <sub>sh</sub> (Ω.cm <sup>2</sup> )	970	70	350

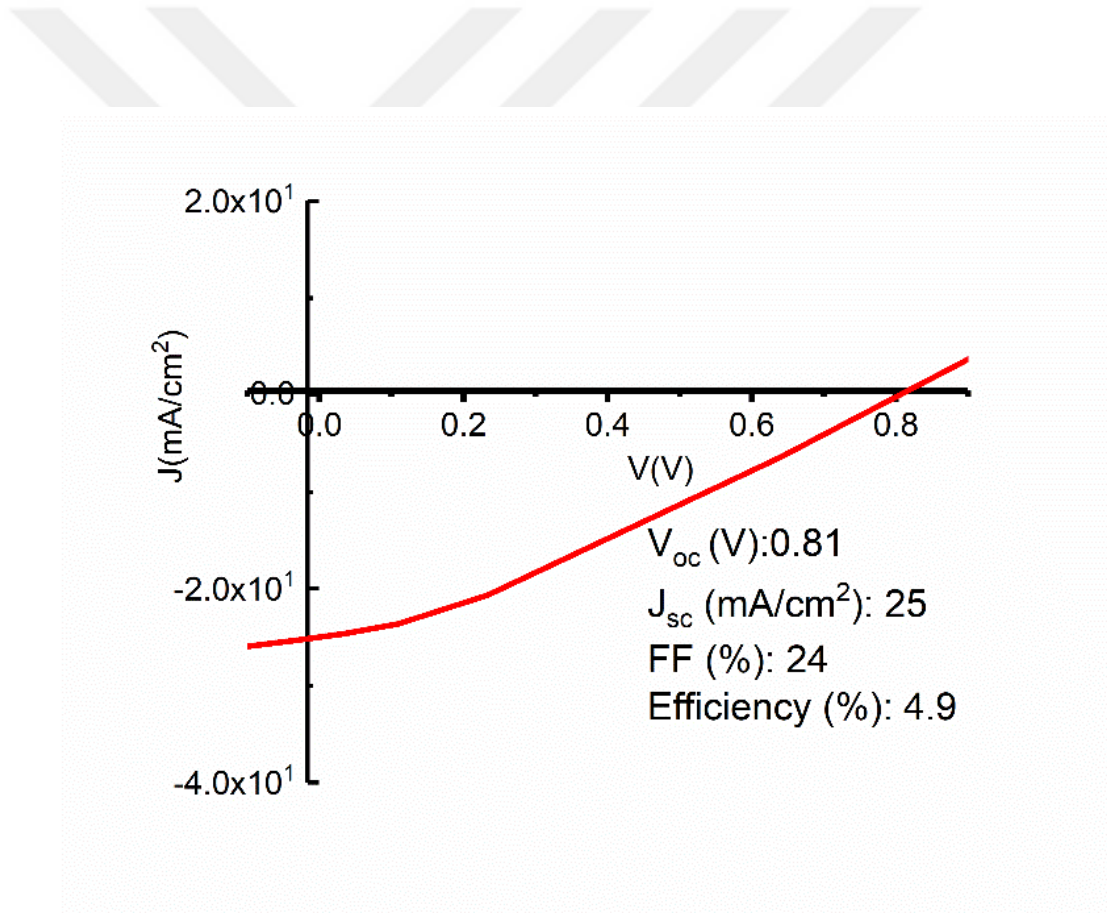


Figure 6.16. Simulated J-V curve of solar cell with high series and low shunt resistance value by using SCAPS 1D.

SCAPS is capable of calculating the effect of series and shunt resistance on the performance of solar cell. In an ideal solar cell, series resistance is assumed to be nearly zero, while shunt resistance is assumed to be infinitely large. However, this is not the case in an experimental study. To exhibit the effect of series and shunt resistance on the performance of solar cell, results of our experiment were used for simulation ( $R_s=25 \Omega cm^2$ ,  $R_{sh}=70 \Omega cm^2$ ). The results of this assumption is given in Figure 6.16. It is deduced that series and shunt resistance of solar cell affects the performance of solar cell negatively.



## CHAPTER 7

### CONCLUSION

“I don’t know anything, but I do know that everything is interesting if you go into it deeply enough”

-Richard P. Feynman

The aim of this study is mainly to produce CZTSSe thin films in an efficient and cost-effective way by excluding any other auxiliary/additional process steps like selenization and sulphurization processes while maintaining the high quality in terms of their the physical properties. Moreover, their characterizations and applications for photovoltaic device are the other objectives of the study.

For this purpose, firstly, CZTSSe crystal was produced by sintering and Bridgman technique. Then, CZTSSe crystal powder was obtained from this crystal since the cost of single-source production is relatively low. CZTSSe thin films were deposited by thermal evaporation using a single evaporation source. Furthermore, structural, optical, and electrical properties of annealed films were analyzed. It was found that samples have Cu poor, Sn-rich composition. And, XRD and Raman scattering measurements indicated the presence of both CZTSSe compound and secondary phases. The band gap of samples was found to be 1.46 eV using transmission and reflection measurements. Films also showed p-type semiconductor behavior.

After the characterization of films, the current transport mechanism and device properties of CZTSSe/n-Si structure were investigated in details. From the dark current-voltage characteristics in wide temperature range, main diode parameters were

calculated by thermionic emission model, and the results revealed the decreasing barrier height and the increasing ideality factor behavior with decreasing temperature, which could be due to the barrier height inhomogeneity at the interface. Thus, the inhomogeneity at the interface was explained by the Gaussian distribution of barrier heights. Under this approximation, mean barrier height ( $\bar{\Phi}_{B0}$ ) and standard deviation ( $\sigma_0$ ) at zero bias were found to be 1.27eV and 0.18V, respectively. By means of modified Richardson plot, Richardson constant was calculated as 120.46 A.cm<sup>-2</sup>K<sup>-2</sup> which was close to theoretical value known for n-Si. In addition, using frequency dependent capacitance-voltage and conductance-voltage characteristics of CZTSSe/n-Si structure, the density of interface state profiles were found by means of high-low frequency capacitance and Hill-Coleman methods, which affects the performance of diode.

Secondly, in this work, a novel single-step growth route by utilizing the RF magnetron sputtering technique was developed for the production of CZTSSe thin films with self-assembled nanoflakes. For this purpose, the six stacked film layers were deposited sequentially by using ZnSe, CuSe, and SnS targets at three different substrate temperatures. During the magnetron sputtering, the well-controlled process parameters such as film thickness and substrate temperature were determined to have strong control over the nanoflake size and dimension. It was also observed that the post-annealing does not affect the size or shape of nanoflakes; it improves the structural properties of films. However, the formation of CZTSSe nanoflakes was critically controlled by the substrate temperature. The nanostructures on the film surface decreased the surface reflection considerably. It was obtained the low surface reflection without any texturing process around 3-4%. The evolution of the CZTSSe nanoflakes was based on the formation of CuSe nanoflake, which had an important role in the formation of nanostructures. As a result, a promising technique was developed for the production of CZTSSe thin films having nanostructured surface without any texturing process.

In the last part of the study, using the CZTSSe absorber layer deposited by RF magnetron sputtering, CZTSSe thin film based solar cells in a superstrate configuration were fabricated. In this context, the structure of glass/ITO/CdS/CZTSSe/metal was investigated using the current-voltage measurements under dark and illumination at an incident light power of  $100\text{mW}/\text{cm}^2$  and quantum efficiency measurements. It was observed that the  $V_{oc}$  was lower than the value of superstrate type kesterite solar cells in the literature and the series resistance was higher than the obtained value in the literature, which is the limiting factor on the device performance. To improve the device performance, titanium dioxide ( $\text{TiO}_2$ ) was coated on top of the FTO layer due to its a hole blocking and wide band gap material. The effect of  $\text{TiO}_2$  thickness on the device performance was studied. The optimum thickness of  $\text{TiO}_2$  was found approximately 90 nm, and the positive effect of  $\text{TiO}_2$  layer on  $V_{oc}$  was obtained considerably. As a result, the FTO/ $\text{TiO}_2$ /CdS/CZTSSe/Au structure showed that the best cell performance, and the main solar cell parameters were found as  $V_{oc}$ : 185mV,  $J_{sc}$ :  $2.54\text{mA}/\text{cm}^2$ .

Further studies are required to improve the solar cell efficiency of FTO/ $\text{TiO}_2$ /CdS/CZTSSe/Au structure. A detailed contact resistivity study is to be done to eliminate (or control) the effect of high series resistance. And, thin  $\text{TiO}_2$  layer could be replaced with another metal oxide like  $\text{NiO}_x$ .



## REFERENCES

- [1] N. H. Stern, *The Economics of Climate Change: The Stern Review* - Nicholas Herbert Stern, Great Britain. Treasury - 2007.
- [2] N. Apergis, J. E. Payne, K. Menyah, and Y. Wolde-Rufael, "On the causal dynamics between emissions, nuclear energy, renewable energy, and economic growth," *Ecol. Econ.*, vol. 69, no. 11, pp. 2255–2260, Sep. 2010.
- [3] N. Apergis and J. E. Payne, "Renewable energy consumption and economic growth: Evidence from a panel of OECD countries," *Energy Policy*, vol. 38, no. 1, pp. 656–660, Jan. 2010.
- [4] M. P. Suryawanshi *et al.*, "CZTS based thin film solar cells: a status review," *Mater. Technol.*, vol. 28, no. 1–2, pp. 98–109, Mar. 2013.
- [5] I. Dincer, "Renewable energy and sustainable development: a crucial review," *Renew. Sustain. Energy Rev.*, vol. 4, no. 2, pp. 157–175, Jun. 2000.
- [6] A. J. McEvoy, L. Castañer, and T. Markvart, *Solar Cells: Materials, Manufacture and Operation*. Academic Press, 2013.
- [7] A. Richter, M. Hermle, and S. W. Glunz, "Reassessment of the limiting efficiency for crystalline silicon solar cells," *IEEE J. Photovoltaics*, vol. 3, no. 4, pp. 1184–1191, 2013.
- [8] M. Yuan, D. B. Mitzi, W. Liu, A. J. Kellock, S. J. Chey, and V. R. Deline, "Optimization of CIGS-Based PV Device through Antimony Doping," *Chem. Mater.*, vol. 22, no. 2, pp. 285–287, Jan. 2010.
- [9] R. W. Birkmire and B. E. McCandless, "CdTe thin film technology: Leading thin film PV into the future," *Curr. Opin. Solid State Mater. Sci.*, vol. 14, no. 6, pp. 139–142, Dec. 2010.
- [10] P. Reinhard *et al.*, "Review of progress toward 20% efficiency flexible CIGS solar cells and manufacturing issues of solar modules," in *2012 IEEE 38th Photovoltaic Specialists Conference (PVSC) PART 2*, 2012, pp. 1–9.
- [11] F. Kessler, D. Herrmann, and M. Powalla, "Approaches to flexible CIGS thin-film solar cells," *Thin Solid Films*, vol. 480–481, pp. 491–498, Jun. 2005.
- [12] F. Kessler and D. Rudmann, "Technological aspects of flexible CIGS solar cells and modules," *Sol. Energy*, vol. 77, no. 6, pp. 685–695, Dec. 2004.
- [13] "Global Solar | Flexible Solar Panels." [Online]. Available: <http://www.globalsolar.com/>. [Accessed: 07-May-2019].
- [14] D. B. Mitzi *et al.*, "A High-Efficiency Solution-Deposited Thin-Film Photovoltaic Device," *Adv. Mater.*, vol. 20, no. 19, pp. 3657–3662, Oct. 2008.

- [15] A. V. Moholkar *et al.*, “Development of CZTS thin films solar cells by pulsed laser deposition: Influence of pulse repetition rate,” *Sol. Energy*, vol. 85, no. 7, pp. 1354–1363, Jul. 2011.
- [16] V. M. Fthenakis, “Life cycle impact analysis of cadmium in CdTe PV production,” *Renew. Sustain. Energy Rev.*, vol. 8, no. 4, pp. 303–334, Aug. 2004.
- [17] Z. Shi, D. Attygalle, and A. H. Jayatissa, “Kesterite-based next generation high performance thin film solar cell: current progress and future prospects,” *J. Mater. Sci. Mater. Electron.*, vol. 28, no. 2, pp. 2290–2306, Jan. 2017.
- [18] S. K. Wallace, D. B. Mitzi, and A. Walsh, “The Steady Rise of Kesterite Solar Cells,” *ACS Energy Lett.*, vol. 2, no. 4, pp. 776–779, Apr. 2017.
- [19] T. Tanaka *et al.*, “Preparation of  $\text{Cu}_2\text{ZnSnS}_4$  thin films by hybrid sputtering,” in *Journal of Physics and Chemistry of Solids*, 2005.
- [20] S. Schorr, H.-J. Hoebler, and M. Tovar, “A neutron diffraction study of the stannite-kesterite solid solution series,” *Eur. J. Mineral.*, 2007.
- [21] H. Katagiri, K. Saitoh, T. Washio, H. Shinohara, T. Kurumadani, and S. Miyajima, “Development of thin film solar cell based on  $\text{Cu}_2\text{ZnSnS}_4$  thin films,” *Sol. Energy Mater. Sol. Cells*, vol. 65, no. 1–4, pp. 141–148, Jan. 2001.
- [22] C. Steinhagen, M. G. Panthani, V. Akhavan, B. Goodfellow, B. Koo, and B. A. Korgel, “Synthesis of  $\text{Cu}_2\text{ZnSnS}_4$  nanocrystals for use in low-cost photovoltaics,” *J. Am. Chem. Soc.*, 2009.
- [23] J. J. Scragg, P. J. Dale, L. M. Peter, G. Zoppi, and I. Forbes, “New routes to sustainable photovoltaics: Evaluation of  $\text{Cu}_2\text{ZnSnS}_4$  as an alternative absorber material,” *Phys. Status Solidi Basic Res.*, 2008.
- [24] “Best Research-Cell Efficiency Chart | Photovoltaic Research | NREL.” [Online]. Available: <https://www.nrel.gov/pv/cell-efficiency.html>. [Accessed: 10-Jun-2019].
- [25] G. B. Haxel, J. B. Hedrick, G. J. Orris, P. H. Stauffer, and J. W. H. II, “Rare earth elements: critical resources for high technology,” 2002.
- [26] K. Oishi *et al.*, “Growth of  $\text{Cu}_2\text{ZnSnS}_4$  thin films on Si (100) substrates by multisource evaporation,” *Thin Solid Films*, vol. 517, no. 4, pp. 1449–1452, 2008.
- [27] B. Shin, O. Gunawan, Y. Zhu, N. A. Bojarczuk, S. J. Chey, and S. Guha, “Thin film solar cell with 8.4% power conversion efficiency using an earth-abundant  $\text{Cu}_2\text{ZnSnS}_4$  absorber,” *Prog. Photovoltaics Res. Appl.*, vol. 21, no. 1, pp. 72–76, Jan. 2013.
- [28] D. H. Son *et al.*, “Growth and Device Characteristics of CZTSSe Thin-Film

- Solar Cells with 8.03% Efficiency,” *Chem. Mater.*, vol. 27, no. 15, pp. 5180–5188, 2015.
- [29] N. Ryota, T. Kunihiko, U. Hisao, J. Kazuo, W. Tsukasa, and K. Hironori, “Cu<sub>2</sub>ZnSnS<sub>4</sub> thin film deposited by sputtering with Cu<sub>2</sub>ZnSnS<sub>4</sub> compound target,” *Jpn. J. Appl. Phys.*, vol. 53, no. 2S, p. 02BC10, 2014.
- [30] N. Song *et al.*, “Epitaxial Cu<sub>2</sub>ZnSnS<sub>4</sub> thin film on Si (111) 4° substrate,” *Appl. Phys. Lett.*, vol. 106, no. 25, p. 252102, 2015.
- [31] Y. B. Kishore Kumar, G. Suresh Babu, P. Uday Bhaskar, and V. Sundara Raja, “Preparation and characterization of spray-deposited Cu<sub>2</sub>ZnSnS<sub>4</sub> thin films,” *Sol. Energy Mater. Sol. Cells*, vol. 93, no. 8, pp. 1230–1237, Aug. 2009.
- [32] N. Kamoun, H. Bouzouita, and B. Rezig, “Fabrication and characterization of Cu<sub>2</sub>ZnSnS<sub>4</sub> thin films deposited by spray pyrolysis technique,” *Thin Solid Films*, vol. 515, no. 15 SPEC. ISS., pp. 5949–5952, 2007.
- [33] F. Yakuphanoglu, “Nanostructure Cu<sub>2</sub>ZnSnS<sub>4</sub> thin film prepared by sol–gel for optoelectronic applications,” *Sol. Energy*, vol. 85, no. 10, pp. 2518–2523, Oct. 2011.
- [34] J. J. Scragg, P. J. Dale, and L. M. Peter, “Towards sustainable materials for solar energy conversion: Preparation and photoelectrochemical characterization of Cu<sub>2</sub>ZnSnS<sub>4</sub>,” *Electrochem. commun.*, vol. 10, no. 4, pp. 639–642, 2008.
- [35] J. Li, T. Ma, M. Wei, W. Liu, G. Jiang, and C. Zhu, “The Cu<sub>2</sub>ZnSnSe<sub>4</sub> thin films solar cells synthesized by electrodeposition route,” *Appl. Surf. Sci.*, vol. 258, no. 17, pp. 6261–6265, Jun. 2012.
- [36] J. Tao *et al.*, “7.1% efficient co-electroplated Cu<sub>2</sub>ZnSnS<sub>4</sub> thin film solar cells with sputtered CdS buffer layers,” *Green Chem.*, vol. 18, no. 2, pp. 550–557, 2016.
- [37] W. Wang *et al.*, “Device characteristics of CZTSSe thin-film solar cells with 12.6% efficiency,” *Adv. Energy Mater.*, vol. 4, no. 7, pp. 1–5, May 2014.
- [38] A. Walsh, S. Chen, S. H. Wei, and X. G. Gong, “Kesterite thin-film solar cells: Advances in materials modelling of Cu<sub>2</sub>ZnSnS<sub>4</sub>,” *Adv. Energy Mater.*, 2012.
- [39] S. Siebentritt and S. Schorr, “Kesterites—a challenging material for solar cells,” *Prog. Photovoltaics Res. Appl.*, vol. 20, no. 5, pp. 512–519, Aug. 2012.
- [40] B. J. Stanbery, “Copper Indium Selenides and Related Materials for Photovoltaic Devices,” *Crit. Rev. Solid State Mater. Sci.*, vol. 27, no. 2, pp. 73–117, Apr. 2002.
- [41] S. Schorr, “The crystal structure of kesterite type compounds: A neutron and X-ray diffraction study,” *Sol. Energy Mater. Sol. Cells*, vol. 95, no. 6, pp. 1482–

1488, Jun. 2011.

- [42] S. Abermann, “Non-vacuum processed next generation thin film photovoltaics: Towards marketable efficiency and production of CZTS based solar cells,” *Sol. Energy*, 2013.
- [43] K. Moriya, J. Watabe, K. Tanaka, and H. Uchiki, “Characterization of  $\text{Cu}_2\text{ZnSnS}_4$  thin films prepared by photo-chemical deposition,” in *Physica Status Solidi (C) Current Topics in Solid State Physics*, 2006.
- [44] K. Sekiguchi, K. Tanaka, K. Moriya, and H. Uchiki, “Epitaxial growth of  $\text{Cu}_2\text{ZnSnS}_4$  thin films by pulsed laser deposition,” in *Physica Status Solidi (C) Current Topics in Solid State Physics*, 2006.
- [45] H. Matsushita, T. Maeda, A. Katsui, and T. Takizawa, “Thermal analysis and synthesis from the melts of Cu-based quaternary compounds Cu–III–IV–VI<sub>4</sub> and  $\text{Cu}_2$ –II–IV–VI<sub>4</sub> (II=Zn,Cd; III=Ga,In; IV=Ge,Sn; VI=Se),” *J. Cryst. Growth*, 2000.
- [46] R. A. Wibowo, W. S. Kim, E. S. Lee, B. Munir, and K. H. Kim, “Single step preparation of quaternary thin films by RF magnetron sputtering from binary chalcogenide targets,” *J. Phys. Chem. Solids*, vol. 68, no. 10, pp. 1908–1913, Oct. 2007.
- [47] R. A. Wibowo, E. S. Lee, B. Munir, and K. H. Kim, “Pulsed laser deposition of quaternary  $\text{Cu}_2\text{ZnSnSe}_4$  thin films,” *Phys. Status Solidi Appl. Mater. Sci.*, 2007.
- [48] X. Song, X. Ji, M. Li, W. Lin, X. Luo, and H. Zhang, “A Review on Development Prospect of CZTS Based Thin Film Solar Cells,” *Int. J. Photoenergy*, vol. 2014, pp. 1–11, May 2014.
- [49] Y. Zhang, Y. Sun, H. Wang, and H. Yan, “A facile non-vacuum-based  $\text{Cu}_2\text{ZnSnSe}_4$  superstrate solar cell with 2.44% device efficiency,” *Phys. status solidi*, vol. 213, no. 5, pp. 1324–1328, May 2016.
- [50] J. He *et al.*, “Single-step preparation and characterization of  $\text{Cu}_2\text{ZnSn}(\text{S}_x\text{Se}_{1-x})_4$  thin films deposited by pulsed laser deposition method,” *J. Alloys Compd.*, vol. 529, pp. 34–37, Jul. 2012.
- [51] C.-L. Wang, C.-C. Wang, B. Reeja-Jayan, and A. Manthiram, “Low-cost, Mo(S,Se)<sub>2</sub>-free superstrate-type solar cells fabricated with tunable band gap  $\text{Cu}_2\text{ZnSn}(\text{S}_{1-x}\text{Se}_x)_4$  nanocrystal-based inks and the effect of sulfurization,” *RSC Adv.*, vol. 3, no. 43, p. 19946, Oct. 2013.
- [52] O. Gunawan, T. K. Todorov, and D. B. Mitzi, “Loss mechanisms in hydrazine-processed  $\text{Cu}_2\text{ZnSn}(\text{Se,S})_4$  solar cells,” *Appl. Phys. Lett.*, vol. 97, no. 23, p. 233506, Dec. 2010.

- [53] M. Berruet, Y. Di Iorio, C. J. Pereyra, R. E. Marotti, and M. Vázquez, “Highly-efficient superstrate  $\text{Cu}_2\text{ZnSnS}_4$  solar cell fabricated low-cost methods,” *Phys. status solidi - Rapid Res. Lett.*, vol. 11, no. 8, p. 1700144, Aug. 2017.
- [54] D. B. Mitzi, O. Gunawan, T. K. Todorov, and D. A. R. Barkhouse, “Prospects and performance limitations for Cu-Zn-Sn-S-Se photovoltaic technology.,” *Philos. Trans. A. Math. Phys. Eng. Sci.*, vol. 371, no. 1996, p. 20110432, Aug. 2013.
- [55] P. Xin, J. K. Larsen, F. Deng, and W. N. Shafarman, “Development of  $\text{Cu}(\text{In,Ga})\text{Se}_2$  superstrate devices with alternative buffer layers,” *Sol. Energy Mater. Sol. Cells*, vol. 157, pp. 85–92, Dec. 2016.
- [56] M. D. Heinemann *et al.*, “Advantageous light management in  $\text{Cu}(\text{In,Ga})\text{Se}_2$  superstrate solar cells,” *Sol. Energy Mater. Sol. Cells*, vol. 150, pp. 76–81, Jun. 2016.
- [57] D. Lee and K. Yong, “Solution-processed  $\text{Cu}_2\text{ZnSnS}_4$  superstrate solar cell using vertically aligned ZnO nanorods,” *Nanotechnology*, vol. 25, no. 6, p. 065401, Feb. 2014.
- [58] M. Kurokawa, K. Tanaka, K. Moriya, and H. Uchiki, “Fabrication of Three-Dimensional-Structure Solar Cell with  $\text{Cu}_2\text{ZnSnS}_4$ ,” *Jpn. J. Appl. Phys.*, vol. 51, no. 10S, p. 10NC33, Oct. 2012.
- [59] Q. Chen, S. Cheng, S. Zhuang, and X. Dou, “ $\text{Cu}_2\text{ZnSnS}_4$  solar cell prepared entirely by non-vacuum processes,” *Thin Solid Films*, vol. 520, no. 19, pp. 6256–6261, Jul. 2012.
- [60] K. Tanaka, M. Kurokawa, K. Moriya, and H. Uchiki, “Surface morphology improvement of three-dimensional solar cell with  $\text{Cu}_2\text{ZnSnS}_4$  absorber,” *J. Alloys Compd.*, vol. 571, pp. 98–102, Sep. 2013.
- [61] C.-L. Wang and A. Manthiram, “Low-Cost CZTSSe Solar Cells Fabricated with Low Band Gap CZTSe Nanocrystals, Environmentally Friendly Binder, and Nonvacuum Processes,” *ACS Sustain. Chem. Eng.*, vol. 2, no. 4, pp. 561–568, Apr. 2014.
- [62] Z. Wang, N. Brodusch, R. Gauvin, and G. P. Demopoulos, “Lithium-doped  $\text{Cu}_2\text{ZnSnS}_4$  superstrate solar cells with 5% efficiency – An alternative to thin film kesterite photovoltaics,” *Nano Energy*, vol. 53, pp. 130–134, Nov. 2018.
- [63] M. A. Green, *Solar cells: operating principles, technology, and system applications*. Prentice-Hall, 1982.
- [64] C. M. Wolfe, N. Holonyak Jr., and G. E. Stillman, *Physical Properties of Semiconductors*. New Jersey: Prentice Hall, Englewood Cliffs, 1989.
- [65] M. Fukuda, *Optical semiconductor devices*. Wiley, 1999.

- [66] D. K. Schroder, *Semiconductor material and device characterization*. IEEE Press, 2006.
- [67] J. I. Pankov, *Optical Processes in Semiconductors*. New Jersey: Prentice-Hall, Inc., Englewood Cliffs, 1971.
- [68] J. Nelson, *The physics of solar cells*. 2003.
- [69] S. Das, “Growth, Fabrication and Characterization of  $\text{Cu}_2\text{ZnSn}(\text{S}_x\text{Se}_{1-x})_4$  Photovoltaic Absorber and Thin-Film Heterojunction Solar,” 2014.
- [70] B. G. Streetman and S. Banerjee, *Solid state electronic devices*. Pearson/Prentice Hall, 2006.
- [71] S. Kasap, *Principles of electronic materials and devices*. McGraw-Hill, 2006.
- [72] C. J. Chen, *Physics of solar energy*. John Wiley & Sons, 2011.
- [73] M. A. Green, “Solar cell fill factors: General graph and empirical expressions,” *Solid. State. Electron.*, vol. 24, no. 8, pp. 788–789, Aug. 1981.
- [74] B. Qi and J. Wang, “Fill factor in organic solar cells,” *Phys. Chem. Chem. Phys.*, vol. 15, no. 23, p. 8972, May 2013.
- [75] M. Burgelman, P. Nollet, and S. Degraeve, “Modelling polycrystalline semiconductor solar cells,” *Thin Solid Films*, 2000.
- [76] M. Burgelman and J. Marlein, “Analysis of graded band gap solar cells with SCAPS,” *23rd Eur. Photovolt. Sol.*, 2008.
- [77] L. Lin, L. Jiang, Y. Qiu, and B. Fan, “Analysis of  $\text{Sb}_2\text{Se}_3/\text{CdS}$  based photovoltaic cell: A numerical simulation approach,” *J. Phys. Chem. Solids*, vol. 122, pp. 19–24, Nov. 2018.
- [78] O. K. Simya, A. Mahaboobbatcha, and K. Balachander, “A comparative study on the performance of Kesterite based thin film solar cells using SCAPS simulation program,” *Superlattices Microstruct.*, vol. 82, pp. 248–261, Jun. 2015.
- [79] T. Azizi, H. Toujeni, M. Ben Karoui, and R. Gharbi, “A comprehensive device modeling of solid state dye sensitized solar cell with SCAPS-1D,” in *2019 19th International Conference on Sciences and Techniques of Automatic Control and Computer Engineering (STA)*, 2019, pp. 336–340.
- [80] P. Kelly and R. Arnell, “Magnetron sputtering: a review of recent developments and applications,” *Vacuum*, vol. 56, no. 3, pp. 159–172, Mar. 2000.
- [81] S. Kayacan İlday, “Multi-scale self-assembly of silicon quantum dots into an anisotropic three-dimensional random network,” Middle East Technical University, 2014.

- [82] B. B. He, *Two-dimensional x-ray diffraction*, Second edition. .
- [83] E. Kaelble, *Handbook of X-rays: for diffraction, emission, absorption, and microscopy*. 1967.
- [84] M. Dimitrievska *et al.*, “Multiwavelength excitation Raman scattering study of polycrystalline kesterite  $\text{Cu}_2\text{ZnSnS}_4$  thin films,” *Appl. Phys. Lett.*, vol. 104, no. 2, p. 021901, Jan. 2014.
- [85] M. Dimitrievska, “Crystalline and vibrational properties of kesterites,” Universitat de Barcelona, 2016.
- [86] A. Fairbrother, “Development of  $\text{Cu}_2\text{ZnSn}(\text{S},\text{Se})_4$  based solar cells,” Universitat de Barcelona, 2014.
- [87] D. K. Schroder, *Semiconductor Material and Device Characterization: Third Edition*. IEEE Press, 2005.
- [88] A. Cantarero, “Raman Scattering Applied to Materials Science,” *Procedia Mater. Sci.*, 2015.
- [89] J. Goldstein, *Scanning electron microscopy and X-ray microanalysis : a text for biologists, materials scientists, and geologists*. 2nd ed: Plenum Press, 1992.
- [90] G. Haugstad, *Atomic force microscopy: understanding basic modes and advanced applications*. John Wiley & Sons, 2012.
- [91] H. Karaağaç, “Electrical, structural and optical properties of  $\text{AgGaSe}_{2-x}\text{S}_x$  thin films grown by sintered powder,” Middle East Technical University, 2010.
- [92] T. Çolakoğlu, “The effects of post-annealing process on the physical properties of silver-indium-selenium ternary semiconductor thin films deposited by electron beam technique,” Middle East Technical University, 2009.
- [93] P. Salomé *et al.*, “Growth and characterization of  $\text{Cu}_2\text{ZnSn}(\text{S},\text{Se})_4$  thin films for solar cells,” *Sol. Energy Mater. Sol. Cells*, vol. 101, pp. 147–153, 2012.
- [94] S. Ranjbar, M. R. Rajesh Menon, P. A. Fernandes, and A. F. Da Cunha, “Effect of selenization conditions on the growth and properties of  $\text{Cu}_2\text{ZnSn}(\text{S},\text{Se})_4$  thin films,” *Thin Solid Films*, vol. 582, pp. 188–192, 2015.
- [95] M. Grossberg, J. Krustok, J. Raudoja, K. Timmo, M. Altosaar, and T. Raadik, “Photoluminescence and Raman study of  $\text{Cu}_2\text{ZnSn}(\text{Se}_x\text{S}_{1-x})_4$  monograins for photovoltaic applications,” *Thin Solid Films*, vol. 519, pp. 7403–7406, 2011.
- [96] A. Fairbrother *et al.*, “Secondary phase formation in Zn-rich  $\text{Cu}_2\text{ZnSnSe}_4$  - based solar cells annealed in low pressure and temperature conditions,” *Prog. Photovoltaics Res. Appl.*, vol. 22, no. 4, pp. 479–487, Apr. 2014.
- [97] K. Muska *et al.*, “Impact of  $\text{Cu}_2\text{ZnSn}(\text{Se}_x\text{S}_{1-x})_4$  ( $x = 0.3$ ) compositional ratios

- on the monograin powder properties and solar cells,” *Thin Solid Films*, vol. 535, no. 1, pp. 35–38, 2013.
- [98] N. M. M. Shinde, D. P. P. Dubal, D. S. S. Dhawale, C. D. D. Lokhande, J. H. H. Kim, and J. H. H. Moon, “Room temperature novel chemical synthesis of  $\text{Cu}_2\text{ZnSnS}_4$  (CZTS) absorbing layer for photovoltaic application,” *Mater. Res. Bull.*, vol. 47, no. 2, pp. 302–307, Feb. 2012.
- [99] G. Suresh Babu, Y. B. Kishore Kumar, P. Uday Bhaskar, and S. Raja Vanjari, “Effect of  $\text{Cu}/(\text{Zn}+\text{Sn})$  ratio on the properties of co-evaporated  $\text{Cu}_2\text{ZnSnSe}_4$  thin films,” *Sol. Energy Mater. Sol. Cells*, vol. 94, no. 2, pp. 221–226, 2010.
- [100] Y. Li, T. Yuan, L. Jiang, F. Liu, Y. Liu, and Y. Lai, “ $\text{Cu}_2\text{ZnSnS}_4$  thin film solar cell fabricated by co-electrodeposited metallic precursor,” *J. Mater. Sci. Mater. Electron.*, vol. 26, pp. 204–210, 2015.
- [101] H. H. Güllü, M. Terlemezoğlu, Ö. Bayraklı, D. E. Yıldız, and M. Parlak, “Investigation of carrier transport mechanisms in the Cu–Zn–Se based heterostructure grown by sputtering technique,” *Can. J. Phys.*, vol. 96, no. 7, pp. 816–825, Jul. 2018.
- [102] K. Yılmaz, M. Parlak, and Ç. Erçelebi, “Investigation of photovoltaic properties of amorphous InSe thin film based Schottky devices,” *Semicond. Sci. Technol.*, vol. 22, no. 12, pp. 1268–1271, Dec. 2007.
- [103] J. Martínez-Pastor, A. Segura, J. L. Valdés, and A. Chevy, “Electrical and photovoltaic properties of indium-tin-oxide/ *p* -InSe/Au solar cells,” *J. Appl. Phys.*, vol. 62, no. 4, pp. 1477–1483, Aug. 1987.
- [104] S. M. Sze and K. K. Ng, *Semiconductor Devices: Physics and Technology*. 2006.
- [105] G. Ersöz, İ. Yücedağ, S. Bayrakdar, Ş. Altındal, and A. Gümüş, “Investigation of photo-induced effect on electrical properties of Au/PPy/n-Si (MPS) type schottky barrier diodes,” *J. Mater. Sci. Mater. Electron.*, vol. 28, no. 9, pp. 6413–6420, May 2017.
- [106] J. M. Andrews and M. P. Lepselter, “Reverse current-voltage characteristics of metal-silicide Schottky diodes,” *Solid State Electron.*, vol. 13, no. 7, pp. 1011–1023, 1970.
- [107] K. Moraki, S. Bengi, S. Zeyrek, M. M. Bülbül, and Ş. Altındal, “Temperature dependence of characteristic parameters of the Au/C20H12/n-Si Schottky barrier diodes (SBDs) in the wide temperature range,” *J. Mater. Sci. Mater. Electron.*, vol. 28, no. 5, pp. 3987–3996, Mar. 2017.
- [108] W. Mönch, “Barrier heights of real Schottky contacts explained by metal-induced gap states and lateral inhomogeneities,” *J. Vac. Sci. Technol. B Microelectron. Nanom. Struct.*, vol. 17, no. 4, p. 1867, 1999.

- [109] R. T. Tung, "Electron transport at metal-semiconductor interfaces: General theory," *Phys. Rev. B*, vol. 45, no. 23, pp. 13509–13523, Jun. 1992.
- [110] R. T. Tung, "Recent advances in Schottky barrier concepts," *Mater. Sci. Eng. R Reports*, vol. 35, no. 1, pp. 1–138, 2001.
- [111] H. Tecimer, Ş. Altındal, S. Aksu, Y. Atasoy, and E. Bacaksız, "Interpretation of barrier height inhomogeneities in Au/In<sub>2</sub>S<sub>3</sub>/SnO<sub>2</sub>/(In-Ga) structures at low temperatures," *J. Mater. Sci. Mater. Electron.*, vol. 28, no. 10, pp. 7501–7508, May 2017.
- [112] S. Chand and J. Kumar, "Current-voltage characteristics and barrier parameters of Pd<sub>2</sub>Si/p-Si(111) Schottky diodes in a wide temperature range," *Semicond. Sci. Technol.*, vol. 10, no. 12, pp. 1680–1688, Dec. 1995.
- [113] R. F. Schmitsdorf, T. U. Kampen, and Mönch W., "Explanation of the linear correlation between barrier heights and ideality factors of real metal-semiconductor contacts by laterally nonuniform Schottky barriers," *J. Vac. Sci. Technol. B Microelectron. Nanom. Struct.*, vol. 15, no. 4, p. 1221, Jul. 1997.
- [114] R. T. Tung, "Electron transport of inhomogeneous Schottky barriers," *Appl. Phys. Lett.*, vol. 58, no. 24, pp. 2821–2823, Jun. 1991.
- [115] S. Acar, S. Karadeniz, N. Tuğluoğlu, A. B. Selçuk, and M. Kasap, "Gaussian distribution of inhomogeneous barrier height in Ag/p-Si (1 0 0) Schottky barrier diodes," *Appl. Surf. Sci.*, vol. 233, no. 1–4, pp. 373–381, Jun. 2004.
- [116] A. Kocyigit, · I Orak, · Ş Aydoğan, · Z Çaldıran, and · A Turut, "Temperature-dependent C-V characteristics of Au/ZnO/n-Si device obtained by atomic layer deposition technique," *J. Mater. Sci. Mater. Electron.*, vol. 28, pp. 5880–5886, 1234.
- [117] S. Naik Shankar and V. Reddy Rajagopal, "Analysis of current–voltage–temperature (I–V–T) and capacitance–voltage–temperature (C–V–T) characteristics of Ni/Au Schottky contacts on n-type InP," *Superlattices Microstruct.*, vol. 48, no. 3, pp. 330–342, Sep. 2010.
- [118] A. Tataroğlu and Ş. Altındal, "Analysis of electrical characteristics of Au/SiO<sub>2</sub>/n-Si (MOS) capacitors using the high-low frequency capacitance and conductance methods," *Microelectron. Eng.*, vol. 85, no. 11, pp. 2256–2260, 2008.
- [119] W. A. Hill and C. . Coleman, "A single-frequency approximation for interface-state density determination," *Solid. State. Electron.*, vol. 23, no. 9, pp. 987–993, Sep. 1980.
- [120] F. Yakuphanoglu, "Nanostructure Cu<sub>2</sub>ZnSnS<sub>4</sub> thin film prepared by sol-gel for optoelectronic applications," *Sol. Energy*, vol. 85, no. 10, pp. 2518–2523, 2011.

- [121] S. S. Mali *et al.*, “Novel synthesis of kesterite  $\text{Cu}_2\text{ZnSnS}_4$  nanoflakes by successive ionic layer adsorption and reaction technique: Characterization and application,” *Electrochim. Acta*, 2012.
- [122] M. Patel, H.-S. Kim, and J. Kim, “Wafer-scale production of vertical SnS multilayers for high-performing photoelectric devices,” *Nanoscale*, vol. 9, no. 41, pp. 15804–15812, Oct. 2017.
- [123] P. K. Sarswat, N. Deka, S. Jagan Mohan Rao, M. L. Free, and G. Kumar, “Surface Texture-Induced Enhancement of Optical and Photoelectrochemical Activity of  $\text{Cu}_2\text{ZnSnS}_4$  Photocathodes,” *J. Electron. Mater.*, vol. 46, no. 8, pp. 5308–5318, Aug. 2017.
- [124] A. Nagaoka, K. Yoshino, H. Taniguchi, T. Taniyama, K. Kakimoto, and H. Miyake, “Growth and characterization of  $\text{Cu}_2\text{ZnSn}(\text{S}_x\text{Se}_{1-x})_4$  alloys grown by the melting method,” *J. Cryst. Growth*, vol. 386, pp. 204–207, Jan. 2014.
- [125] R. Mohammadigharehbagh, S. Özen, H. H. Yudar, S. Pat, and Ş. Korkmaz, “The electrical, elemental, optical, and surface properties of Si-doped ZnO thin films prepared by thermionic vacuum arc,” *Mater. Res. Express*, vol. 4, no. 9, p. 096404, Sep. 2017.
- [126] S. Das and K. C. Mandal, “Growth and characterization of kesterite  $\text{Cu}_2\text{ZnSn}(\text{S}_x\text{Se}_{1-x})_4$  crystals for photovoltaic applications,” vol. 57, pp. 135–139, 2014.
- [127] Ö. Bayraklı, M. Terlemezoglu, H. H. Güllü, and M. Parlak, “Investigation of precursor sequence and post-annealing effects on the properties of  $\text{Cu}_2\text{SnZnSe}_4$  thin films deposited by the elemental thermal evaporation,” *Mater. Res. Express*, vol. 4, no. 8, p. 086411, Aug. 2017.
- [128] T. P. Dhakal, C. Y. Peng, R. Reid Tobias, R. Dasharathy, and C. R. Westgate, “Characterization of a CZTS thin film solar cell grown by sputtering method,” *Sol. Energy*, vol. 100, pp. 23–30, Feb. 2014.
- [129] M. Grossberg, J. Krustok, J. Raudoja, K. Timmo, M. Altosaar, and T. Raadik, “Photoluminescence and Raman study of  $\text{Cu}_2\text{ZnSn}(\text{Se}_x\text{S}_{1-x})_4$  monograins for photovoltaic applications,” *Thin Solid Films*, vol. 519, no. 21, pp. 7403–7406, Aug. 2011.
- [130] O. Ramdani *et al.*, “One-step electrodeposited  $\text{CuInSe}_2$  thin films studied by Raman spectroscopy,” *Thin Solid Films*, vol. 515, no. 15, pp. 5909–5912, May 2007.
- [131] M. Li, M. Zheng, T. Zhou, C. Li, L. Ma, and W. Shen, “Fabrication and characterization of ordered  $\text{CuIn}_{(1-x)}\text{Ga}_x\text{Se}_2$  nanopore films via template-based electrodeposition,” *Nanoscale Res. Lett.*, vol. 7, no. 1, p. 675, Dec. 2012.
- [132] M. Terlemezoglu, Ö. Bayraklı, H. H. Güllü, T. Çolakoğlu, D. E. Yildiz, and M. Parlak, “Analysis of current conduction mechanism in CZTSSe/n-Si structure,”

- J. Mater. Sci. Mater. Electron.*, vol. 29, no. 7, pp. 5264–5274, Apr. 2018.
- [133] J. Y. W. Seto, “The electrical properties of polycrystalline silicon films,” *J. Appl. Phys.*, vol. 46, no. 12, pp. 5247–5254, Dec. 1975.
- [134] N. Mott and E. Davis, *Electronic processes in non-crystalline materials*, 2nd ed. Clarendon Press, 2012.
- [135] R. H. Bube, *Photoelectronic properties of semiconductors*. Cambridge University Press, 1992.
- [136] M. Zhong, S. Liu, H. Li, and C. Li, “Superstrate-type  $\text{Cu}_2\text{ZnSnS}_4$  solar cells without sulfurization fabricated by spray pyrolysis,” *Chalcogenide Lett.*, 2018.





## CURRICULUM VITAE

### PERSONAL INFORMATION

Surname, Name : Terlemezođlu, Makbule  
Nationality : Turkish (TC)  
Date and Place of Birth : 19 July 1985, ŐiŐli  
Phone : +90 312 210 50 80  
E-mail : tmakbule@metu.edu.tr

### EDUCATION

Degree	Institution	Year of Graduation
MS	METU Physics	2013
BS	ESOGÜ Mathematics (Double Major)	2009
BS	EskiŐehir Osmangazi Univesity (ESOGÜ) Physics	2008 (with first rank)

### WORK EXPERIENCE

Year	Place	Enrollment
2010-Present	METU	Research Assistant
2009-2010	Tekirdađ Namık Kemal University	Research Assistant

### FOREIGN LANGUAGES

Advanced English

### PUBLICATIONS

#### A. Articles

1. E. Peksu, **M. Terlemezolu**, M. Parlak, and H. Karaagac, "Characterization of one-step deposited  $\text{Cu}_2\text{ZnSnS}_4$  thin films derived from a single crystalline powder," *Renew. Energy*, vol. 143, pp. 1133–1142, Dec. 2019.

2. Ö. B. Sürücü, H. H. Güllü, **M. Terlemezoğlu**, D.E. Yildiz and M. Parlak, “Determination of current transport characteristics in Au-Cu/CuO/n-Si Schottky diodes,” *Phys. B Condens. Matter*, vol. 570, pp. 246–253, Oct. 2019.
3. H.H. Gullu, Ö. Bayraklı Sürücü, **M. Terlemezoğlu**, D. E. Yildiz, and M. Parlak, “Investigation of electrical characteristics of Ag/ZnO/Si sandwich structure,” *J. Mater. Sci. Mater. Electron.*, vol. 30, no. 16, pp. 15371–15378, Aug.2019.
4. H. H. Gullu, D. E. Yildiz, Ö. Bayrakli Sürücü, **M. Terlemezoğlu**, and M. Parlak, “Temperature dependence of electrical properties in In/Cu<sub>2</sub>ZnSnTe<sub>4</sub>/Si/Ag diodes,” *Bull. Mater. Sci.*, vol. 42, no. 2, p. 45, Apr. 2019.
5. S. Delice, M. Isik, H. H. Gullu, **M. Terlemezoğlu**, O. Bayrakli Surucu, M. Parlak, and N. M. Gasanly., “Temperature dependence of band gaps in sputtered SnSe thin films,” *J. Phys. Chem. Solids*, vol. 131, pp. 22–26, Aug. 2019.
6. **M. Terlemezoğlu**, Ö. Bayraklı Sürücü, C. Dogru, H. H. Güllü, E. H. Ciftpinar, Ç. Erçelebi, and M. Parlak., “CZTSSe thin films fabricated by single step deposition for superstrate solar cell applications,” *J. Mater. Sci. Mater. Electron.*, pp. 1–6, May 2019.
7. H. H. Gullu, Ö. Bayraklı Sürücü, **M. Terlemezoğlu**, D. E. Yildiz, and M. Parlak, “Frequency effect on electrical and dielectric characteristics of In/Cu<sub>2</sub>ZnSnTe<sub>4</sub>/Si/Ag diode structure,” *J. Mater. Sci. Mater. Electron.*, vol. 30, no. 10, pp. 9814–9821, May 2019.
8. **M. Terlemezoğlu**, Ö. Bayraklı Sürücü, T. Çolakoğlu, M. K. Abak, H. H. Güllü, Ç. Erçelebi, and M. Parlak, “Construction of self-assembled vertical nanoflakes on CZTSSe thin films,” *Mater. Res. Express*, vol. 6, no. 2, p. 026421, Nov. 2018.
9. **M. Terlemezoğlu**, Ö. Bayraklı, H. H. Güllü, T. Çolakoğlu, D. E. Yildiz, and M. Parlak, “Analysis of current conduction mechanism in CZTSSe/n-Si structure,” *J. Mater. Sci. Mater. Electron.*, vol. 29, no. 7, pp. 5264–5274, Apr. 2018.
10. H. H. Güllü, **M. Terlemezoğlu**, Ö. Bayraklı, D. E. Yıldız, and M. Parlak, “Investigation of carrier transport mechanisms in the Cu–Zn–Se based hetero-structure grown by sputtering technique,” *Can. J. Phys.*, vol. 96, no. 7, pp. 816–825, Jul. 2018.
11. Ö. Bayraklı, **M. Terlemezoğlu**, H. H. Güllü, and M. Parlak, “Investigation of precursor sequence and post-annealing effects on the properties of Cu<sub>2</sub>SnZnSe<sub>4</sub> thin films deposited by the elemental thermal evaporation,” *Mater. Res. Express*, vol. 4, no. 8, p. 086411, Aug. 2017.

12. Ö. Bayraklı, **M. Terlemezoglu**, H. H. Güllü, and M. Parlak, “Deposition of CZTSe thin films and illumination effects on the device properties of Ag/n-Si/p-CZTSe/In heterostructure,” *J. Alloys Compd.*, vol. 709, pp. 337–343, Jun. 2017.

#### A. International Conference Papers

1. H. Karaagac, O. Guller, E. Peksu, E. Humali, **M. Terlemezoglu**, M. Parlak, and M. S. Islam., “Transfer of ordered and disordered Si nanowires onto alien substrates for the fabrication of third-generation solar cells,” in *Micro- and Nanotechnology Sensors, Systems, and Applications XI*, 2019, vol. 10982, p. 4.

#### B. Oral Presentations

1. **M. Terlemezoglu**, Ö. Bayraklı, T. Çolakoğlu, H. H. Güllü, M. K. Abak, , Ç. Erçelebi, and M. Parlak, “Directional Self Assembly of Nanoflakes on the Surface of CZTSSe Thin Films on Glass Substrates: Growth and Characterization” ,The 33<sup>rd</sup> Şişecam Glass Symposium,2018.
2. **M. Terlemezoglu**, Ö. Bayraklı, C. Dogru, H. H. Güllü, E. H. Ciftpinar, Ç. Erçelebi, and M. Parlak “Fabrication of CZTSSe Superstrate Solar Cells by RF Magnetron Sputtering Technique”, Turkish Physical Society 34th International Physics Congress (TFD-34),2018.
3. Ö. Bayraklı, H. H. Güllü , **M. Terlemezoglu**, D. E. Yıldız and M. Parlak “Fabrication and Electrical Characterization of p-AgGa0.5In0.5Te2 Thin Film Heterostructure with Cd-Free Front Layer”, Turkish Physical Society 34th International Physics Congress (TFD-34), 2018.
4. H. H. Güllü , **M. Terlemezoglu**, Ö. Bayraklı, D. E. Yıldız and M. Parlak “Investigation of carrier transport mechanisms in the CuZnSe2-based heterostructure grown by sputtering technique”, Turkish Physical Society 33th International Physics Congress (TFD-33), 2017.
5. G. Sürücü, Ö. Bayraklı, H. H. Güllü , **M. Terlemezoglu** and M. Parlak “Device Behavior of CZTSe/Si Nanowire Heterojunction”, Photovoltaic Technical Conference, 2017.
6. Ö. Bayraklı, **M. Terlemezoglu**, H. H. Güllü, D. E. Yıldız, G. Sürücü, and M. Parlak “Deposition of CZTSe thin films and investigation of their devices properties”, International Conference on Condensed Matter and Materials Science, 2017.

7. Ö. Bayraklı, H. H. Güllü, **M. Terlemezoglu** and M. Parlak “Optimization of the Fabrication Process for Al-doped ZnO Thin Films on Soda Lime Glass Substrates by Thermal Heating”, 2017 ICG Annual Meeting and 32<sup>nd</sup> Şişecam Glass Symposium, 2017.

#### **D. Poster Presentations**

1. E. Dönerçark, T. Çolakoğlu, **M. Terlemezoglu**, M. K. Abak, A. Bek and R.Turan “Wet chemical surface finishing for lithography free inverted pyramids”, 35<sup>nd</sup> European Photovoltaic Solar Energy Conference and Exhibition-EU PVSEC, 2018.
2. E. Dönerçark, T. Çolakoğlu, M. K. Abak, **M. Terlemezoglu**, A. Bek and R.Turan “Enhanced optical properties of lithography free inverted pyramids with tetragonal star shape surface morphology”, 8<sup>th</sup> International Conference on Crystalline Silicon Photovoltaics (Silicon PV), 2018.
3. **M. Terlemezoglu**, Ö. Bayraklı, T. Çolakoğlu, M. K. Abak, H. H. Güllü, R.Turan and M. Parlak “Self-assembled vertical nanoflakes on the surface of CZTSSe thin films for solar energy harvesting”, European Materials Research Society-Spring Meeting, 2018.
4. C. Dogru, **M. Terlemezoglu**, Ö. Bayraklı, H. H. Güllü and M. Parlak “The Effect of Substrate Temperature on CdZnTe thin films”, European Materials Research Society-Spring Meeting, 2018.
5. M. Demir, **M. Terlemezoglu**, Ö. Bayraklı, H. H. Güllü and M. Parlak “Post-annealing effects of CdSe Thin Films”, European Materials Research Society-Spring Meeting, 2018.
6. Ö. Bayraklı, **M. Terlemezoglu**, H. H. Güllü, G. Sürücü and M. Parlak “Effects of in-situ selenization on the physical properties of CZTSe thin films”, European Materials Research Society-Spring Meeting 2018, 2018.
7. H. H. Güllü, Ö. Bayraklı, **M. Terlemezoglu** and M. Parlak “Material Characterization of Amorphous Molybdenum Oxide Thin Films”, European Materials Research Society-Spring Meeting, 2018.
8. Ö. Bayraklı, **M. Terlemezoglu**, H. H. Güllü, D. E. Yıldız, T. Çolakoğlu, E. Coşkun and M. Parlak “Determination of the Interface Properties of p-CZTSe/n-Si Nanowire Heterojunction Diode”, Materials Research Society (MRS) 2017 Fall Meeting, 2017.
9. H. H. Güllü, D. E. Yıldız, **M. Terlemezoglu** and M. Parlak “Temperature dependent current-voltage characteristics of SnTe-based Schottky Barrier

- Diode”, International Conference on Condensed Matter and Materials Science, 2017.
10. H. H. Güllü, Ö. Bayraklı, **M. Terlemezoğlu** and M. Parlak “Synthesis and Characterization of MoO<sub>3</sub> Thin Films under the Effect of Sputtering Power”, European Materials Research Society (EMRS) Fall Meeting, 2017.
  11. E. Coşkun, H. H. Güllü, Ö. Bayraklı, **M. Terlemezoğlu** and M. Parlak “Synthesis and Structural Characterization on the (Cu,Ag)GaTe<sub>2</sub> Thin Films Deposited on Si Nanowires”, European Materials Research Society-Spring Meeting, 2017.
  12. C. Dogru, Ö. Bayraklı, **M. Terlemezoğlu** and M. Parlak “The Effect of CdCl<sub>2</sub> Treatment on CdZnTe Thin Films”, European Materials Research Society-Spring Meeting, 2017.
  13. **M. Terlemezoğlu**, Ö. Bayraklı, H. H. Güllü, T. Çolakoğlu, and M. Parlak, “Physical properties and device application of CZTSSe thin films deposited by thermal evaporation method” , European Materials Research Society-Spring Meeting, 2017.
  14. Ö. Bayraklı, H. H. Güllü, G. Sürücü, **M. Terlemezoğlu** and M. Parlak “Theoretical and Experimental Investigation of Nano-mechanical Characteristics of SnTe Thin Films.”, European Materials Research Society-Spring Meeting, 2017.
  15. H. H. Güllü, Ö. Bayraklı, C. Emir, **M. Terlemezoğlu** and M. Parlak “Influence of Chemical Post-deposition Treatment on the Structural Properties of ZnSnTe<sub>2</sub> Thin Films”, European Materials Research Society (EMRS) Fall Meeting, 2017.
  16. H. H. Güllü, **M. Terlemezoğlu**, Ö. Bayraklı and M. Parlak “The Effects of Substrate and Annealing Temperatures on Surface Morphology of Sputtered SnSe Thin Films”, European Materials Research Society (EMRS) Fall Meeting, 2017.
  17. Ö. Bayraklı, **M. Terlemezoğlu** , H. H. Güllü, G. Sürücü and M. Parlak “Deposition and characterization of ZTSeS thin films for photovoltaic applications”, Photovoltaic Technical Conference, 2017.
  18. Ö. Bayraklı, H. H. Güllü, **M. Terlemezoğlu** and M. Parlak “Characterization of CZTSe Thin Films for Solar Cell”, 32nd European Photovoltaic Solar Energy Conference and Exhibition-EU PVSEC, 2016.
  19. **M. Terlemezoğlu** , H. H. Güllü, Ö. Bayraklı and M. Parlak “Effect of Zn Doping on CdS Thin Film Deposited by RF Magnetron Sputtering”, 32nd European Photovoltaic Solar Energy Conference and Exhibition-EU PVSEC, 2016.

## PROJECTS

1. TÜBİTAK-1003-Proje no: 315M401 ‘‘Düşük Maliyetli ve Yüksek Verimlilikli Transfer Edilebilir  $\text{Cu}_2\text{ZnSnS}_4$  Tabanlı 3. Nesil Güneş Hücrelerinin Üretimi’’ (2017-2019)- Bursiyer
2. METU-BAP-01-05-2017-002 ‘‘ $\text{Cu}_2\text{ZnSn}(\text{S},\text{Se})_4$  İnce Filmlerinin Fiziksel Buharlaştırma Tekniği ile Üretilmesi ve Özelliklerinin Belirlenmesi’’ (2017)- Araştırmacı
3. METU-BAP-01-05-2016-004 ‘‘ $\text{Cu}_2\text{ZnSnSe}_4$  İnce Filmlerinin Fiziksel Buharlaştırma Tekniği ile Üretilmesi ve Özelliklerinin Belirlenmesi’’ (2016)- Araştırmacı

## ATTENDED INTERNATIONAL CONFERENCES & SUMMER SCHOOLS

1. European Materials Research Society-Spring Meeting, Strasbourg, France, 2018 (18-22 June).
2. Turkish Physical Society 33th International Physics Congress (TFD-33), Muğla, Turkey, 2017 (6-10 September).
3. European Materials Research Society-Spring Meeting, Strasbourg, France, 2017 (22-26 May).
4. 32<sup>nd</sup> European Photovoltaic Solar Energy Conference and Exhibition-EU PVSEC, Munich, Germany, 2016 (20-24 June).
5. 56<sup>th</sup> Course of the International School of Solid State Physics "Materials for Renewable Energy", Erice, Italy, 2012 (18-28 July).

## HOBBIES

Tennis, Swimming